

GEOPHYSICAL INVESTIGATIONS OF THE SEATTLE FAULT ZONE
IN WESTERN WASHINGTON AND A GEOTHERMAL SYSTEM AT
MOUNT PRINCETON, COLORADO

by

Andrew Patrick Lamb

A dissertation
submitted in partial fulfillment
of the requirements for the degree of
Doctor of Philosophy in Geophysics
Boise State University

December 2013

© 2013

Andrew Patrick Lamb

ALL RIGHTS RESERVED

BOISE STATE UNIVERSITY GRADUATE COLLEGE

DEFENSE COMMITTEE AND FINAL READING APPROVALS

of the dissertation submitted by

Andrew Patrick Lamb

Dissertation Title: Geophysical Investigations of the Seattle Fault Zone in Western Washington and a Geothermal System at Mount Princeton, Colorado

Date of Final Oral Examination: 11 July 2013

The following individuals read and discussed the dissertation submitted by student Andrew Patrick Lamb, and they evaluated his presentation and response to questions during the final oral examination. They found that the student passed the final oral examination.

Kasper van Wijk, Ph.D.

Chair, Supervisory Committee

Lee M. Liberty, M.S.

Member, Supervisory Committee

Mila Adam, Ph.D.

Member, Supervisory Committee

David Wilkins, Ph.D.

Member, Supervisory Committee

The final reading approval of the dissertation was granted by Kasper van Wijk, Ph.D., Chair of the Supervisory Committee. The dissertation was approved for the Graduate College by John R. Pelton, Ph.D., Dean of the Graduate College.

To Julie, Eva, and Ella

ACKNOWLEDGMENT

I would like to thank Dr. Kasper van Wijk for his support over the past number of years. His enthusiasm and policy of openness have been invaluable lessons on how to both conduct and promote this field of science. I am truly grateful to have been selected as one of his students and his support has been unwavering throughout. I would also like to thank Boise State as a whole for their incredible support and in particular the past two years. The University went well beyond their remit, and for that I will always be indebted to the school and cannot have wished for a better place to undertake my studies.

I would like to thank Dr. Dylan Mikesell, Dr. Thomas Blum, and Dr. Emily Hinz, who never refrained from helping me out in any way they could. With not being a geophysicist when I entered the program, they had to endure a number of very tedious questions and were always very patient in answering them. I would also like to thank Dr. Mila Adam and Lee Liberty who provided a tremendous amount of support throughout my studies. In particular, I would like to thank them for their help during the past year when things were more difficult than expected.

Last but not least, I would like to thank my family and friends, particularly my late wife Julie who I wish could be here to share in it's completion, my parents David and Pat, my brother Donald, my parents-in-law Sue and Jerry, my cousin Carrie, her husband Mike, and my daughters Eva and Ella who one day will understand why Dad was still in school while they were starting school. I am very grateful to have had the opportunity to

pursue these studies and without everyone's support it would not have been possible. I would now like to use the following two sections to acknowledge all those people and organizations that assisted with the research presented in the two main sections of this dissertation.

Western Limits of the Seattle Fault Zone

I would like to thank the co-authors of my Seattle research paper that was published by the Geological Society of America in their *Geosphere* journal in 2012. These include Lee Liberty, Dr. Richard Blakely, Dr. Tom Pratt, Dr. Brian Sherrod, and Dr. Kasper van Wijk. I would also like to thank Dr. Megan Anderson of Colorado College for providing the gravity data, and Dr. CJ Northrup of Boise State University for his insights into the structure of the region. I thank Pat Karel, Mike Mitchell, Sam Nillson, Larry Otheim, Andrew Nies, and Nick Suttin for their assistance with field work and processing of the BB, CO, FM, SR, and HI lines. I thank Dr. William Stephenson, Dr. Rowland Tabor, Dr. Ralph Haugerud, Dr. Ray Wells, and Dr. Jonathan Glen of the U.S. Geological Survey for their advice, reviews, and comments. I thank Dr. Ken Clark from the University of Puget Sound for sharing information with us about the geology near Bremerton. Finally, I would like to thank Michael Polenzand Trevor Contreras of the Washington Division of Geology and Earth Resources for their advice, which included sharing draft versions of their geologic map for the Holly 7.5-minute quadrangle.

Mt. Princeton, Colorado

I would like to thank the co- authors of my Colorado Leading Edge article that was published by the Society of Exploration Geophysicists in 2012. These include Lee Liberty, Dr. Kasper van Wijk, Dr. André Revil, Chuck Diggins, and Dr. Mike Batzle. Funding for my work in Colorado was provided by the Department of Energy award G018195 and the National Science Foundation award EAR-1142154. Additional funding for the vibroseis was provided by the NSF. I would like to thank the local community and land owners for giving us access to their properties and particularly Bill Moore and Stephen Long. I also thank on everyone's behalf, Chaffee County, the SEG Foundation, ION Geophysical, field camp students, and other local stakeholders for their support. The seismic, DC electrical resistivity, and self-potential data were acquired from 2008 to 2010 as part of the spring geophysical field camp attended by students from the Colorado School of Mines, Boise State University, and Imperial College London. Other individuals who contributed to this work include Dr. Dylan Mikesell, Dr. Thomas Blum, Justin Ball, Dr. Seth Haines, Dr. Andrée Revil, Kyle Richards, Dr. Abderrahim Jardani, Fred Henderson, Dr. William Stephenson, and Dr. John Bradford.

ABSTRACT

We use an array of existing and modified geophysical techniques to investigate the active Seattle thrust fault zone in western Washington and a geothermal system at Mt. Princeton Colorado. Through the integration of different geophysical methods, we can extend our observations of the surface geology to beneath the subsurface, thereby giving us a greater understanding of the structures and their kinematic interplay.

We find geophysical evidence through the use of potential field and seismic data for the Seattle fault zone extending further to the west than previously thought. We also find evidence that the Seattle fault zone may be linked to active fault systems further to the south and west. These findings suggest a larger magnitude earthquake can be sustained on the Seattle fault zone and this has implications for earthquake hazard assessment in the region, as these systems pass under the densely populated urban developments of both Seattle and Tacoma.

The second part of this work is based at the Mount Princeton Hot Springs located in the Upper Arkansas basin in central Colorado. These springs are the result of a lateral offset in the basins major range-front normal fault, termed the Sawatch fault. Imaging and characterizing the near surface of this lateral offset through the use and development of near surface geophysical methods improves our understanding of this geothermal resource. Faults in these geothermal systems can form rapid transport pathways for deep-heated geothermal fluids to migrate upwards into the near surface. We chose two separate field sites that exhibited high geothermal activity hypothesized to be a result of the lateral offset across the Sawatch fault. Both sites are on the order of 0.1 km².

At the first site, we used a 3D refraction survey in conjunction with self-potential and resistivity surveys to determine the near surface structure and underground hot water pathways of the Mt. Princeton geothermal system. We find a number of northwest to southeast striking faults that at our site that suggest the Mt. Princeton hot water springs are being fed from a system to the northwest. These structures are likely connected to the main Sawatch normal fault that bounds the western margin of the Upper Arkansas valley.

At our second site, we acquired a 440 m long multi-component, high resolution seismic survey. The purpose of this survey was to both explore a modification of a surface wave analysis technique, called the Spatial Autocorrelation Method (SPAC) and map the near surface structure. The seismic survey was selected to be coincident with a 160 m deep well that showed a hot water source at a depth of 150 m. We conducted a vertical seismic profile on this well to help constrain our surface seismic survey. We found that adding extra components to the SPAC method improves both signal-to-noise and our spatial resolution of the 2D subsurface velocity profile.

TABLE OF CONTENTS

| | |
|--|------|
| ACKNOWLEDGMENT | v |
| ABSTRACT | viii |
| LIST OF TABLES | xiii |
| LIST OF FIGURES | xiv |
| 1 INTRODUCTION | 1 |
| 1.1 Introduction to the Western Extents of the Seattle Fault in Washington State | 1 |
| 1.2 Introduction to the Mount Princeton Geothermal System in Central Colorado | 2 |
| 2 WESTERN LIMITS OF THE SEATTLE FAULT ZONE AND ITS INTER- ACTION WITH THE OLYMPIC PENINSULA, WASHINGTON | 5 |
| 2.1 Summary | 5 |
| 2.2 Introduction | 6 |
| 2.3 Geological and Geophysical Setting | 11 |
| 2.4 Western Extent of Seattle Fault Zone | 14 |
| 2.4.1 Geophysical Investigations | 15 |
| 2.4.2 Results and interpretations | 21 |
| 2.5 Western extent of Tacoma Fault | 28 |
| 2.5.1 Geophysical investigations | 31 |

| | | |
|-------|---|----|
| 2.6 | Discussion | 33 |
| 2.7 | Conclusions | 39 |
| 3 | THE FIELD OF PAIN STUDY SITE | 41 |
| 3.1 | Introduction | 41 |
| 3.1.1 | Study Site Background | 41 |
| 3.2 | Data Acquisition and Processing | 44 |
| 3.3 | Results and Discussion | 46 |
| 3.4 | Conclusions | 54 |
| 4 | DEADHORSE LAKE, MOUNT PRINCETON: NEAR SURFACE CHARAC- TERIZATION WITH MULTI-COMPONENT SURFACE WAVE CORRELA- TIONS | 56 |
| 4.1 | Glossary of Mathematical Terms Used | 57 |
| 4.2 | Introduction | 58 |
| 4.3 | The SPAC and MuSPAC Methods as Applied to a Homogeneous Half- Space | 60 |
| 4.4 | MuSPAC and Partial-Band Data in a Homogeneous Half-Space | 65 |
| 4.4.1 | Introduction and Experimental Setup | 65 |
| 4.4.2 | Results | 65 |
| 4.4.3 | Discussion | 68 |
| 4.5 | MuSPAC and Body Wave Contamination in a Slab Model | 71 |
| 4.5.1 | Introduction and Experimental Setup | 71 |
| 4.5.2 | Results | 73 |
| 4.5.3 | Discussion | 78 |

| | | |
|-------|--|-----|
| 4.6 | MuSPAC and Dispersion in a Simple Two Layered Model | 80 |
| 4.6.1 | Introduction and Experimental Setup | 80 |
| 4.6.2 | Results | 82 |
| 4.6.3 | Discussion | 86 |
| 4.7 | MuSPAC and Body Wave Contamination in a Complex 31 Layer Model | 88 |
| 4.7.1 | Introduction and Experimental Setup | 88 |
| 4.7.2 | Results | 89 |
| 4.7.3 | Discussion | 92 |
| 4.8 | MuSPAC and Partial-Band Data in a Complex 32 Layered Model . . | 93 |
| 4.8.1 | Introduction and Experimental Setup | 93 |
| 4.8.2 | Results and Discussion of Synthetic Shot Records | 95 |
| 4.8.3 | Results and Discussion for MuSPAC and Full-Band Data . . . | 98 |
| 4.8.4 | Results and Discussion for MuSPAC and Partial-Band Data . | 100 |
| 4.9 | Deadhorse Lake Field Site | 107 |
| 4.9.1 | Introduction | 107 |
| 4.9.2 | Results: Background Data | 109 |
| 4.9.3 | Discussion: Background Data | 113 |
| 4.9.4 | Introduction: MuSPAC Field Analysis | 119 |
| 4.9.5 | Results: MuSPAC Field Analysis | 120 |
| 4.9.6 | Discussion: MuSPAC Field Analysis | 132 |
| 4.10 | Conclusions | 139 |
| | FUTURE WORK | 141 |
| | REFERENCES | 144 |

LIST OF TABLES

| | | |
|-----|--|----|
| 3.1 | Seismic acquisition parameters. | 46 |
| 4.1 | Glossary of mathematical terms used. | 57 |

LIST OF FIGURES

| | | |
|-----|--|---|
| 1.1 | <p>Top Right: State of Colorado map showing the relative locations between Chaffee County, Mount Princeton, and Denver. Bottom Right: A topographic map of the Upper Arkansas basin located in Chaffee County superimposed with the the two study sites, 'FOP' and 'DHL'. Left: A schematic map showing faults mapped along the Sawatch Range according to Scott <i>et al.</i> (1975), Colman <i>et al.</i> (1985), and Miller (1999).</p> | 2 |
| 2.1 | <p>(A) Tectonic map of the Puget Lowland and Olympic Peninsula modified from Blakely <i>et al.</i> (2009). The yellow arrow shows the regional direction of strain relative to North America (McCaffrey <i>et al.</i>, 2007). FCF-Frigid Creek fault; HRF-Hurricane Ridge Fault; OF-Olympia Fault; OU-Olympia uplift; SB-Seattle basin; SF-Seattle Fault; SMF-Saddle Mountain Fault (East and West faults); SMDZ-Saddle Mountain deformation zone; SU-Seattle Uplift; TB-Tacoma basin; TF-Tacoma Fault. Other regional faults not referred to in this research but shown in this figure are: CRF-Canyon River Fault; DMF-Devils Mountain Fault; EB-Everett basin; KA-Kingston arch; LRF-Leech River Fault; RMF-Rattlesnake Mountain Fault; SCF-Straight Creek Fault; SWIF-southern Whidbey Island Fault; WRF-White River Fault. (B) Geologic map modified from Schuster (2005) and Blakely <i>et al.</i> (2009).</p> | 7 |

2.2 (A) Regional aeromagnetic anomaly map of the study area produced by upward continuing the reduced to the pole aeromagnetic data by 4 km and then subtracting the result from the original grid. Data were acquired by the U.S. Geological Survey (Blakely *et al.*, 1999). FCF-Frigid Creek Fault; HRF-Hurricane Ridge Fault; OF-Olympia Fault; OU-Olympia uplift; SB-Seattle basin; SFZ-Seattle Fault Zone; SMDZ-Saddle Mountain deformation zone; SMF-Saddle Mountain fault (East and West); SU-Seattle Uplift; TB-Tacoma basin; TF-Tacoma Fault; DW-Dewatto seismic line; DL-Dewatto magnetic lineament; CI-Carr Inlet. The A-A line represents the transect used by Blakely *et al.* (1999) in their potential field modeling. The B-B line represents the transect used in this paper to investigate the Dewatto magnetic lineament using potential-field modeling methods. (B) Isostatic gravity anomaly map derived from data acquired and processed by the U.S. Geological Survey. (C) Left panel shows the track-lines for the marine magnetic survey in Hood Canal. The middle and right panels show a comparison between the magnetic anomaly data acquired from a boat and an aircraft, respectively. 10

2.3 Map showing seismic and potential field data interpretations overlaid on both gray hillshaded LiDAR (light detection and ranging) data and transparent color magnetic anomaly data. See Figure 2.1B for figure boundaries. The aeromagnetic anomaly data acquired in Hood Canal has been overlaid with the marine magnetic survey anomaly data and is outlined using a dashed line. The diversions of the Big Beef channel and Anderson creek are also shown. A1, A2, A3, and A4-interpreted anticlines; S1, S2, S3, S4, and S5-interpreted synclines; F1, F2, F3, and F4-interpreted faults; Line84-Hood Canal seismic line; Line91-Hood Canal seismic line; CO-Coho Rd. seismic line; BB-Big Beef Rd. seismic line; FM-Feather-Minnig Rd. seismic line; HI-Hite Rd. seismic line; SR-State Route 101 seismic line; SFZ-Seattle Fault Zone. Numbers adjacent to the Line84 and Line91 seismic profiles are common depth point numbers. 16

2.4 (A) Unmigrated and uninterpreted seismic section for the Big Beef Rd. (BB) seismic line including the locations and depths of three water wells used to make our interpretations. Seismic line locations are shown in Figure 2.3. (B) Unmigrated and uninterpreted seismic section for the Coho Rd. (CO) seismic line located approximately 500 m west of the BB seismic line. (C) Unmigrated and uninterpreted seismic section for the HI seismic line including the locations and depths of two water wells used to make our interpretations. 17

| | | |
|-----|--|----|
| 2.5 | (A) Time migrated, time-depth converted, and interpreted seismic section for the Big Beef Rd. (BB) seismic line. Line locations are shown in Figure 2.3. A1-interpreted anticline; S1-interpreted syncline; F1-interpreted south-dipping thrust fault; See legend for additional explanations. (B) Time migrated, time-depth converted, and interpreted seismic section for the Coho Rd. (CO) seismic line. A1-interpreted anticline; S1-interpreted syncline; F1-interpreted south-dipping thrust fault; (C) Time migrated, time-depth converted, and interpreted seismic section for the Hite Rd. (HI) seismic line. | 18 |
| 2.6 | (A) Unmigrated and uninterpreted seismic section for the State Route 101 (SR) seismic line. Line locations are shown in Figure 2.3. (B) Time migrated, time-depth converted, and interpreted seismic section for the SR seismic line. A1-interpreted anticline; See legend for additional explanations. (C) Unmigrated and uninterpreted seismic section for the Feather-Minnig Rd. (FM) seismic line. (D) Time migrated, time-depth converted, and interpreted seismic section for the FM seismic line. A1 and A2-interpreted anticlines; S2 and S3-interpreted synclines; F2-interpreted south-dipping thrust fault. | 19 |

| | | |
|-----|--|----|
| 2.7 | <p>(A) Time migrated, time-depth converted, and uninterpreted seismic section for the Hood Canal seismic lines 84 and 91 shown in Figure 2.3.</p> <p>(B) Reduced to the pole aeromagnetic (blue) and marine/ground magnetic (red) anomaly values that correspond with the location of the Hood Canal seismic lines 84 and 91.</p> <p>(C) Time migrated, time-depth converted, and interpreted seismic section for the Hood Canal seismic lines 84 and 91. A1, A2, A3, and A4-interpreted anticlines; S2, S3, S4, and S5-interpreted synclines; F2, F3, and F4-interpreted faults. See legend for additional explanations.</p> | 25 |
| 2.8 | <p>(A) and (B) The calculated and observed anomalies using forward modeling for the 45 km long Dewatto transect B-B' shown in Figure 2.2A. The model extends to infinity in both directions perpendicular to the profile.</p> <p>(C) The magnetic and density distributions used to interpret the geological structure from the forward model where $\Delta\rho$ is the density contrast in kg/m³ relative to normal crust (2670 kg/m³) and χ is the magnetic susceptibility in SI units. The modeled thrust fault is termed the Dewatto Fault.</p> <p>(D) Seismic section for the 7.5-km-long Dewatto profile (DW) shown in Figures 2.2A and 2.2B that runs E-W across the western margin of the Seattle Uplift (SU). This cross section shows $\sim 20^\circ$ west-dipping tilt in the interpreted Pliocene and younger sedimentary deposits and the more severe $\sim 6^\circ$-80° tilting of west-dipping Oligocene-Miocene sedimentary rocks below 0.6 km. . . .</p> | 30 |

| | | |
|-----|--|----|
| 2.9 | <p>Summary interpretation of the western portions of Seattle Fault zone. Rainbow colors indicate reduced-to-the-pole magnetic anomaly field intensity. The yellow arrow shows the regional direction of strain relative to North America (Mazzotti <i>et al.</i>, 2002; McCaffrey <i>et al.</i>, 2007). Solid black lines show previously mapped faults while structures introduced in this paper are marked in red. The two blue lines represent the location of the Coho Rd. (CO) and Big Beef Rd. (BB) seismic lines; DF-Dewatto Fault; F2-Thrust fault (Figures 2.3, 2.6, and 2.7); FCF-Frigid Creek Fault; GM-Green Mountain; HRF-Hurricane Ridge Fault; OF-Olympia Fault; OU-Olympia uplift; SB-Seattle basin; SFZ-Seattle Fault Zone; SMDZ-Saddle Mountain deformation zone as interpreted from magnetic data (Blakely <i>et al.</i>, 2009); SMF-Saddle Mountain fault (East and West); TB-Tacoma basin; TF-Tacoma Fault.</p> | 34 |
| 3.1 | <p>Major fault systems and Long’s Field located at the north-west corner of Mount Princeton Hot Springs Resort where the 3-D seismic, self-potential, and DC resistivity surveys were conducted. The rainbow colors represent self-potential anomalies in mV with high (red) values indicating upwelling ground water and low values (blue) representing downwelling ground water. The self-potential anomaly data is overlaid with the 3-D seismic survey shot points that are shown in more detail in Figure 3.2.</p> | 43 |

| | | |
|-----|--|----|
| 3.2 | Long’s Field, located at the north-west corner of Mount Princeton Hot Springs Resort where the 3-D seismic, self-potential, and DC resistivity surveys were conducted. The rainbow colors represent self-potential anomalies in mV with high and low values representing upwelling and downwelling ground water respectively. The self-potential anomaly data is overlaid with the 3-D seismic survey grid that shows the nomenclature used for inline and crossline receiver and shot stations and the lines along which velocity tomograms were modeled (dashed lines). The map also shows a 2-D DC resistivity profile which traversed in a north-northwest direction across the eastern portions of the field. Fault A shown to strike in an east-west direction across the field is based upon work by Richards <i>et al.</i> (2010). | 45 |
| 3.3 | Panel A shows the DC resistivity inversion result for the DC resistivity line. Panels B and C show the self-potential and 2-D refraction tomography results for L15i. Line locations are shown in Figures 3.1 and 3.2 | 48 |
| 3.4 | A shot gather on L15i at station 53 showing a step-up in the bedrock refraction at station 91 that is common to many of the shots shooting northwards in the eastern half of Long’s field. | 49 |
| 3.5 | Panels A, B and C show the self-potential and 2-D refraction tomography results for lines L31i, L45i and L55i (see Figure 3.2). Our interpreted location of Faults A through D are shown on each of the three panels along with a shot gather from station 55 on line L31i. | 50 |

| | | |
|-----|---|----|
| 3.6 | Figure showing the elevation above sea level for the 3250 m/s velocity isosurface using the 3-D tomography code. The figure is overlaid with our joint seismic, 2-D refraction, DC resistivity, and self-potential interpretations. The 3250 m/s velocity isosurface is interpreted to represent the top of the altered quartz monzonite where high elevation is represented by red and low elevation by blue. The bedrock surface elevation is overlaid with the 3-D seismic survey grid that shows the 2-D tomogram and resistivity profile locations. The subdued colors bordering the 3-D refraction results represent areas of low ray coverage for which the calculated velocities are not well constrained and therefore interpreted with caution. | 51 |
| 3.7 | Figure showing our interpretations superimposed on the self-potential anomaly map. The figure is overlaid with the 3-D seismic survey grid that shows the 2-D tomogram and resistivity profile locations. | 52 |
| 4.1 | The vertical component $U_z(r, t)$ recorded by four receivers for a source located at the first receiver (0 m offset). The source swept from 0 to 150 Hz in 12 s. Only the first second of the time record is shown for viewing purposes. | 60 |
| 4.2 | The causal Green's function, $G_{zz}(2, 3, t)$, found by cross-correlating the vertical wavefield components of $U_z(r, t)$ at receivers 2 and 3 with a separation distance of 50m. The center of the pulse arrives at $t = 0.125$ s, which indicates a Rayleigh-wave velocity of 400 m/s. | 62 |
| 4.3 | The SPAC coefficients $\phi_{zz}(2, 3, f)$ that are the real part of the Fourier transform of $G_{zz}(2, 3, t)$ | 63 |

| | | |
|-----|--|----|
| 4.4 | The zero crossings of the real part of the Fourier transform of the correlation between receivers 2 and 3 to estimate the wave speed as a function of frequency. | 64 |
| 4.5 | The semi-transparent and full-color SPAC coefficients, ϕ_{zz} , ϕ_{zx} , ϕ_{xz} , and ϕ_{xx} are for full-band and partial-band data respectively. | 66 |
| 4.6 | The semi-transparent and full color dispersion curves c_{xx} and c_{xz} are for full-band and partial-band data respectively. A sinusoidal chirp sweep from 0 to 150 Hz was used to impart a wavefield into a slab model that was recorded by receivers spaced 25-m apart. The effect of adding up to 6 missing zero crossings ($m=6$) on the partial-band data is shown with $m_{xx} = 3$ and $m_{xz} = 4$ resulting in a match between the partial-band and full-band dispersion curves. | 67 |
| 4.7 | A schematic of the single layered slab model used to parameterize the SEM model. | 72 |
| 4.8 | The vertical component of a synthetic shot record, U_z , as a function of source-detector offset. The source used is Ricker wavelet with a dominant frequency of 30 Hz. Interpretations of the main wavefield events are shown to the right and left of the shot record. | 74 |
| 4.9 | Cross-correlations of the vertical component of wavefields for a virtual shot at station 20. Receivers 20 and 40 were used to compare single shot (dotted) and summed shot (solid) correlations. | 75 |

| | | |
|------|--|----|
| 4.10 | Cross-correlations of the vertical component of wavefields of receivers 20 and 40. The real part of the Fourier transform of SPAC coefficients, ϕ_{zz} , ϕ_{zx} , ϕ_{xz} , and ϕ_{xx} . | |
| | | 76 |
| 4.11 | Cross-correlations of the vertical component of wavefields of receivers 20 and 40. Middle: The real part of the Fourier transform of the cross-correlation of the vertical components. | 76 |
| 4.12 | Zero crossings of the real part of the Fourier transform of the cross-correlations between receivers 20 and 40 for all four components for a single source (top) and the sum of 11 sources (bottom). | 77 |
| 4.13 | A schematic of the 2 layered model used to parameterized the SEM model. | 81 |
| 4.14 | A synthetic shot record showing the radial component U_x for the two layered model. | 82 |
| 4.15 | The Green's functions $G_{zz}(60, 40, t)$, $G_{zx}(60, 40, t)$, $G_{xz}(60, 40, t)$, and $G_{xx}(60, 40, t)$ found by cross-correlating the vertical and radial wavefield components for the two layered model. | 83 |
| 4.16 | $\phi_{zz}(60, 40, f)$, $\phi_{zx}(60, 40, f)$, $\phi_{xz}(60, 40, f)$, and $\phi_{xx}(60, 40, f)$ for the two layered model. | |
| | | 84 |
| 4.17 | Phase velocity dispersion curves $c_{zz}(60, 40, f)$, $c_{zx}(60, 40, f)$, $c_{xz}(60, 40, f)$, and $c_{xx}(60, 40, f)$ for the two layered model. $\lambda_c \approx 12 m$ represents one wavelength at 48 Hz and $c_1 = 480$ m/s. Waves below 48 Hz increasingly sample the faster velocity of layer 2 with decreasing frequency. | 84 |

| | | |
|------|---|----|
| 4.18 | The solid line represents the average ϕ for all four coefficients. The primed $\phi_{zx'}$ and $\phi_{xz'}$ coefficients indicate that they have been rotated by -90 deg and 90 deg respectively to match the cosine function of the ϕ_{zz} and ϕ_{xx} coefficients. | |
| | | 85 |
| 4.19 | The solid black line shows the result of using the average ϕ to calculate phase velocity. | 85 |
| 4.20 | A schematic of the 31 layered model used to investigate how body waves effect our estimation of phase velocity. Two separate density profiles are used in the modeling and these are represented by dashed (increasing density with depth) and solid (decreasing density with depth) red lines. | 88 |
| 4.21 | A comparison of the Green's functions $G_{zz}(s_{16}, s_1, t)$ and $G_{xx}(s_{16}, s_1, t)$ for the 31 layer models with and without reflectivity. | 90 |
| 4.22 | A comparison of SPAC coefficients $\phi_{zz}(s_{16}, s_1, f)$ for the 31 layer models with and without reflectivity. | 90 |
| 4.23 | A comparison of phase velocities $c_{zz}(s_{16}, s_1, f)$ for the 31 layer models with and without reflectivity. | 91 |
| 4.24 | A schematic of the 32 layered model showing the P-wave (Vp) and S-wave (Vp) velocity profiles used to parameterized the SEM model. The corresponding Rayleigh wave velocity c is also shown and is based upon equations from White (1983). | 94 |

| | | |
|------|--|----|
| 4.25 | U_z for the 32 layer model with an offset of 10 m to the first receiver. A Dirac source was used and a bandpass filter from 1 to 90 Hz was applied. Receiver separation is 2 m. | 96 |
| 4.26 | U_x for the 32 layer model with an offset of 10 m to the first receiver. A Dirac source was used and a bandpass filter from 1 to 90 Hz was applied. Receiver separation is 2 m. | 96 |
| 4.27 | A numerical virtual shot gather of $G_{zz}(r, s_2, t)$ for the 32 layer model. A Dirac source was used and a bandpass filter from 1 to 90 Hz was applied. The virtual shot position is at receiver 2 and is created by summing together the cross-correlations between 23 real shots. The real shots are located to the left of the first receiver and have an offset range of 58 to 10 m with interval spacings ranging from 2 to 4 m. . . | 97 |
| 4.28 | A numerical virtual shot gather of $G_{xx}(r, s_2, t)$ for the 32 layer model. The shot position is at receiver 2 and is created by summing together the cross-correlations between 23 real shots. The real shots are located to the left of the first receiver and have an offset range of 58 to 10 m with interval spacings ranging from 2 to 4 m. | 97 |
| 4.29 | Full-band Green's functions $G(s_{16}, s_2, t)$ for the 32 layer model. The Green's functions were created using the virtual shot gathers and summing over all receiver pairs that have $r = 28$ m. | 98 |
| 4.30 | Full-band SPAC coefficients $\phi(s_{15}, s_1, f)$ for the 32 layer model with $r = 28$ m. | 99 |

| | | |
|------|---|-----|
| 4.31 | Full-band phase velocity dispersion curves $c(s_{15}, s_1, f)$ for the 32 layer model with $r = 28 m$. The curves show the effect of adding zero crossings in intervals of 2. The differences in m between components is related to the requirement that the first crossing direction must follow either a cosine or sine function as demonstrated by the homogeneous half-space examples. | 101 |
| 4.32 | Partial-band Green's functions $G(s_{15}, s_1, t)$ for the 32 layer model. The Green's functions were created using the virtual shot gathers and summing over all receiver pairs that have $r = 28 m$ | 102 |
| 4.33 | A comparison of the full-band and partial-band Green's functions $G_{xx}(s_{15}, s_1, t)$ for the 32 layer model. | 103 |
| 4.34 | Partial-band SPAC coefficients $\phi(s_{15}, s_1, f)$ for the 32 layer model where only frequencies of 29 Hz and up are band passed. 104 | |
| 4.35 | A comparison of the full-band and partial-band SPAC coefficients $\phi_{xx}(s_{15}, s_1, f)$ for the 32 layer model. | 104 |
| 4.36 | Partial-band phase velocity dispersion curves $c(s_{15}, s_1, f)$ for the 32 layer model where only frequencies of 29 Hz and up are band passed. The curves show the effect of adding zero crossings in intervals of 2. . | 105 |
| 4.37 | A comparison of the full-band and partial-band dispersion curves using the $c_{zz}(s_{15}, s_1, f)$ curve. This shows that five missed zero crossings must be added to the partial-band curves in order to retrieve the correct phase velocities. | 106 |

| | | |
|------|--|-----|
| 4.38 | The DHL study site showing water wells and their temperatures, the location of the seismic lines, and overlaid with the results of a gravity survey we acquired. | 108 |
| 4.39 | Left panel: Vertical seismic profile at MG-1 using a zero offset sledge hammer source and a hydrophone string with 1 m receiver spacings. Right panel: A zoomed in portion of the left panel, designated by the dashed box, that highlights the difficulty of interpreting the near-surface wavefields due to interference from waves related to the steel well casing and water. The letters are associated to dominant wavefield events that we interpret as: A, unsaturated sediments with $V_p=600$ m/s; B, saturated sediments with $V_p=1800$ m/s; C, altered quartz monzonite with $V_p=2400-3600$ m/s; D, granite with $V_p=3600-4400$ m/s; E, borehole steel casing with $V_p=5500$ m/s; F1, water wave radiating from the steel casing with $V_p=1433$ m/s; F2, water wave originating from the top of the well with $V_p=1433$ m/s. | 110 |
| 4.40 | U_{xx} shot record acquired using a radial source at shot position 161 and recorded by radial receivers spaced 2 m apart from 161 to 220. The shot gather has been trace normalized. | 112 |
| 4.41 | U_{zx} shot record acquired using a radial source at shot position 161 and recorded by vertical receivers spaced 2 m apart from 161 to 220. The shot gather has been trace normalized. | 112 |
| 4.42 | U_{zz} shot record acquired using a vertical source at shot position 161 and recorded by vertical receivers spaced 2 m apart from 161 to 220. The shot gather has been trace normalized. | 112 |

| | | |
|------|--|-----|
| 4.43 | Velocity profile results from a refraction tomography analysis along the seismic acquisition line represented as the solid and dashed line in Figure 4.38. First breaks were picked from the correlated U_{zz} shot gathers extending from stations 1 to 236. | 113 |
| 4.44 | Interpretation along the seismic acquisition line extending from stations 1 to 236 in Figure 4.38. The interpretation is based upon refraction tomography velocities, VSP velocities, single shot gather interpretations, gravity data, and the well-log for borehole MG-1. | 118 |
| 4.45 | $G_{xx}(r, s_{162}, t)$ virtual shot record located at station 162. The virtual shot is calculated using cross-correlations of the uncorrelated sweep field data. The virtual shot gather has been trace normalized. | 120 |
| 4.46 | $G_{zz}(r, s_{162}, t)$ virtual shot record located at station 162. The virtual shot is calculated using cross-correlations of the uncorrelated sweep field data. The virtual shot gather has been trace normalized. | 120 |
| 4.47 | A comparison of Green's functions calculated from correlated and uncorrelated sweep data. Top muted $G_{zz}(s_{180}, s_{165}, t)$ and $G_{xz}(s_{180}, s_{165}, t)$ with a receiver separation of $r = 30$ m have been used. | 121 |
| 4.48 | A comparison of SPAC coefficients calculated from correlated and uncorrelated sweep data. Top muted SPAC coefficients $\phi_{zz}(s_{190}, s_{162}, f)$ and $\phi_{xz}(s_{180}, s_{165}, f)$ with a receiver separation of $r = 30$ m have been used. The $\phi_{xz}(s_{180}, s_{165}, f)$ components show a difference of 1 Hz for their crossings between 28 and 30 Hz. X and X' shown in the inset box represent the shift in the fifth zero crossing to a higher frequency between the uncorrelated and correlated vibroseis data respectively. . | 122 |

| | | |
|------|--|-----|
| 4.49 | A comparison of velocity dispersion curves showing the differences between using correlated and uncorrelated sweep data. $m = 3$ for both components. | 123 |
| 4.50 | Un-muted Green's functions $G(s_{176}, s_{162}, t)$ for the field case where $r = 28 m$ | 125 |
| 4.51 | Top muted Green's functions $G(s_{176}, s_{162}, t)$ for the field case where $r = 28 m$ | 125 |
| 4.52 | Un-muted SPAC coefficients $\phi(s_{176}, s_{162}, f)$ for the field case where $r = 28 m$ | 126 |
| 4.53 | Top muted SPAC coefficients $\phi(s_{176}, s_{162}, f)$ for the field case where $r = 28 m$ | 126 |
| 4.54 | Top muted velocity dispersion curves $c(s_{176}, s_{162}, f)$ with a range of added zero crossings for the field case where $r = 28 m$. The semi-transparent and full color dispersion curves are for full-band and partial-band data respectively. The full-band curve E is based upon the 32 layer numerical model presented in the previous section. It shows that in our field case, that we have missed zero crossings as defined by $m_{zz, zx, xx} = 5$ and $m_{xz} = 6$ in the frequency range of 0-28 Hz where we did not sweep. | 127 |

4.55 Left panel: The lower panel shows a gather of cross-correlation coefficient traces for $\phi_{xx}(s_{n+R}, s_n, f)$ for the field case where $n = 168$ to 213 and $R = 14$ refers to a separation of 14 stations or $r = 28$ m. The dashed red line shows the 7th zero crossings which is in-turn a proxy for changing velocity. The phase velocity corresponding to the 7th zero crossings is shown in the top panel. Right panel: The bottom panel shows a gather of all four cross-correlation coefficient components summed together for each trace. It is for the same field case as the left panel. 128

4.56 Top muted Green's functions $G(s_{190}, s_{162}, t)$ for the field case where $r = 56$ m. 130

4.57 Top muted SPAC coefficients $\phi(s_{190}, s_{162}, f)$ for the field case where $r = 56$ m. 130

4.58 Top muted velocity dispersion curves $c(s_{190}, s_{162}, f)$ with a range of added zero crossings for the field case where $r = 56$ m. The semi-transparent and full color dispersion curves are for full-band and partial-band data respectively. The full-band curve E is based upon the 32 layer numerical model presented in the previous section. It shows that in our field case, that we have missed zero crossings as defined by $m_{zz, zx, xx} = 5$ and $m_{xz} = 6$ in the frequency range of 0-28 Hz where we did not sweep. 131

CHAPTER 1:

INTRODUCTION

The first section of this dissertation (Chapter 2) examines the Western extents of the Seattle fault in Washington State, while the second section (Chapters 3 and 4) investigates a geothermal system situated at Mount Princeton in Colorado.

1.1 Introduction to the Western Extents of the Seattle Fault in Washington State

In Chapter 2, we present evidence that the Seattle Fault Zone, in Washington State, extends west beyond the Seattle basin to form a >100-km-long active fault zone (Lamb *et al.*, 2012a). This fault system and its active links pass under the urban centers of Seattle and Tacoma that have a combined population of approximately 3.5 million people. The last known rupture that occurred on this system was a M7 earthquake approximately 1,100 years ago. This earthquake caused the hanging wall of the Seattle fault to lift by 6.5 m and generated a local tsunami and landslides. The accurate characterization of this fault system, and the magnitude earthquake that it can support, is essential for improving risk and earthquake hazard assessments in the region. We use a combination of magnetic, gravity, and seismic data in conjunction with geologic maps to show that the fault does extend further to the west by a minimum of 20 km with the potential to extend across Hood Canal and connect with faults in the eastern margin of the Olympic Mountains.

1.2 Introduction to the Mount Princeton Geothermal System in Central Colorado

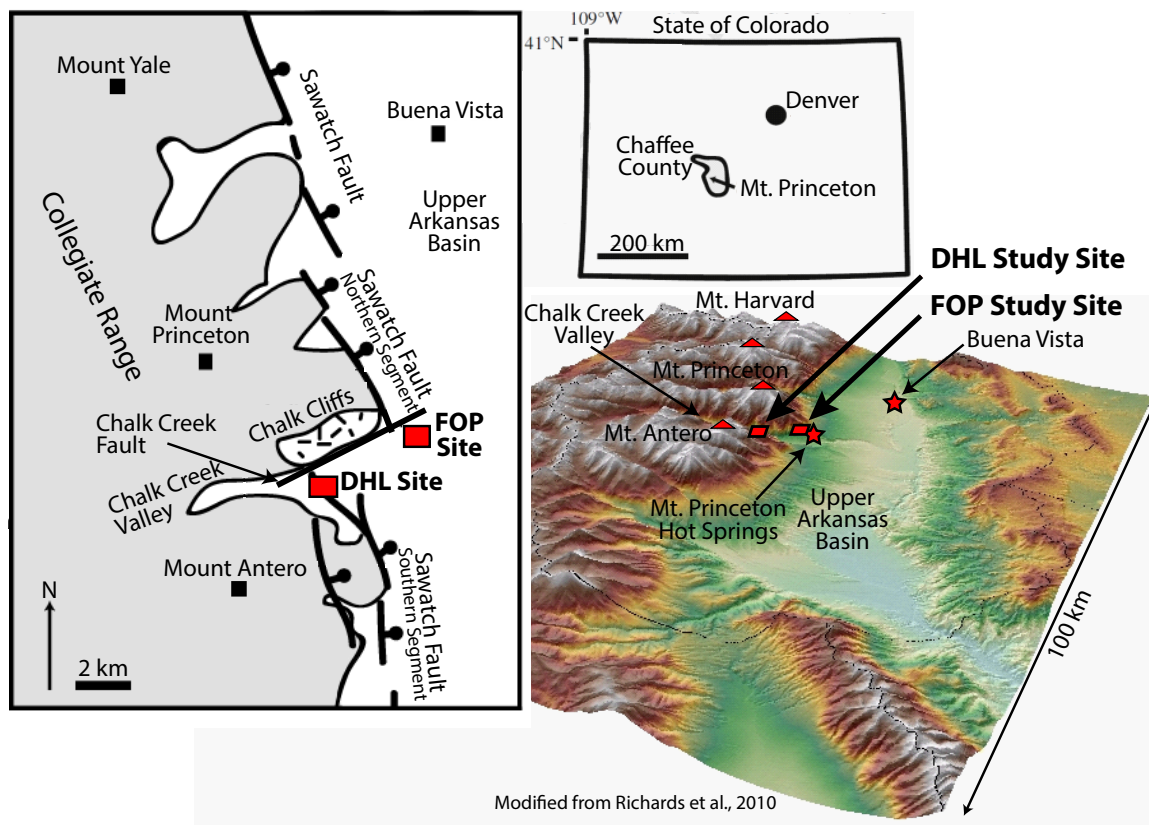


Figure 1.1: Top Right: State of Colorado map showing the relative locations between Chaffee County, Mount Princeton, and Denver. Bottom Right: A topographic map of the Upper Arkansas basin located in Chaffee County superimposed with the two study sites, 'FOP' and 'DHL'. Left: A schematic map showing faults mapped along the Sawatch Range according to Scott *et al.* (1975), Colman *et al.* (1985), and Miller (1999).

The Upper Arkansas Valley in the Rocky Mountains of central Colorado is the northernmost extensional basin of the Rio Grande Rift (Figure 1.1). The valley is a half-graben bordered to the east and west by the Mosquito and Sawatch Ranges,

respectively (McCalpin and Shannon, 2005). The Sawatch Range is home to the Collegiate Peaks, which include some of the highest summits in the Rocky Mountains. Some of the Collegiate Peaks over 4,250 m (14,000 ft) from north to south include Mount Harvard, Mount Yale, Mount Princeton, and Mount Antero. The Sawatch Range-front normal fault strikes north-northwest along the eastern margin of the Collegiate Peaks and is characterized by a right-lateral offset between the Mount Princeton batholith and Mount Antero. This offset in basin bounding faults is accommodated by a northeast-southwest dextral strike slip transfer fault (Richards *et al.*, 2010) and coincides with an area of hydrogeothermal activity and Mount Princeton Hot Springs. This transfer fault is here termed the 'Chalk Creek fault' due to its alignment with the Chalk Creek valley. A 250 m high erosional scarp, called the Chalk Cliffs, lies along the northern boundary of this valley. The cliffs are comprised of geothermally altered quartz monzonite and not chalk (Miller, 1999). These cliffs coincide with the Chalk Creek fault, whose intersection with the Sawatch Range-front normal fault results in a primary pathway for upwelling geothermal waters (Richards *et al.*, 2010).

Faults can form rapid transport pathways for deep heated geothermal fluids (Fairley and Hinds, 2004) and surface expression of these fluids in the form of hot springs often appear at intersecting fault systems (Smith *et al.*, 2002; Glen *et al.*, 2008). The Mount Princeton Hot Springs, located near the intersection of the Sawatch Range-front normal fault and Chalk Creek fault (Figure 1.1), is an example of a geothermal system controlled by intersecting faults. Mapping these faults and associated fractures will help to improve our understanding of the geothermal system and to determine its potential as an economic resource. We use a range of geophysical data to investigate

the subsurface features in this region that are potential flow pathways for fluids.

Next, we describe the applied geophysical methods and present the research questions. In Chapters 3 and 4, we analyze and integrate geophysical data that we acquired at Mount Princeton Hot Springs to characterize faults within Chalk Creek and the near surface surrounding them. In Chapter 3, we use traditional geophysical methods (self-potential, dc resistivity, seismic) to investigate an upwelling event in a site called the Field of Pain (FOP in Figure 1.1) that is interpreted as the source for the Mount Princeton Hot Spring (Lamb *et al.*, 2012b). In Chapter 4, we investigate a dry lake bed called Deadhorse lake (DHL in Figure 1.1) and its environs where a number of wells produce hot water. We use active source multicomponent data to present a new technique that incorporates surface waves recorded on radial and vertical receiver components. We extend the Spatial Autocorrelation (SPAC) method (Aki, 1957) to improve surface wave velocity dispersion estimates. Existing methods to retrieve vital near-surface properties generally use only the vertical components of the wavefield. We demonstrate the advantages of the Multi-Component SPAC, here termed MuSPAC, by applying our method to numerical elastic wave simulations for a known source and earth model of increasing complexity. We then apply this method to a field case and examine how successfully we can retrieve the velocity structure of the earth model.

CHAPTER 2:

WESTERN LIMITS OF THE SEATTLE FAULT ZONE AND ITS INTERACTION WITH THE OLYMPIC PENINSULA, WASHINGTON

2.1 Summary

We present evidence that the Seattle Fault Zone of Washington State extends to the west edge of the Puget Lowland and is kinematically linked to active faults that border the Olympic Massif, including the Saddle Mountain deformation zone. We acquired new high-resolution seismic reflection and marine magnetic data that suggest the Seattle Fault Zone extends west beyond the Seattle basin to form a >100-km-long active fault zone. We provide evidence for a strain transfer zone, expressed as a broad set of faults and folds, connecting the Seattle and Saddle Mountain deformation zones near Hood Canal. This connection provides an explanation for the apparent synchronicity of M7 earthquakes on the two fault systems approximately 1,100 years ago. We redefine the boundary of the Tacoma basin to include the previously termed Dewatto basin and show that the Tacoma Fault, the southern part of which is a backthrust of the Seattle Fault Zone, links with a previously unidentified fault along the western margin of the Seattle Uplift. We model this north-south fault, termed the Dewatto Fault, along the western margin of the Seattle Uplift as a low-angle thrust that initiated with exhumation of the Olympic Massif and today accommodates north-

directed motion. The Tacoma and Dewatto faults likely control both the southern and western boundary of the Seattle Uplift. The inferred strain transfer zone linking the Seattle Fault Zone and Saddle Mountain deformation zone defines the northern margin of the Tacoma basin, and the Saddle Mountain deformation zone forms the northwestern boundary of the Tacoma basin. Our observations and model suggest that the western portions of the Seattle Fault Zone and Tacoma Fault are complex, require temporal variations in principal strain directions, and cannot be modeled as a simple thrust/backthrust system.

2.2 Introduction

Oblique subduction of the Juan de Fuca plate beneath the North American continent results in northeast migration of coastal regions of Washington State relative to stable North America. This northeast motion is resisted by Mesozoic and older rocks that form the stable craton of southwest Canada, resulting in shortening of the Puget Lowland region of Washington State (Wells *et al.*, 1998; Mazzotti *et al.*, 2002; McCaffrey *et al.*, 2007). This shortening is expressed, in part, as a series of northwest- and west-trending active faults that separate basins and structural uplifts beneath the Puget Lowland, within which are the Seattle and Tacoma metropolitan areas (Figure 2.1; Johnson *et al.*, 1996; Pratt *et al.*, 1997).

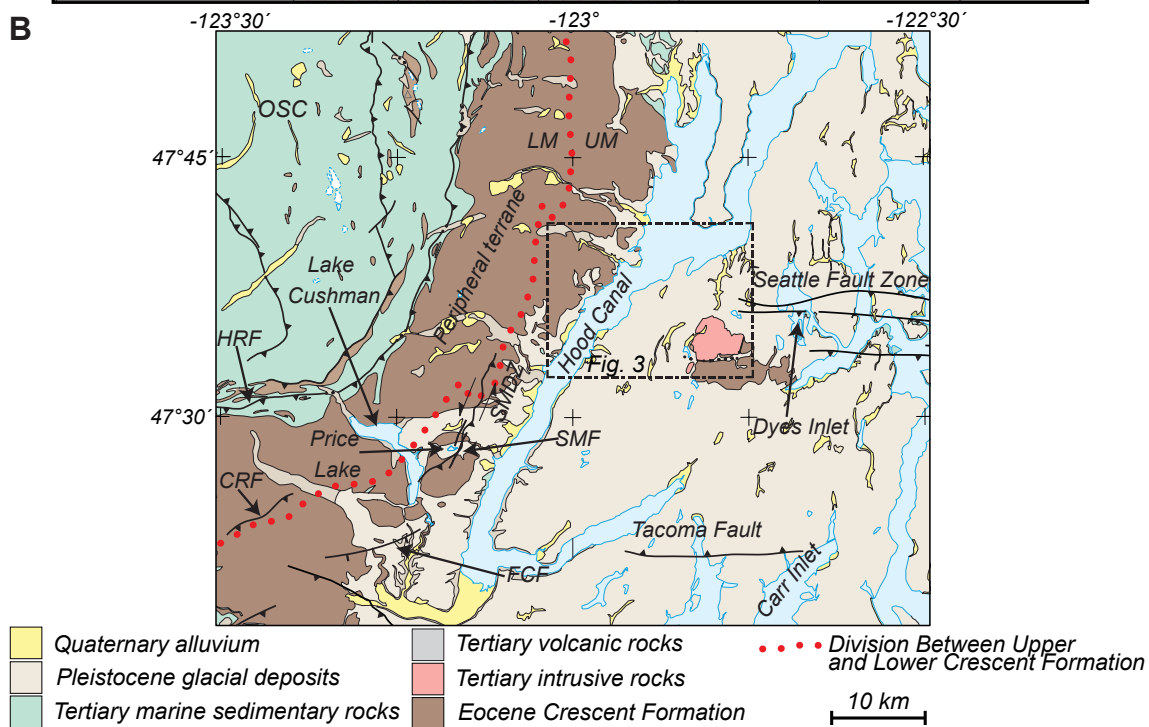
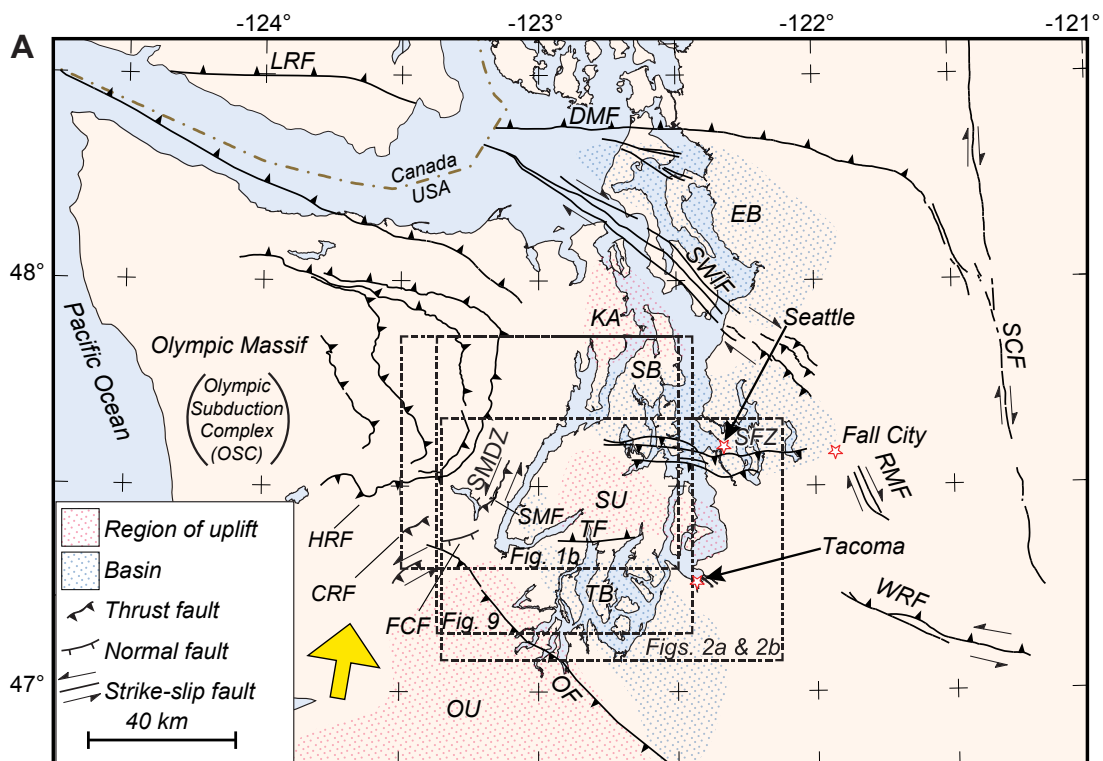


Figure 2.1: (A) Tectonic map of the Puget Lowland and Olympic Peninsula modified from Blakely *et al.* (2009). The yellow arrow shows the regional direction of strain relative to North America (McCaffrey *et al.*, 2007). FCF-Frigid Creek fault; HRF-Hurricane Ridge Fault; OF-Olympia Fault; OU-Olympia uplift; SB-Seattle basin; SF-Seattle Fault; SMF-Saddle Mountain Fault (East and West faults); SMDZ-Saddle Mountain deformation zone; SU-Seattle Uplift; TB-Tacoma basin; TF-Tacoma Fault. Other regional faults not referred to in this research but shown in this figure are: CRF-Canyon River Fault; DMF-Devils Mountain Fault; EB-Everett basin; KA-Kingston arch; LRF-Leech River Fault; RMF-Rattlesnake Mountain Fault; SCF-Straight Creek Fault; SWIF-southern Whidbey Island Fault; WRF-White River Fault. (B) Geologic map modified from Schuster (2005) and Blakely *et al.* (2009).

The Seattle basin and Tacoma basin extend eastward ~ 70 km from Hood Canal, beneath the Seattle/Tacoma urban corridor, to the foothills of the Cascade Range (Figure 2.1). The Seattle Uplift, separating the Seattle and Tacoma basins, is interpreted as a pop-up block above the south-dipping Seattle thrust fault to the north and the Tacoma backthrust to the south (Pratt *et al.*, 1997; Brocher *et al.*, 2001, 2004). Direct geologic evidence for the Seattle and Tacoma Fault systems is sparse, consisting primarily of uplifted bedrock terraces (Bucknam *et al.*, 1992; Kelsey *et al.*, 2008), topographic scarps observed in light detection and ranging (LiDAR) surveys that cover a large area of the Puget Lowland (e.g., Haugerud *et al.*, 2003; Sherrod *et al.*, 2004, 2008), and faults and folds found in detailed studies of trench excavations across LiDAR scarps (e.g., Nelson *et al.*, 2003; Sherrod *et al.*, 2004). Fault strands and underlying structures are inferred from seismicity, magnetic, gravity, geologic, and seismic-reflection data (e.g., Finn, 1990; Pratt *et al.*, 1997; Brocher *et al.*, 2001; Blakely *et al.*, 2002; Johnson *et al.*, 2004; Stephenson *et al.*, 2006; Liberty and Pratt, 2008; Sherrod *et al.*, 2008).

The ~ 70 km long Seattle Fault Zone is comprised of south-dipping thrust faults and interpreted north-dipping backthrusts that lie in part beneath the Seattle metropoli-

tan area (Figure 2.1). The shallow portion of this fault zone is comprised of a monocline that bounds the southern margin of the Seattle basin, and mapped faults and folds in the hanging wall just south of the monocline. The Seattle Fault Zone may extend to the east beyond the boundaries of the Seattle basin to merge with the active South Whidbey Island fault (Figure 2.1; Johnson *et al.* (1996); Liberty and Pratt (2008); Sherrod *et al.* (2008); Blakely *et al.* (2009)).

The Tacoma Fault on the south side of the Seattle Uplift is less well defined than the Seattle Fault. The Tacoma Fault extends ~ 20 km along the southern margin of the Seattle Uplift between Carr Inlet and the southeastern extent of Hood Canal (Figure 2.1B). The Tacoma Fault is along strike of the White River Fault (Figure 2.1A) that extends through the Cascade Range, but no direct evidence links these two fault systems (Blakely *et al.*, 2007, 2011). Field studies show that the Seattle and Tacoma faults are capable of causing large earthquakes (Atwater and Moore, 1992; Sherrod *et al.*, 2004), so knowing their overall lengths and their interactions with neighboring faults assist with understanding fault kinematics and earthquake hazards in this area. The most recent large rupture occurred on the Seattle Fault Zone in A.D. 900 to 930, producing a M7-7.5 earthquake that lifted the hanging wall ~ 6.5 m and generated a local tsunami and landslides (Atwater and Moore, 1992; Bucknam *et al.*, 1992; Jacoby *et al.*, 1992; Atwater and Hemphill-Haley, 1997; Sherrod *et al.*, 2000; ten Brink *et al.*, 2002). Trench studies across LiDAR scarps on the Tacoma and Saddle Mountain Faults (Figure 2.1) suggest similarly timed earthquakes (within the limits of radiocarbon dating) as the Seattle Fault Zone event 1,100 years ago and may be contemporaneous (e.g., Sherrod *et al.*, 2004, 2008; Blakely *et al.*, 2009).

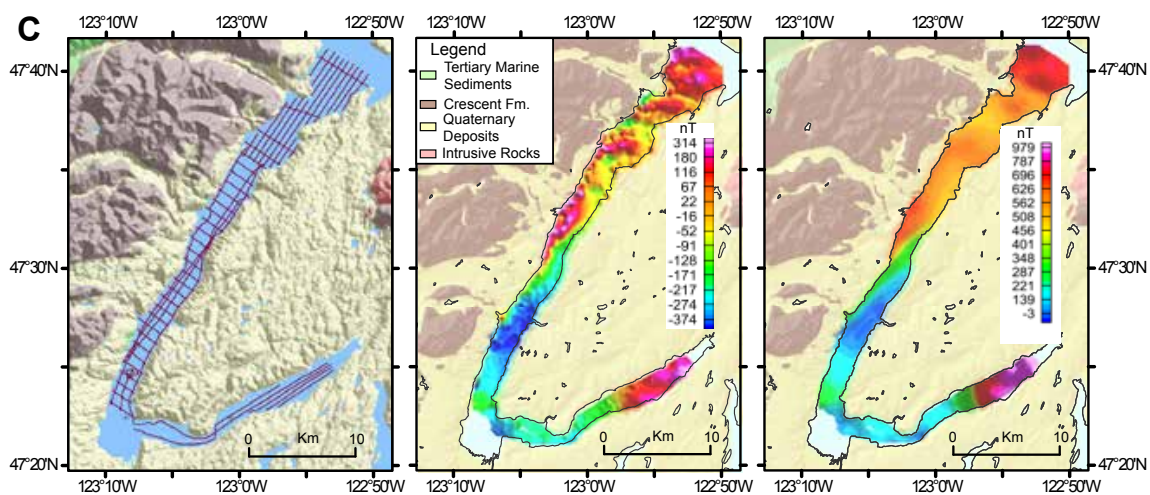
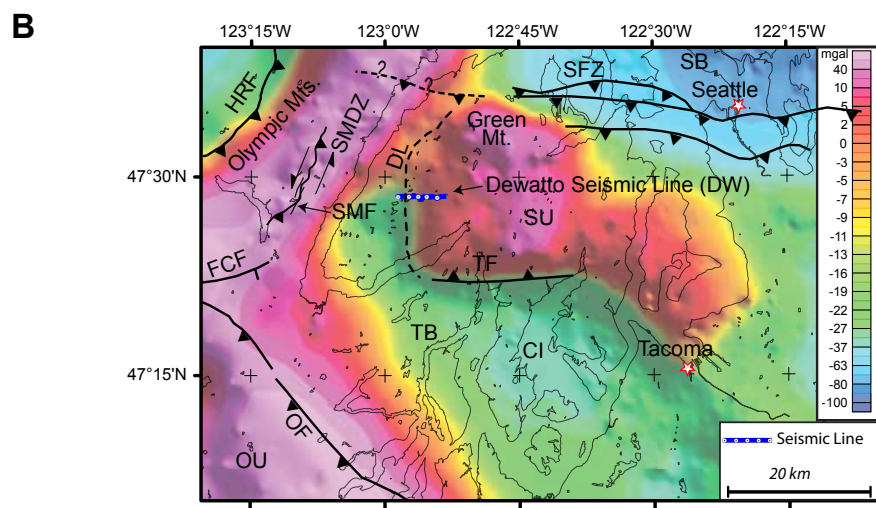
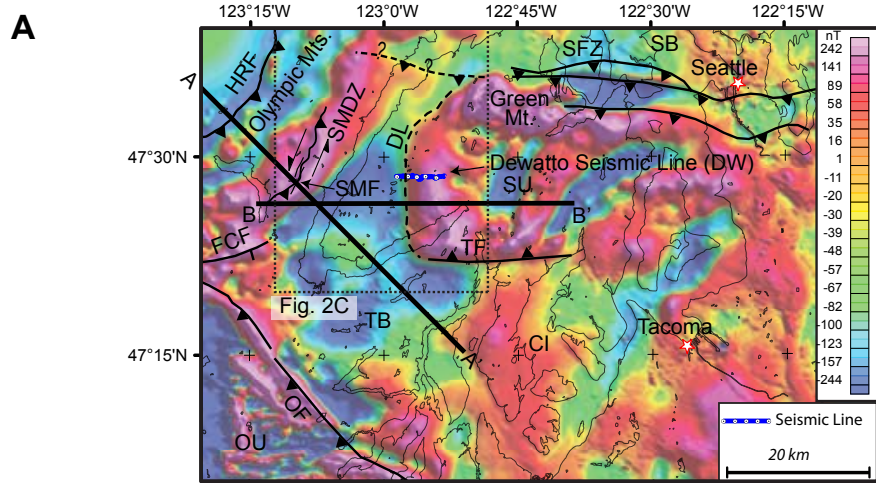


Figure 2.2: (A) Regional aeromagnetic anomaly map of the study area produced by upward continuing the reduced to the pole aeromagnetic data by 4 km and then subtracting the result from the original grid. Data were acquired by the U.S. Geological Survey (Blakely *et al.*, 1999). FCF-Frigid Creek Fault; HRF-Hurricane Ridge Fault; OF-Olympia Fault; OU-Olympia uplift; SB-Seattle basin; SFZ-Seattle Fault Zone; SMDZ-Saddle Mountain deformation zone; SMF-Saddle Mountain fault (East and West); SU-Seattle Uplift; TB-Tacoma basin; TF-Tacoma Fault; DW-Dewatto seismic line; DL-Dewatto magnetic lineament; CI-Carr Inlet. The A-A line represents the transect used by Blakely *et al.* (1999) in their potential field modeling. The B-B line represents the transect used in this paper to investigate the Dewatto magnetic lineament using potential-field modeling methods. (B) Isostatic gravity anomaly map derived from data acquired and processed by the U.S. Geological Survey. (C) Left panel shows the track-lines for the marine magnetic survey in Hood Canal. The middle and right panels show a comparison between the magnetic anomaly data acquired from a boat and an aircraft, respectively.

In this chapter, we explore the deformation caused by convergence across the Seattle Fault Zone and eastern portions of the Olympic Massif using new high-resolution seismic profiles and magnetic data between Hood Canal and Puget Sound (Figure 2.2). These new data cross the northwest and west flanks of the Seattle Uplift where structures may define the western limits of the Seattle Fault Zone. We integrate results from these newly acquired data with previously published geological and geophysical data to test whether there is a link between the Seattle Fault Zone and structures in the Olympic Massif to the west. Our interpretations suggest a kinematic linkage between several fault systems in the Puget Sound region, providing a possible explanation for synchronous ruptures of multiple faults during large earthquakes.

2.3 Geological and Geophysical Setting

The Olympic subduction complex, an exhumed part of the Cascadia accretionary wedge (Brandon *et al.*, 1998), lies west of the Puget Lowland and the Seattle Fault

Zone (Figure 2.1A). The complex is cored by severely deformed and metamorphosed Eocene to Miocene marine sedimentary rocks, which have been uplifted to form the Olympic Massif (Figure 2.1A). The sedimentary strata are thrust beneath peripheral rocks of the Siletz terrane, a largely volcanic terrane of oceanic affinity that forms the crystalline basement beneath most of the Cascadia forearc and reaches thicknesses of up to 35 km (Finn, 1990; Lees and Crosson, 1990; Trehu *et al.*, 1994; Parsons *et al.*, 1998). Exhumation of the Olympic subduction complex began at ca. 18 Ma (Brandon *et al.*, 1998). The Olympic subduction complex is bordered to the east by the uplifted portion of the Siletz terrane, marked by the Hurricane Ridge Fault (Brandon *et al.*, 1998). The regions of the Siletz terrane bordering Hood Canal host steeply east-dipping thrust faults including the Saddle Mountain and Hurricane Ridge Faults (Blakely *et al.*, 2009; Brandon *et al.*, 1998). These faults, along with the Frigid Creek and Canyon River faults, have been previously defined as elements of the Saddle Mountain deformation zone that accommodates northward shortening of the Puget Lowland crust east of the Olympic Massif (Blakely *et al.*, 2009). These faults also have components of vertical displacement that accommodate exhumation of the Olympic Massif (e.g., Wilson *et al.*, 1979; Brandon *et al.*, 1998; Witter *et al.*, 2008; Blakely *et al.*, 2009).

The Crescent Formation is a mafic volcanic component of the Siletz terrane, which is part of the Paleocene to Eocene Coast Range Volcanic Province (Babcock *et al.*, 1992; Hirsch and Babcock, 2009). The Crescent Formation is exposed along the north and east sides of the Olympic Massif (Figure 2.1B), where it can be subdivided into a lower member consisting of massive submarine basalt flows and an upper member of subaerial basalt with sparse sedimentary interbeds (Tabor and Cady, 1978a; Babcock

et al., 1992; Hirsch and Babcock, 2009). These two members represent an upward progression from an oceanic deep-water origin in the lower member to a coastal marine and terrestrial setting in the upper member. The Crescent Formation dips eastward from the Saddle Mountain deformation zone, and except for exposures in the Green Mountain uplift, is largely covered east of Hood Canal by Tertiary sedimentary rocks and glacial deposits of late Quaternary age beneath the Puget Lowland (Figures 2.1 and 2.2; Johnson *et al.*, 1994, 2004; Haeussler and Clark, 2000; Blakely *et al.*, 2009; Tabor *et al.*, 2011).

The Crescent Formation has been delineated beneath the Puget Lowland using aeromagnetic and gravity anomalies because of its high magnetic susceptibility and density (Finn, 1990; Babcock *et al.*, 1992; Blakely *et al.*, 2009). The upper member is more magnetic than the lower member and therefore is more evident in aeromagnetic data (Blakely *et al.*, 2009). The strong magnetic properties result in well-defined, linear magnetic anomalies where the Crescent Formation is folded or vertically displaced by faults, allowing potential field modeling of structures in the region (e.g., Dane *et al.*, 1965; Gower *et al.*, 1985; Blakely *et al.*, 1999, 2002; Brocher *et al.*, 2004; Johnson *et al.*, 2004; Blakely *et al.*, 2009). Northward motion of the Puget Lowland at rates of 4.4 ± 0.3 mm/yr (Mazzotti *et al.*, 2002; McCaffrey *et al.*, 2007) and clockwise rotation of the Cascadia Forearc at 1.5 ± 0.50 /m.y. (Wells *et al.*, 1998) have resulted in the formation of the 7 to 9 km deep Seattle basin, the 5 to 7 km deep Tacoma basin, and the ~ 25 km wide Seattle Uplift that separates the two basins (Figure 2.1; Johnson *et al.*, 1994; Pratt *et al.*, 1997; Brocher *et al.*, 2001; van Wagoner *et al.*, 2002; Johnson *et al.*, 2004). A number of tectonic models have been proposed for the Seattle Fault Zone and Tacoma Fault that bound the Seattle Uplift. The prevailing

view is that the Seattle Fault Zone is comprised of a blind, south-dipping thrust fault. Some models propose steep dip angles (Brocher *et al.*, 2001), while others propose shallower dip angles with penetration to detachment surfaces at depths of 14-20 km (Pratt *et al.*, 1997; ten Brink *et al.*, 2002; Johnson *et al.*, 2004). Brocher *et al.* (2001) and Johnson *et al.* (2004) suggest the Tacoma Fault is a 30°-45° dipping backthrust to the Seattle Fault Zone, while Brocher *et al.* (2004) interpret the Seattle Uplift as a passive-roof duplex with greater uplift rates on the west end of the Seattle Uplift compared to farther east. An overview of these models is presented in Mace and Keranen (2012) who also interpret a zone of recent northeast-southwest faulting that crosses the Seattle Basin and Seattle Uplift. They suggest that this northeast-southwest aligned faulting may be responsible for cyclic accommodation of eastward transport of the Olympic Massif and north-south shortening of the Washington block.

2.4 Western Extent of Seattle Fault Zone

The first evidence for Holocene displacement on the Seattle Fault Zone came from uplifted shorelines along Puget Sound, and accompanying tsunami deposits (Bucknam *et al.*, 1992; Atwater and Moore, 1992; Sherrod *et al.*, 2000; Nelson *et al.*, 2003). Subsequent trenching of fault scarps has confirmed Holocene earthquakes (Wilson *et al.*, 1979; Sherrod, 2001; Nelson *et al.*, 2003). The Seattle monocline marks the southern boundary of the Seattle basin and is formed by north-dipping Tertiary sedimentary rocks. The monocline extends westward from near Fall City to the north flank of Green Mountain, and apparently formed by north-south compression along the Seattle Fault Zone (Figure 2.1; Johnson *et al.*, 1999; Blakely *et al.*, 2002; Brocher *et al.*, 2004; Liberty and Pratt, 2008). The extension of deformation related to the Seattle

Fault Zone west of Puget Sound is inferred from geologic mapping near Green Mountain, seismic profiles in Dyes Inlet, and aeromagnetic lineations over the hanging wall (Johnson *et al.*, 1999; Haeussler and Clark, 2000; Blakely *et al.*, 2002; Tabor *et al.*, 2011). Farther west, Blakely *et al.* (2009) used potential field modeling and geologic mapping to suggest that the north-northwest-striking Saddle Mountain Fault on the Olympic Peninsula extends northward to near the projected western extension of the Seattle Fault Zone (Figure 2.2), and that west-trending magnetic lineations between the Saddle Mountain deformation zone and Seattle Fault Zone indicate that the two fault systems may be linked by structures extending beneath Hood Canal. Both of these fault systems produced large earthquakes approximately 1,000 to 1,100 yr ago (Atwater and Moore, 1992; Bucknam *et al.*, 1992; Jacoby *et al.*, 1992; Karlin and Abella, 1992; Schuster *et al.*, 1992), suggesting they may form a linked, >150 km long set of active fault systems (Hughes, 2005).

2.4.1 Geophysical Investigations

To characterize possible structural ties between the Seattle Fault Zone and Saddle Mountain deformation zone, we collected five high-resolution seismic reflection profiles across the western portion of the Seattle Fault Zone (Figure 2.3). We acquired all seismic data using a 200 kg accelerated weight drop source, a 120 channel seismic recording system, and a 5 m source and receiver spacing to produce a nominal 60 fold data set with source-receiver offsets as great as 600 m. All seismic profiles were acquired on roadways. Standard processing techniques (Yilmaz, 2001) were applied to produce the uninterpreted and interpreted seismic profiles presented in Figures 2.4 through 2.8. The velocity model derived from normal-moveout corrections was used to

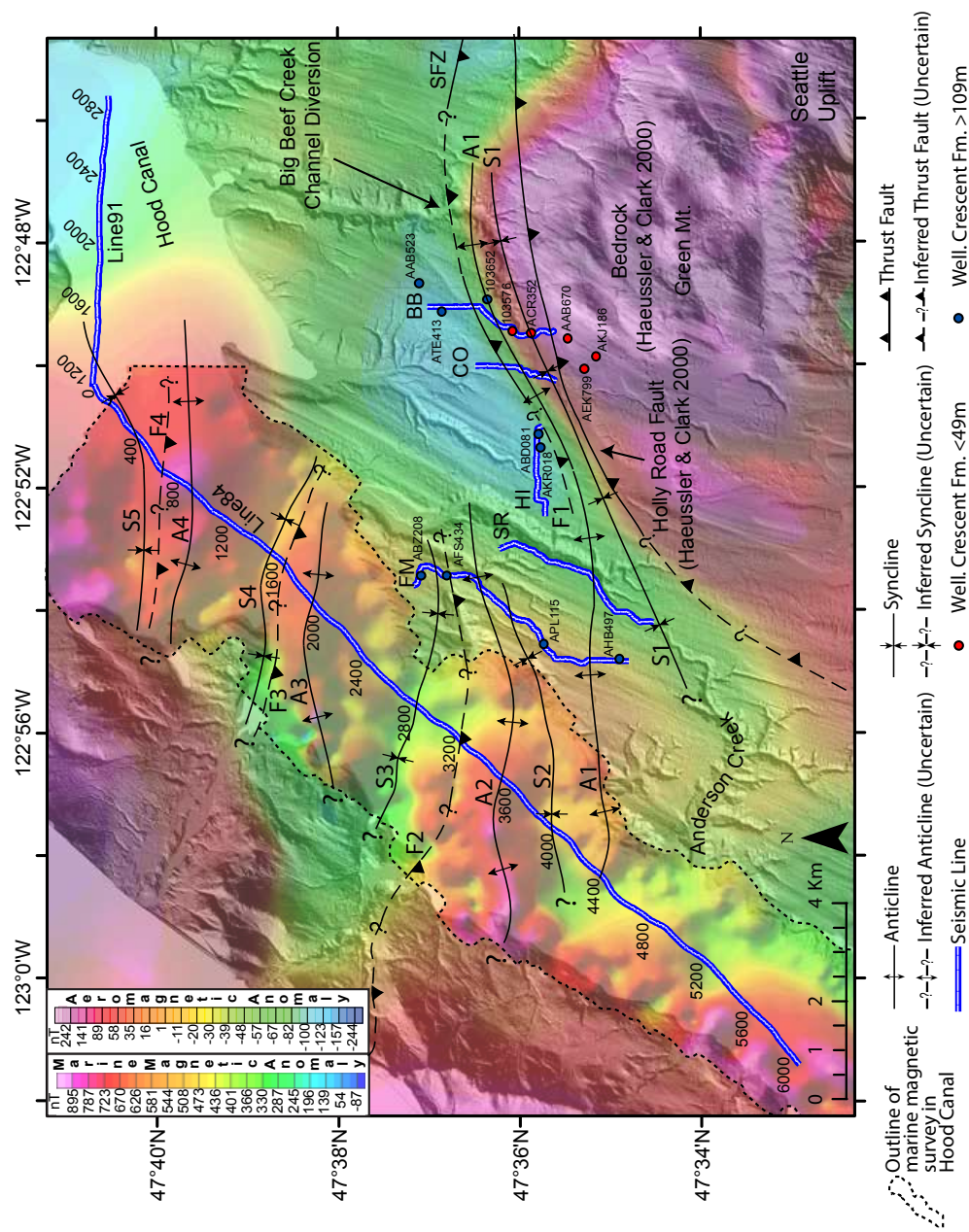


Figure 2.3: Map showing seismic and potential field data interpretations overlaid on both gray hillshaded LiDAR (light detection and ranging) data and transparent color magnetic anomaly data. See Figure 2.1B for figure boundaries. The aeromagnetic anomaly data acquired in Hood Canal has been overlaid with the marine magnetic survey anomaly data and is outlined using a dashed line. The diversions of the Big Beef channel and Anderson creek are also shown. A1, A2, A3, and A4-interpreted anticlines; S1, S2, S3, S4, and S5-interpreted synclines; F1, F2, F3, and F4-interpreted faults; Line84-Hood Canal seismic line; Line91-Hood Canal seismic line; CO-Coho Rd. seismic line; BB-Big Beef Rd. seismic line; FM-Feather-Minnig Rd. seismic line; HI-Hite Rd. seismic line; SR-State Route 101 seismic line; SFZ-Seattle Fault Zone. Numbers adjacent to the Line84 and Line91 seismic profiles are common depth point numbers.

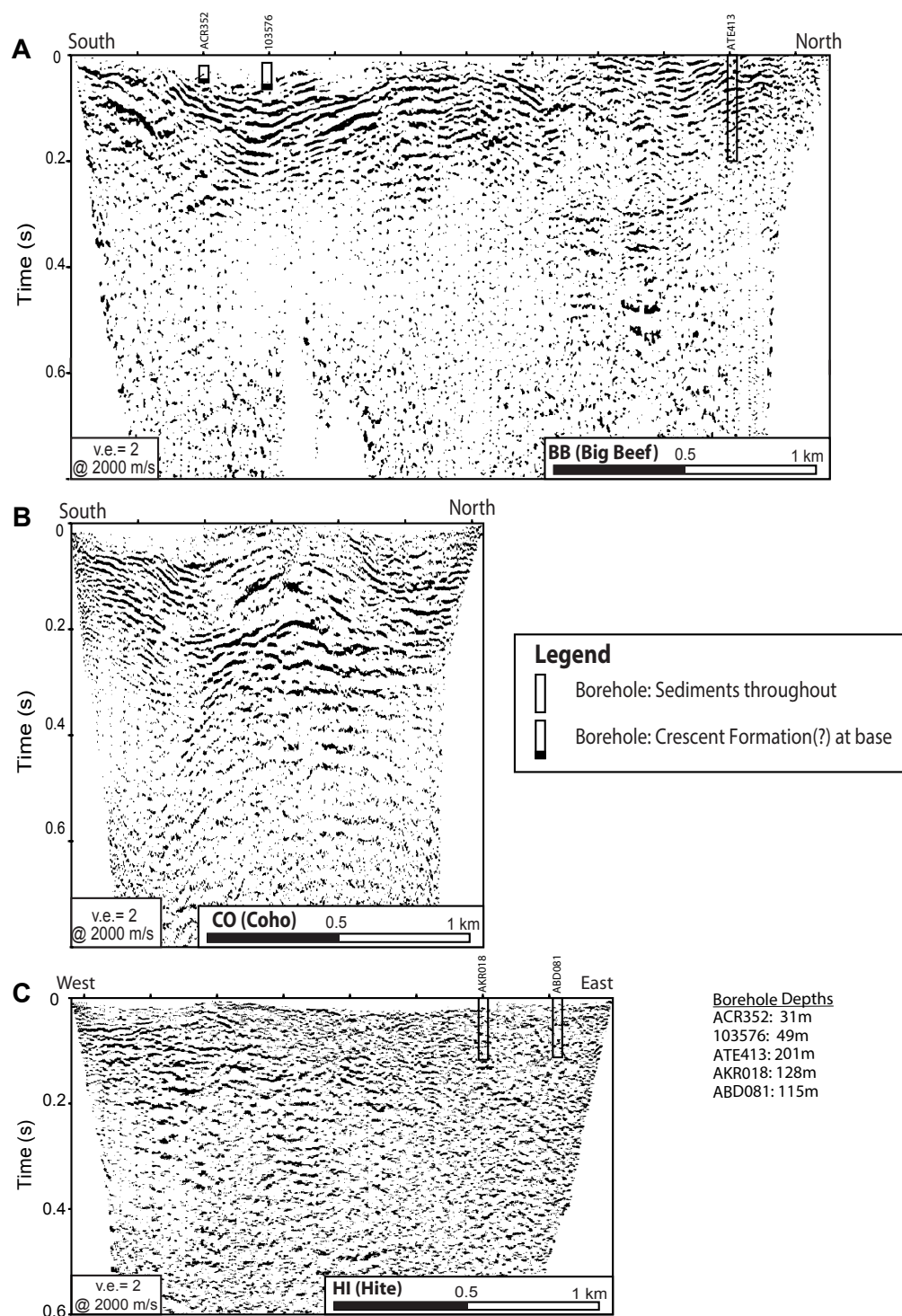


Figure 2.4: (A) Unmigrated and uninterpreted seismic section for the Big Beef Rd. (BB) seismic line including the locations and depths of three water wells used to make our interpretations. Seismic line locations are shown in Figure 2.3. (B) Unmigrated and uninterpreted seismic section for the Coho Rd. (CO) seismic line located approximately 500 m west of the BB seismic line. (C) Unmigrated and uninterpreted seismic section for the HI seismic line including the locations and depths of two water wells used to make our interpretations.

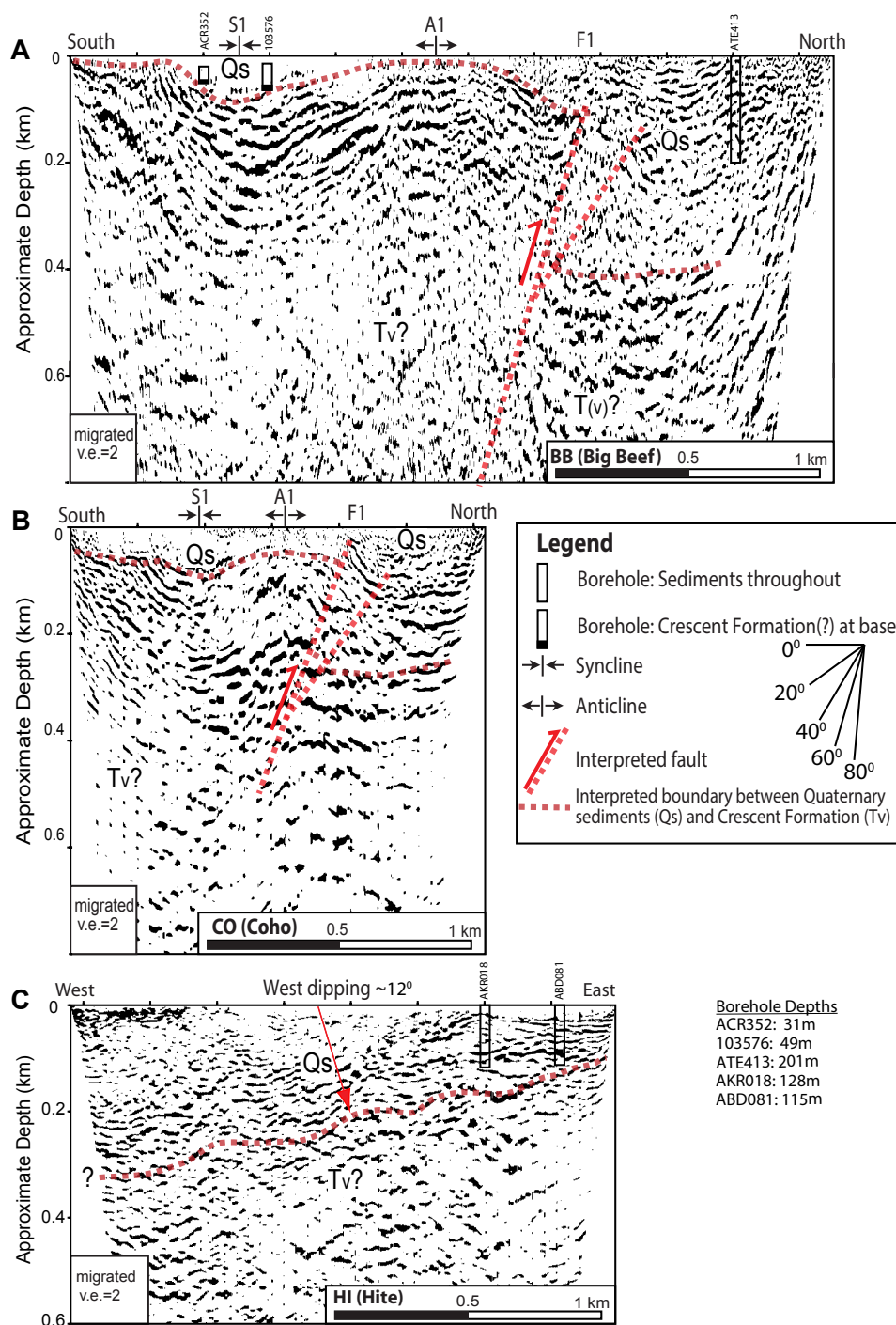


Figure 2.5: (A) Time migrated, time-depth converted, and interpreted seismic section for the Big Beef Rd. (BB) seismic line. Line locations are shown in Figure 2.3. A1-interpreted anticline; S1-interpreted syncline; F1-interpreted south-dipping thrust fault; See legend for additional explanations. (B) Time migrated, time-depth converted, and interpreted seismic section for the Coho Rd. (CO) seismic line. A1-interpreted anticline; S1-interpreted syncline; F1-interpreted south-dipping thrust fault; (C) Time migrated, time-depth converted, and interpreted seismic section for the Hite Rd. (HI) seismic line.

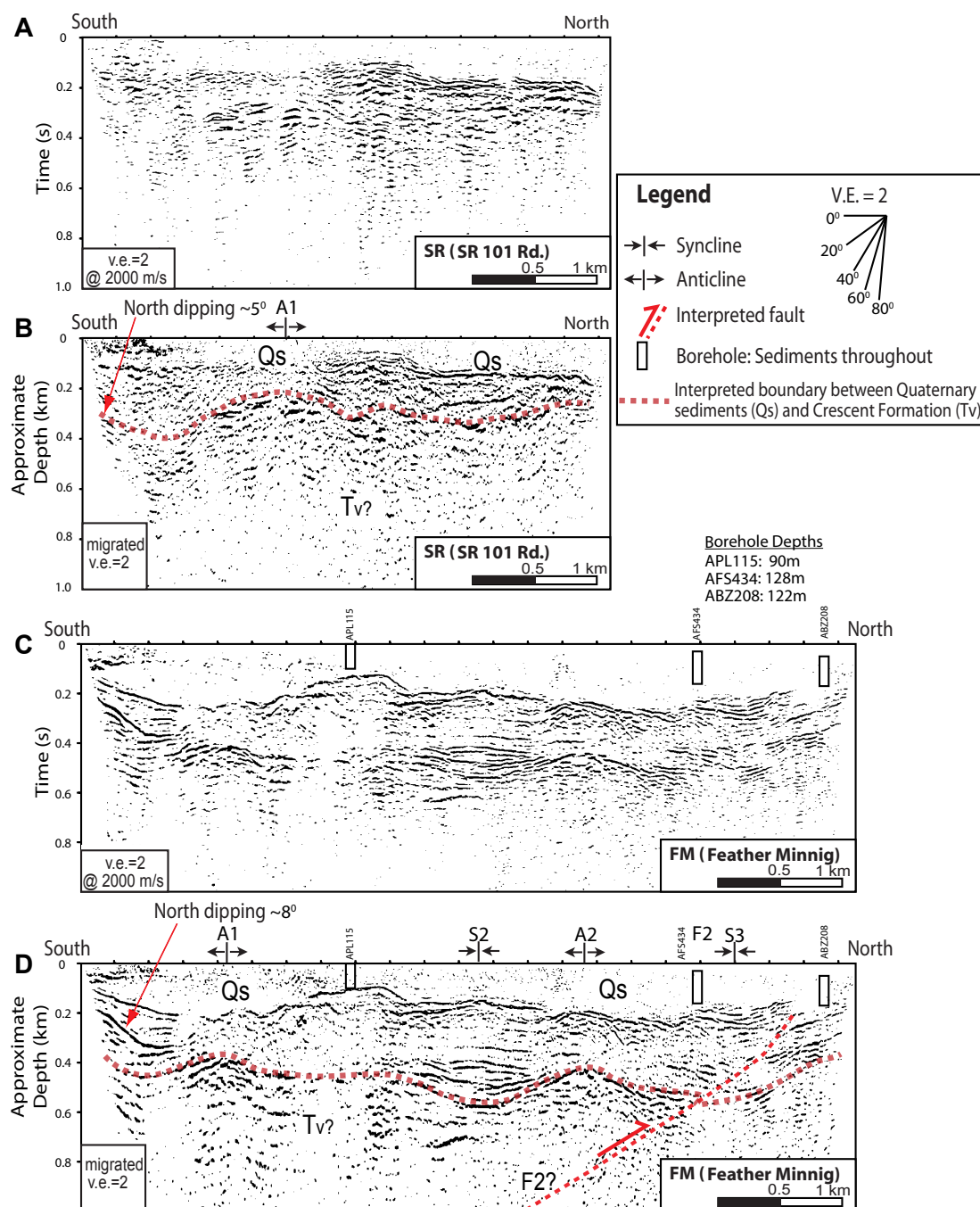


Figure 2.6: (A) Unmigrated and uninterpreted seismic section for the State Route 101 (SR) seismic line. Line locations are shown in Figure 2.3. (B) Time migrated, time-depth converted, and interpreted seismic section for the SR seismic line. A1-interpreted anticline; See legend for additional explanations. (C) Unmigrated and uninterpreted seismic section for the Feather-Minnig Rd. (FM) seismic line. (D) Time migrated, time-depth converted, and interpreted seismic section for the FM seismic line. A1 and A2-interpreted anticlines; S2 and S3-interpreted synclines; F2-interpreted south-dipping thrust fault.

perform the time to depth conversions. The unmigrated data (Figures 2.4, 2.6A, and 2.6C) were used to assist with our interpretations of the migrated data (Figures 2.5, 2.6B, and 2.6D) as there tends to be more signal coherency in the unmigrated data. This greater coherency is likely due to inaccuracies in our near surface velocity model and out-of-plane reflections that can reduce the effectiveness of the migration process (Figures 2.5, 2.6B, and 2.6D).

The aeromagnetic data presented here were acquired by the U.S. Geological Survey, using a nominal altitude of 300 m above ground, but the altitude increased to >1 km over the eastern margin of the Olympic Mountains (Blakely *et al.*, 1999). The north-south flight lines were spaced 400 m apart, with east-west tie lines spaced 8 km apart. We corrected the raw magnetic data for the Earth's background field and then reduced to the pole. Reduction to the pole simplifies data interpretation by recalculating the magnetic intensity data as if it were at the north pole. In Figure 2.2A, we emphasize the magnetic sources in the upper 2 km by upward continuing the reduced to the pole aeromagnetic data by 4 km and then subtracting the result from the original reduced to the pole grid (Jacobsen, 1987). The gravity data were acquired and compiled by U.S. Geological Survey personnel and had been previously reduced to isostatic residual anomaly values. Isostatic residual anomalies have been gridded using minimum curvature, with a 250 m grid cell size.

To supplement the aeromagnetic data in this area, we conducted an additional marine magnetic survey of Hood Canal using a 6-m-long fiberglass fishing boat. The magnetometer was positioned 3 m forward of the bow using 3-m-long wooden boom to reduce the magnetic effects of the boat. At the position of the sensor, the magnetic field of the boat had a maximum directional error of ~ 7 nT, determined by crossing

a single point in the four cardinal directions. The marine data were corrected for this heading error, even though it is small in comparison to anomalies of geologic origin. The survey tie lines and magnetic anomaly results are presented in the left-hand and middle panels of Figure 2.2C, respectively. A comparison of these results with the aeromagnetic anomalies (right-hand panel of Figure 2.2C) demonstrates the additional information provided by the marine magnetic data. To facilitate our analyses, these marine magnetic data are superimposed onto the aeromagnetic anomaly map in Figure 2.3.

We used legacy marine seismic data acquired in Hood Canal (Dadisman *et al.*, 1997; Figure 2.3) to further investigate the hypothesized structural linkage beneath Hood Canal. These seismic data extend much farther to the north and south than our land-based seismic lines, and should intersect any westward projection of the Seattle Fault Zone. The narrow, steep walls of Hood Canal can cause out-of-plane reflection interference in the seismic profiles, but depths to interpreted Crescent Formation basement rocks are estimated along the length of the profile and plotted with the corresponding magnetic anomaly data. Water well log data obtained from the Washington State Department of Ecology (<http://apps.ecy.wa.gov/wellog>) were used to assist with our seismic interpretations. The locations and identification tags of these wells are shown in Figures 2.3, 2.4, 2.5, and 2.6.

2.4.2 Results and interpretations

Two seismic profiles collected on Big Beef (BB) and Coho (CO) roads were acquired on glacial till and outwash deposits immediately north of exposed Crescent Formation rocks at Green Mountain (Haeussler and Clark, 2000; Tabor *et al.*, 2011; Figure 2.3).

The magnetic field decreases in amplitude northward along both profiles (Figure 2.3), suggesting a northward deepening of the Crescent Formation from exposures at Green Mountain. This increasing bedrock depth to the north is supported by well log data that indicate a bedrock depth of ~ 50 m on the southern end of the BB profile but no bedrock above a depth of ~ 200 m on the north end of the BB profile (Figures 2.4A and 2.5A). Additional water well drillers logs near the BB and CO lines are all consistent with the Crescent Formation dipping to the north. We used these well log and magnetic data along with geologic mapping (Haeussler and Clark, 2000) to interpret the Quaternary-Tertiary boundary on the BB and CO seismic lines. A diverted stream channel (Big Beef Creek), apparent on the LiDAR topographic image, overlies a syncline (label S1, Figure 2.3) evident on seismic profiles BB and CO (Figure 2.5) and may be structurally controlled, offering evidence for synclinal growth that may be related to active faulting. The southwestern extension of syncline S1 underlies a second diverted stream channel (Anderson Creek) also visible on the LiDAR data.

The BB and CO profiles show the north-dipping bedrock surface north of Green Mountain, and exhibit north-dipping structures in the upper 0.5 km (Figures 2.5A and 2.5B). These structures include syncline S1 and anticline A1. The distance between S1 and A1 decreases at the CO profile and then increases again farther to the west (Figure 2.3). Both of these structures become more southerly in trend as they wrap around the northwest flank of Green Mountain following the northern margin of the pronounced magnetic high centered over Green Mountain (Figure 2.3). Structures S1 and A1 likely reflect either glacial processes (moraines) or late Quaternary tectonic deformation. We favor the latter interpretation because the BB and CO seismic profiles also exhibit reflector truncations and changes in Quaternary reflector dip

that we interpret as marking a southwest-striking reverse fault F1 with south-side-up Quaternary displacement of >200 m. We show F1 on the BB and CO seismic profiles with a splay (Figures 2.5A and 2.5B) due to the packet of steeply north dipping reflections above 0.1 km depth that are not present in the hanging wall. The truncation on these shallow reflections may be due to out-of-plane reflections or dextral strike-slip motion causing an along strike offset. The fault is striking to the southwest and may, through increasing strike-slip motion, accommodate an element of north-south shortening. This northeast-southwest aligned dextral strike-slip motion is also supported by a recent study to the east that shows evidence for similarly aligned faults beneath the central Puget Lowland (Mace and Keranen, 2012). Fault F1 parallels the north edge of anticline A1 (Figure 2.3), suggesting that the anticline is a fold above the fault. The fault may be one of several thrust faults similar to those imaged on seismic profiles within the Seattle Fault Zone beneath and east of Puget Sound (Johnson *et al.*, 1999; Haeussler and Clark, 2000; Liberty and Pratt, 2008). We interpret these faults and folds to be related to the Seattle Fault Zone that defines the southern margin of the Seattle basin. The folding along BB and CO may be related to the Seattle monocline as interpreted by Haeussler and Clark (2000) or to backthrusts of a Seattle Fault that projects farther to the north. We cannot distinguish between these two interpretations because of the short profile lengths. Regardless, the southwest-striking faults and folds showing late Quaternary motion demonstrate that the strain accommodated by the Seattle Fault Zone may extend farther west than the western limits of the Seattle basin and is instead characterized by a broadening zone of deformation that becomes increasingly distributed as it crosses Hood Canal and links with the Saddle Mountain deformation zone.

The seismic profiles along Hite Rd. (HI), State Route 101 (SR), Feather-Minnig Rd. (FM), and Hood Canal were acquired west of the BB and CO seismic profiles outside the limits of the Seattle basin as defined by gravity anomalies (Figure 2.2B; Finn, 1990) and seismic tomography (Snelson *et al.*, 2007) but along strike of the Seattle Fault Zone (Figure 2.3). These profiles exhibit less deformation than the BB and CO profiles to the east (Figures 2.5 and 2.6) and appear west of the Green Mountain magnetic high (Figure 2.3). Although data quality along the HI profile is poor, the profile shows predominately west-dipping reflectors that we interpret as Quaternary strata overlying Tertiary Crescent Formation (Figure 2.5C). There are no direct constraints to help interpret the Quaternary / Tertiary boundary on the HI profile; however, we can use the strength of the magnetic anomalies as a proxy for the depth to Crescent Formation, assuming the magnetization of Crescent Formation basalts remain approximately uniform. Our interpretation for the top of Crescent Formation therefore relies on correlating bedrock exposures and well logs to the amplitudes of the corresponding magnetic anomalies, and applying this relationship to our seismic interpretations. Through this exercise we interpret the Quaternary / Tertiary boundary along the HI profile to be at depths of 0.2 to 0.6 km, which is compatible with well logs that do not show Tertiary strata but show Quaternary sediments at depths as great as ~ 130 m. We interpret the west dipping strata to encompass the north limb of the A1 anticline.

Our interpretations for the Quaternary / Tertiary boundary along the SR, FM, and Hood Canal seismic profiles were obtained by a similar method as described above. Projecting the broad north limb of anticline A1 westward from the HI profile, we interpret anticline A1 along the southern portions of SR and FM seismic pro-

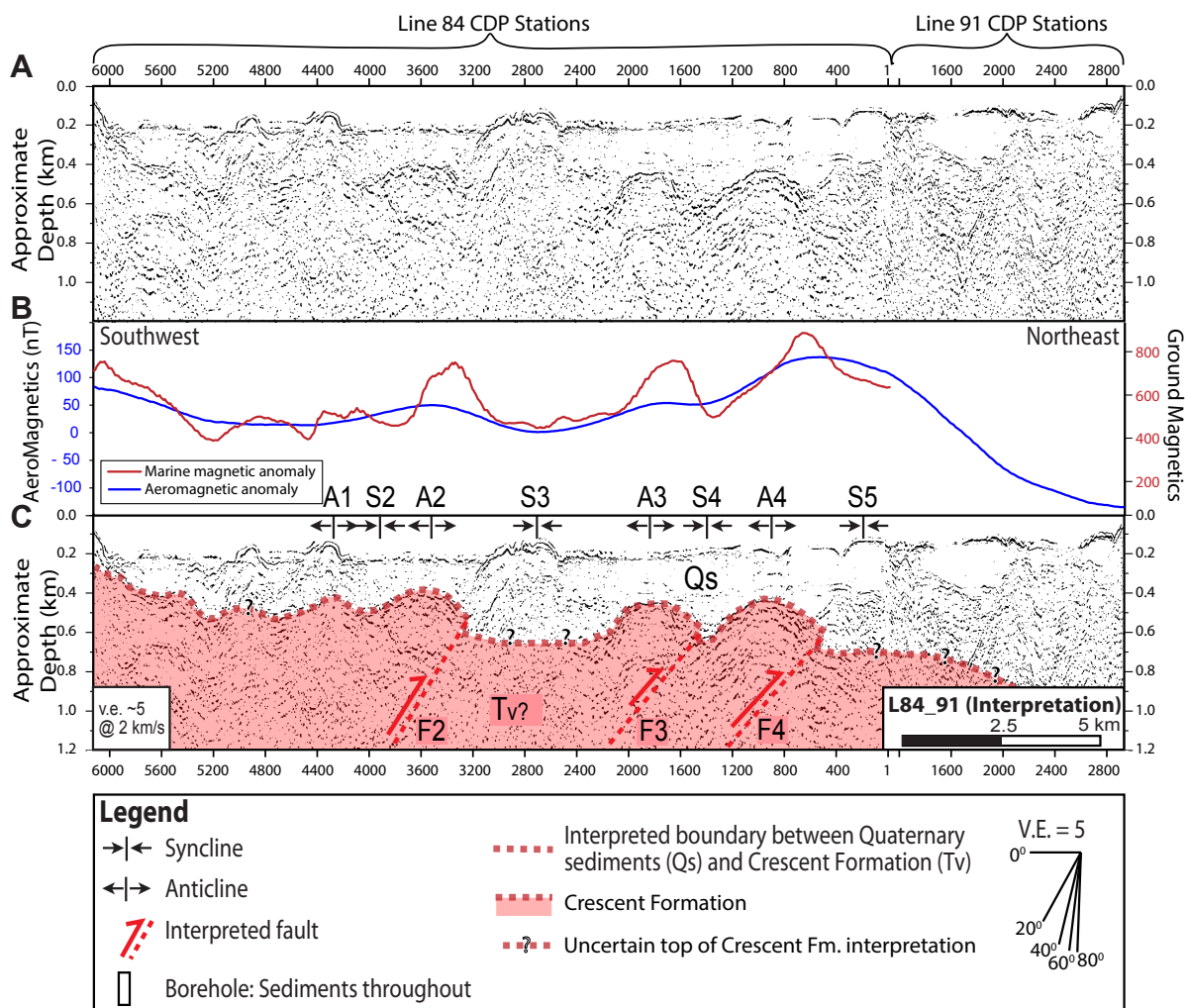


Figure 2.7: (A) Time migrated, time-depth converted, and uninterpreted seismic section for the Hood Canal seismic lines 84 and 91 shown in Figure 2.3. (B) Reduced to the pole aeromagnetic (blue) and marine/ground magnetic (red) anomaly values that correspond with the location of the Hood Canal seismic lines 84 and 91. (C) Time migrated, time-depth converted, and interpreted seismic section for the Hood Canal seismic lines 84 and 91. A1, A2, A3, and A4-interpreted anticlines; S2, S3, S4, and S5-interpreted synclines; F2, F3, and F4-interpreted faults. See legend for additional explanations.

files (Figure 2.3) at a depth of ~ 0.35 km (Figure 2.6) and along the Hood Canal seismic profile at a depth of ~ 0.4 km (CDP 4400 in Figure 2.7C). We interpret a more prominent anticline termed A2, at a depth of ~ 0.4 km along the FM profile that is north of the A1 structure and north of the SR profile limits. We infer a west trend for the more prominent anticline A2 from the Hood Canal seismic interpretation and magnetic data (Figures 2.7B and 2.7C). The east-west synclines S2 and S3 imaged beneath Hood Canal are also observed on the FM seismic profile. The Hood Canal seismic section shows additional faults and folds to the north (A3, A4, A5, S3, S4, S5, F1, F2, and F3) that produce west-east lineations on the magnetic data (Figures 2.3 and 2.7C). It is important to note that each interpreted anticline and syncline correlates with a magnetic high or low, respectively, seen in high-resolution marine magnetic data from Hood Canal (Figure 2.3).

From the Hood Canal and FM seismic profiles, we interpret a series of east-west striking, low angle thrust faults (F2, F3 and F4) that may indicate strain partitioning in the Seattle Fault Zone across a number of faults beneath Hood Canal. Faults F2 and F4 lie along strike of faults previously interpreted by Blakely *et al.* (2009) as possible links between the Seattle Fault Zone and Saddle Mountain deformation zone. The seismic profiles show no clear indication of offset strata above the Tertiary bedrock surface and is complicated by out-of-plane reflections from the Hood Canal boundaries. This lack of evidence for younger offset strata suggests that these low-angle thrust faults may be older, inactive faults, or that northward shortening is distributed along a series of faults that show little late Quaternary displacement. The data quality along the Hood Canal Line 91 seismic section does not enable us to confidently determine the source of the corresponding eastward decrease in the

aeromagnetic and gravity values (Figures 2.7 and 2.2B) and whether there is related faulting. These data do suggest that these potential field gradients represent the northern limb of the Seattle Fault Zone and delineate the margins of the 7-9 km deep Seattle basin.

We interpret $\sim 5^{\circ}$ - 8° north-dipping Quaternary strata along the southern portions of the SR and FM profiles south of anticline A1 to indicate that Quaternary deformation continues to the west of Green Mountain and farther south than the westward projection of the Seattle Fault (Figures 2.3, 2.6B, and 2.6D). The west to southwest trend of these imaged structures also suggests that the prominent, collinear, southwest-striking magnetic lineation that wraps around Green Mountain may be an expression of the southern limits of the Seattle Fault Zone. Unfortunately, we have no seismic data that extend through the southwestern strike of this magnetic lineation, so we must rely on the potential-field data to examine this link.

Structural folding and faulting that follow the trend of Green Mountain bedrock exposures, along with our seismic interpretations of inactive or smaller displacements on structures further to the west, suggest three possible scenarios for the active Seattle Fault Zone: (1) termination east of the FM and SR profiles, (2) change in trend to wrap around the bedrock exposures and pass south of the FM and SR profiles, or (3) distribution over a broad zone west of Green Mountain that we term a strain transfer zone. The strain transfer zone scenario best matches our observations of the staggered faults and folds spanning between the Seattle Fault Zone and Saddle Mountain deformation zone. The strain transfer zone is bounded to the north by the Seattle basin, to the east by the Seattle Uplift, and to the west by the Olympic Massif. Our interpretations offer further support for a link between the Seattle Fault

Zone and Saddle Mountain deformation zone. We cannot determine if this link is between active faults, but the synchronicity of large earthquakes on both the Seattle Fault Zone and Saddle Mountain deformation zone 1,100 years ago suggests that this is a possibility.

2.5 Western extent of Tacoma Fault

The Tacoma Fault dips northward beneath the Seattle Uplift and deforms strata of late Quaternary age (Figure 2.1; Brocher *et al.*, 2001; Johnson *et al.*, 2004; Clement *et al.*, 2010). The Crescent Formation in the hanging wall of the Tacoma fault has been uplifted from $\sim 5\text{-}7$ km depth beneath the Tacoma basin to ~ 213 m depth in a borehole on the Seattle Uplift (Sceva, 1957; Brocher and Ruebel, 1998). The Catfish Lake scarp imaged on LiDAR data provides evidence for Holocene deformation in the center of a seismically imaged kink band along the Tacoma Fault (Johnson *et al.*, 2004; Sherrod *et al.*, 2004; Liberty and Pratt, 2008; Clement *et al.*, 2010). The Tacoma Fault appears as a prominent west-trending magnetic lineation on the southern margin of the Seattle Uplift, but deformation associated with the Tacoma Fault has not been identified west of Hood Canal or east of Puget Sound. Johnson *et al.* (2004) interpret the Tacoma Fault as a $\sim 40^\circ$ north-dipping backthrust of the Seattle Fault Zone based on their analysis of seismic reflection data.

A gravity low and slow upper crustal seismic velocities define a basin immediately west of the Seattle Uplift that has previously been termed the Dewatto basin (Figure 2.2; van Wagoner *et al.* (2002); Johnson *et al.* (2004)). Along the east edge of this basin and west edge of the Seattle Uplift is a north-striking magnetic and gravity anomaly that we term the Dewatto lineament (DL in Figure 2.2A and 2.2B;

Pratt *et al.*, 1997; Brocher *et al.*, 2001; van Wagoner *et al.*, 2002). The southern end of the Dewatto lineament at the southwestern corner of the Seattle Uplift intersects the west-trending Tacoma Fault. It has been previously suggested that the Tacoma Fault extends beneath Hood Canal to just east of the Frigid Creek fault (label FCF, Figure 2.2) based on the presence of a broad, low-amplitude (~ 200 nT and 10-20 km wide), west-trending magnetic anomaly (Johnson *et al.*, 2004) that is along strike with the Tacoma Fault. However, the magnetic anomaly west of the Dewatto lineament is extremely weak compared to the Tacoma and Dewatto lineaments, and neither gravity nor seismic tomography data (Brocher *et al.*, 2001) are consistent with uplifted basement rocks along this anomaly. This weak magnetic anomaly is similar in amplitude to other anomalies throughout the Puget Lowland and may be caused by near-surface deformation resulting from glacial deposition or scour (e.g., Sherrod *et al.*, 2008). Gravity, magnetic, and tomography data do not support a separation between the Tacoma and Dewatto basins.

We propose that the Dewatto basin is a northwestern arm of the Tacoma basin. Furthermore, we suggest that the Tacoma and Dewatto basins have evolved as a single structure, and refer to both as the Tacoma basin. The kidney-shaped Tacoma basin thus defined is bounded by the Olympia Fault to the south, the Saddle Mountain deformation zone to the west, and the Seattle Uplift to the north (Figures 2.2A and 2.2B).

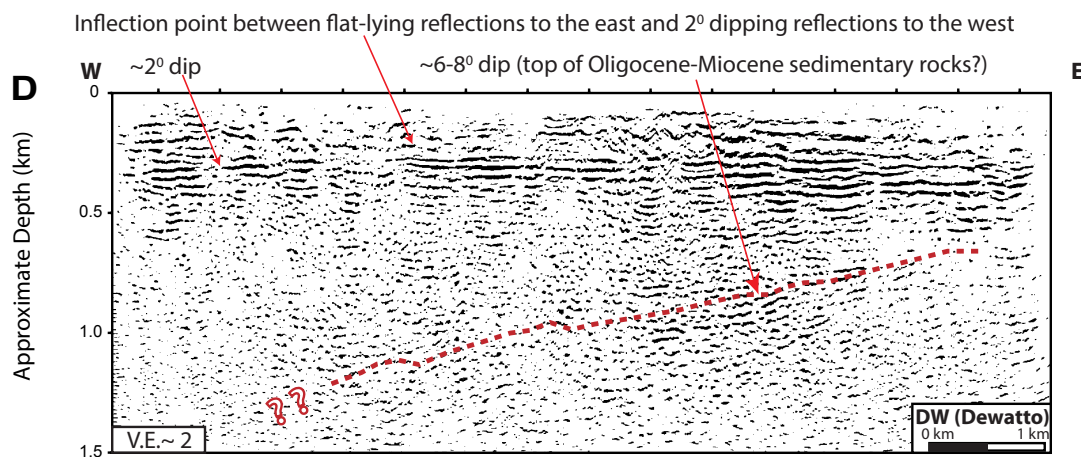
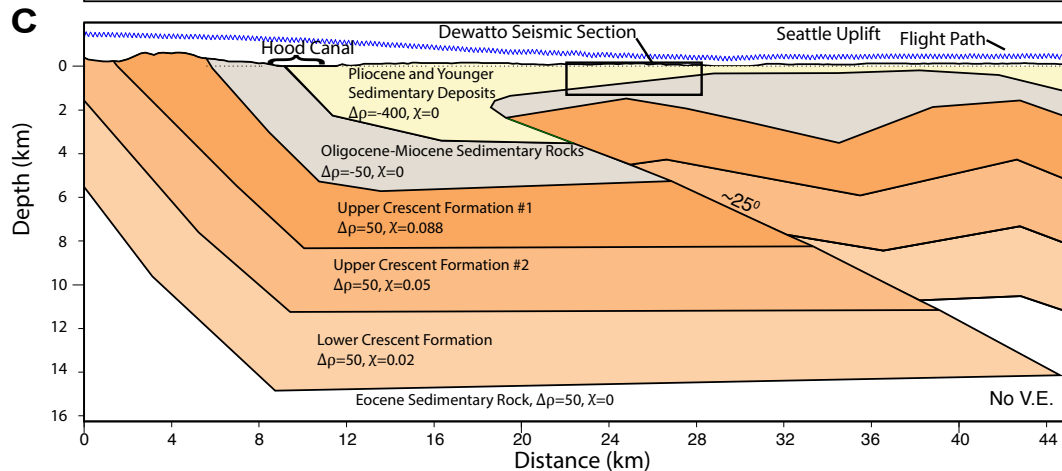
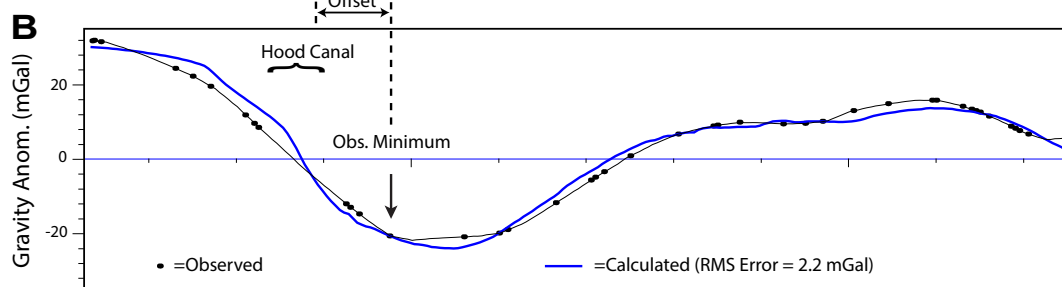
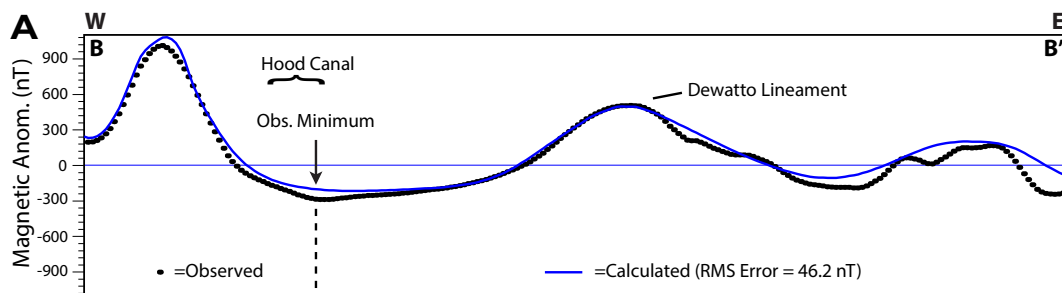


Figure 2.8: (A) and (B) The calculated and observed anomalies using forward modeling for the 45 km long Dewatto transect B-B' shown in Figure 2.2A. The model extends to infinity in both directions perpendicular to the profile. (C) The magnetic and density distributions used to interpret the geological structure from the forward model where $\Delta\rho$ is the density contrast in kg/m³ relative to normal crust (2670 kg/m³) and χ is the magnetic susceptibility in SI units. The modeled thrust fault is termed the Dewatto Fault. (D) Seismic section for the 7.5-km-long Dewatto profile (DW) shown in Figures 2.2A and 2.2B that runs E-W across the western margin of the Seattle Uplift (SU). This cross section shows $\sim 20^\circ$ west-dipping tilt in the interpreted Pliocene and younger sedimentary deposits and the more severe $\sim 6^\circ$ - 80° tilting of west-dipping Oligocene-Miocene sedimentary rocks below 0.6 km.

We acquired a 7.5-km-long west-east seismic profile southwest of Green Mountain to image strata across the Dewatto lineament (Figures 2.2A, 2.2B, and 2.8D; line DW). Relatively flat-lying reflectors suggest undeformed strata in the upper 0.5 km depth along the eastern portion of the profile and gently dipping ($\sim 2^\circ$) strata along the western 2 km of the Dewatto profile (Figure 2.8D). We interpret an apparent reflector divergence as an unconformity marking the boundary between deposits of late Quaternary age or younger and $\sim 6^\circ$ - 8° west-dipping Tertiary strata on the eastern and middle portions of the profile. There is no clear evidence of stratigraphic offset along this profile, but the reflector dip is consistent with late Quaternary folding of hanging wall strata similar to that observed across the east-striking Tacoma Fault to the southeast (Johnson *et al.*, 2004).

2.5.1 Geophysical investigations

To constrain deformation along the western margin of the Seattle Uplift, we forward modeled gravity and magnetic data using constraints from previous potential-field modeling to the west (Blakely *et al.*, 2009), deep well logs (Brocher and Ruebel,

1998), seismic tomography velocity models (Brocher *et al.*, 2001), and stratigraphic constraints for the top kilometer from the seismic data presented in Figure 2.8D. The model is along a 45-km-long west-east transect crossing the Dewatto lineament positioned where the magnetic and gravity gradients are well defined (B-B' in Figure 2.2). Magnetic and density values used in the model are consistent with physical property measurements from Blakely *et al.* (2009) along a northwest-southeast transect that crosses the Saddle Mountain Fault and the Tacoma basin (Figure 2.2A, profile A-A'). Densities for the primary formations were taken from regional well logs (Brocher and Ruebel, 1998) and are modeled as density contrasts relative to normal crust (2670 kg/m³).

Our model (Figure 2.8C) based on gravity and magnetic profiles B-B' suggest asymmetry in the shape of the northwestern arm of Tacoma basin and ~5 km of Tertiary and younger sedimentary strata overlying rocks of the Crescent Formation. Steeply dipping Tertiary rocks near Saddle Mountain west of Hood Canal are consistent with previous potential field interpretations (Blakely *et al.*, 2009), and basin depths are in agreement with previous estimates from seismic tomographic studies (Brocher *et al.*, 2001; van Wagoner *et al.*, 2002). The magnetic low that defines the northwestern arm of the Tacoma basin lies ~4 km west of the gravity low. Due to the offset in gravity and magnetic lows (Figures 2.8A and 2.8B), the Dewatto lineament is best modeled as dense magnetic Crescent Formation rocks thrust westward over less dense, non-magnetic basin sediments and sedimentary rocks. Thus, we show the Dewatto lineament modeled with a 25° east-dipping thrust fault (the Dewatto Fault) similar in nature to the north dipping Tacoma Fault (Brocher *et al.*, 2004; Johnson *et al.*, 2004). Our model is consistent with east-west compression and with thrusting

along the eastern boundary of the Olympic Massif (Hurricane Ridge Fault) to the west of the basin. Tilted strata of late Quaternary age observed in the western portions of the Dewatto seismic line (Figure 2.8D) suggest continued folding of strata in the forelimb of the Dewatto Fault.

2.6 Discussion

The decreased deformation and faulting along the SR, FM, and Hood Canal seismic profiles relative to profiles BB and CO farther east (Figures 2.3, 2.6, and 2.7C) indicate that either the active Seattle Fault Zone diminishes to the west of Green Mountain or that deformation is being radially distributed across Hood Canal to the Saddle Mountain deformation zone. Deformation of Quaternary strata on seismic profiles BB and CO (Figures 2.3, 2.5A, and 2.5B) on the north flank of Green Mountain suggests that deformation related to the Seattle Fault Zone extends southwestward from north of Green Mountain (Figure 2.9). Continued westward deformation is supported by north-dipping strata along the southern ends of profiles SR and FM. Furthermore, folded glacial sediments and faults within Green Mountain bedrock (Haeussler and Clark, 2000; Tabor *et al.*, 2011) lie parallel to a magnetic lineation that wraps around Green Mountain bedrock exposures. This southwestward trend of the Seattle Fault Zone may be influenced by the adjacent Olympic Massif and may mark the southern limits of a zone of deformation that transfers strain between the Seattle Fault Zone and Saddle Mountain deformation zone.

The magnetic lineation that corresponds with fault F2 was originally interpreted as a fault by Blakely *et al.* (2009) using a maximum horizontal gradient method (Phillips *et al.*, 2007). The structures A2, F2, and S3 responsible for this lineation,

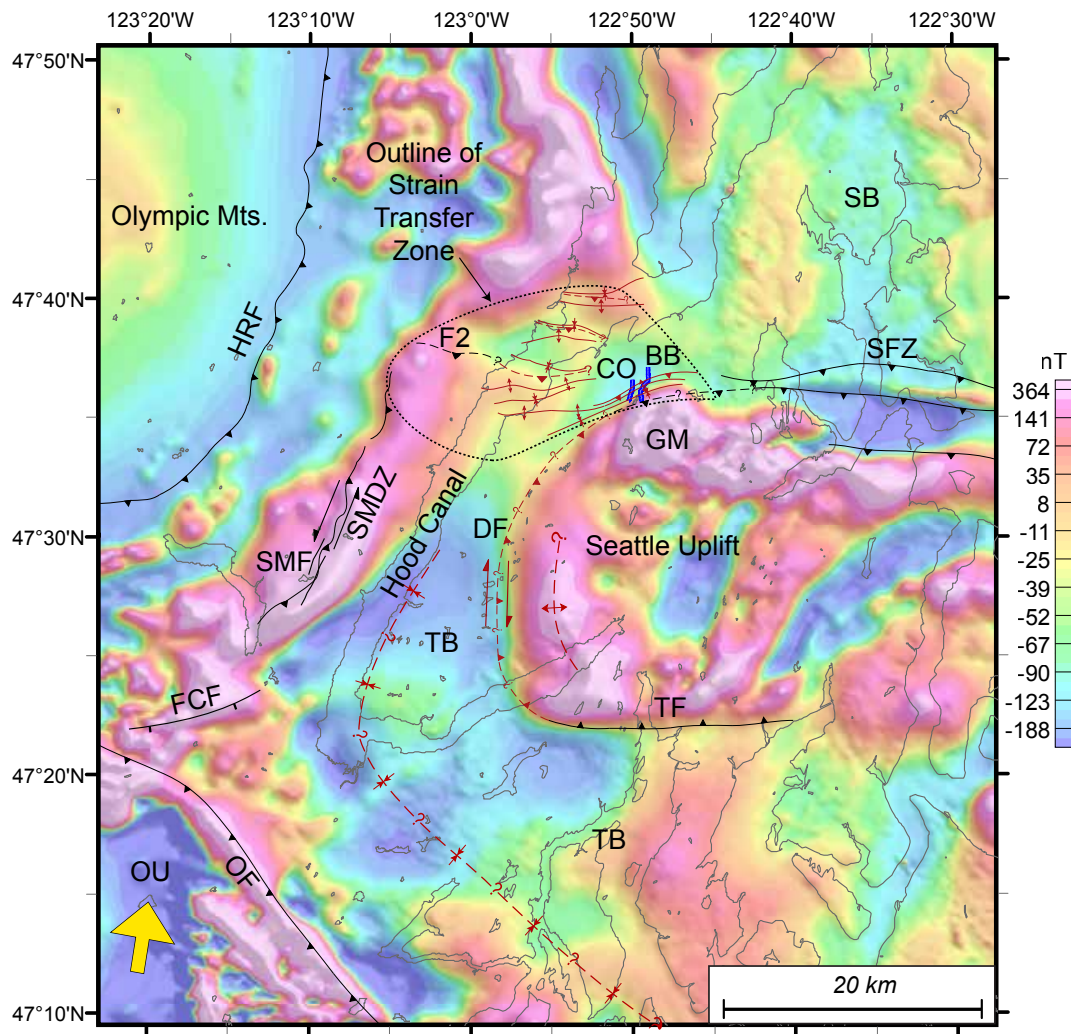


Figure 2.9: Summary interpretation of the western portions of Seattle Fault zone. Rainbow colors indicate reduced-to-the-pole magnetic anomaly field intensity. The yellow arrow shows the regional direction of strain relative to North America (Mazzotti *et al.*, 2002; McCaffrey *et al.*, 2007). Solid black lines show previously mapped faults while structures introduced in this paper are marked in red. The two blue lines represent the location of the Coho Rd. (CO) and Big Beef Rd. (BB) seismic lines; DF-Dewatto Fault; F2-Thrust fault (Figures 2.3, 2.6, and 2.7); FCF-Frigid Creek Fault; GM-Green Mountain; HRF-Hurricane Ridge Fault; OF-Olympia Fault; OU-Olympia uplift; SB-Seattle basin; SFZ-Seattle Fault Zone; SMDZ-Saddle Mountain deformation zone as interpreted from magnetic data (Blakely *et al.*, 2009); SMF-Saddle Mountain fault (East and West); TB-Tacoma basin; TF-Tacoma Fault.

are more clearly expressed by our marine magnetic survey (Figure 2.2C), and their presence is evident in the Hood Canal seismic data (Figure 2.7C). We have no seismic data south of Line 84 (Figure 2.3) to determine the southern limit of the fold and fault belt; however, the seismic data presented in Figure 2.7C, along with the absence of strong east-west magnetic lineations south of anticline A1, suggest that the relatively large displacement on west-striking structures lying between A1 and the eastern end of seismic line 91, all form a distributed area of deformation related to the Seattle Fault Zone projecting westward through a radially distributed strain transfer zone. The zone of strain transfer may continue southward, but we believe on the basis of the Hood Canal magnetic survey, that strain is concentrated between the Seattle basin margin to the north and anticline A1 to the south. The broad potential field gradients associated with these lineations suggest that the sources either lie deeper than the FM and SR profile imaging depths, that the gentle gradients are the result of the high altitude used for the aeromagnetic data acquisition, or that contrasts are gradational rather than abrupt. Based on the available data, late Quaternary deformation likely continues southwest around Green Mountain, where gravity and magnetic highs are likely caused by structures that connect the Seattle Uplift with the Olympic Massif to the west. Late Quaternary deformation also continues to the west, but is distributed over a larger area causing smaller displacements on active transfer faults that are difficult to image using seismic and magnetic methods. In addition, the dip-slip component observed on the transfer faults further to the east (e.g., as observed on the BB and CO seismic lines) may partly transition to an increasing strike-slip component as they strike westward. Such deformation would be less evident in seismic and magnetic imaging.

Seismic tomography, gravity, magnetic, and geologic data suggest that the Tacoma basin is a $\sim 5\text{-}7$ km deep, kidney-shaped basin bounded by the Tacoma, Saddle Mountain, and Olympia Fault Zones (Figure 2.9; Brocher *et al.*, 2001; van Wagoner *et al.*, 2002; Blakely *et al.*, 2009). The low-amplitude, ~ 200 nT magnetic anomaly crossing Hood Canal along strike with the Tacoma Fault may mark a minor component of deformation related to the Tacoma Fault. However, we propose that the Tacoma Fault terminates at the southern end of the Dewatto lineament, where it links with a north-south fault, here termed the Dewatto fault, that strikes along the Dewatto lineament. We model the Dewatto fault as a low-angle thrust fault separating the Tacoma basin from the Seattle Uplift to the east (Figures 2.8 and 2.9). The low angle Dewatto Fault thrust model may be best explained by east-directed shortening caused by exhumation of the accretionary terrane in the Olympic core complex (Wells *et al.*, 1984; Johnson, 1985; Brocher *et al.*, 2001). However, given modern north-northeast-directed motion inferred from GPS measurements and earthquake focal mechanisms (Mazzotti *et al.*, 2002; McCaffrey *et al.*, 2007), and clockwise rotation of the Cascadia Forearc at $1.5 \pm 0.50^\circ/\text{m.y.}$ (Wells *et al.*, 1998), the Dewatto Fault now may be accommodating predominantly dextral strike-slip motion. Assuming that formation of the Seattle Uplift commenced ~ 14 Ma (ten Brink *et al.*, 2002), this low angle thrust fault, which previously accommodated east-west shortening, may now be accommodating predominantly north-south compression by facilitating slip partitioning between the Seattle Uplift and the Olympic Massif. The northward compression that would result from dextral strike-slip motion along the Dewatto Fault may be a component of the strain transfer zone west of Green Mountain.

Recent work by Mace and Keranen (2012), who jointly interpreted several types

of geophysical data in the central Puget Lowland, found evidence for a zone of recent northeast-southwest faulting that crosses the Seattle Basin and Seattle Uplift. By examining offsets of east-west aligned structures in the Seattle Fault Zone, they interpreted dextral strike-slip along this northeast-southwest aligned fault system and suggested that these northeast trending structures may accommodate eastward transport of the Olympic Massif. They further proposed that strain partitioning cycles between the east-west orientated Seattle Fault Zone and these northeast-southwest orientated structures, to facilitate north-south and east-west shortening, respectively. Our data and interpretations of east-west to northeast-southwest to north-south trending structures at the western margins of the Seattle Fault Zone and Seattle Uplift, independently support partitioning of strain between the Seattle Fault Zone and Saddle Mountain deformation zone.

Figure 2.9 illustrates the map expression of a conceptual model for the west to southwestward continuation of deformation related to the Seattle Fault Zone. Seismic reflection data and magnetic anomalies presented here indicate that the deformation observed along the southern boundary of the modern Seattle Fault Zone extends west and southwestward from north of Green Mountain (Figures 2.3, 2.5, 2.6, and 2.7). We propose that strain between the western part of the Seattle Fault Zone and the Olympic Massif is transferred by way of a broad, west to southwest-striking zone of deformation reflected in the gravity and magnetic highs that traverse Hood Canal along the northern limits of the Tacoma basin (Figures 2.2B and 2.9). We believe this is a strain transfer zone that links the Saddle Mountain and Seattle Fault zones through a series of smaller displacement faults and folds as partially observed in our data (Figure 2.9). The strain transfer zone merges with the Saddle

Mountain deformation zone and defines the northern boundary of the Tacoma basin. This model requires that faults and folds mapped on profiles BB and CO are in the hanging wall of the Seattle Fault Zone and that the faults project to the surface farther north. We suggest that the southwest structural trend observed on the BB and CO seismic profiles defines the southern margin of the strain transfer zone. The northern margin of this strain transfer zone is characterized by the east-west aligned structures interpreted from our seismic and magnetic data near Hood Canal (Figures 2.6 and 2.7).

The fault-controlled western boundary of the Seattle Uplift suggests strain partitioning along the western limits of the Seattle Fault Zone in order to accommodate rigid block uplift of the Seattle Uplift and Saddle Mountain deformation zone. This may represent a complex interplay with east-directed Olympic subduction and north-directed (modern) Cascadia motion as observed on the Hurricane Ridge Fault (Tabor and Cady, 1978b; Wells *et al.*, 1984; Johnson, 1985; Brandon *et al.*, 1998). Our model suggests a direct link between the Seattle Fault and Saddle Mountain deformation zones. This model is consistent with studies of the Saddle Mountain West and Saddle Mountain East Faults, which show that these faults were formed by east-west compression that caused thrust faulting and displacement of Pleistocene glacial deposits and underlying Eocene Crescent Formation rocks (Wilson, 1975; Wilson *et al.*, 1979; Witter *et al.*, 2008; Blakely *et al.*, 2009). Trench excavations across the Saddle Mountain Faults also show that both are southeast dipping thrust faults with left-lateral movement. There is further paleoseismic evidence that both of these faults produced earthquakes between 1,000 and 1,300 yr ago (Hughes, 2005). The possible synchronicity of motion on these faults with the >M7 earthquake that occurred on the

Seattle Fault $\sim 1,100$ yr ago is consistent with rupture of linked faults. These results suggest that the Seattle Fault Zone extends >100 km and is capable of supporting $>M7$ earthquakes (Wells and Coppersmith, 1994). Our interpretation of the Dewatto fault along the western margin of the Seattle Uplift has implications for conventional risk assessments in the region, however until a slip rate and recurrence interval is established, its risk is unknown.

The principal uncertainties in our model are related to the sparseness of our data and the inherent non-uniqueness of potential field interpretations. We have minimized these uncertainties by using an integrated approach that incorporates a range of geophysical and geological data. We have investigated a number of possible scenarios that honor these data and that a distributed zone of strain transfer across Hood Canal provides a robust fit to our data and offers an explanation for interaction between the western Seattle Fault Zone and Olympic Massif. Our interpretation could be improved and tested with additional gravity and seismic data both east-west across the Dewatto lineament and north-south along Hood Canal. A three-dimensional, balanced crustal model would assure that interpreted structures can be restored back in time to balanced stratigraphy.

2.7 Conclusions

Our analyses suggest that the Seattle Fault Zone and Saddle Mountain deformation zone are linked along the northern margin of the Tacoma basin west of the Seattle Uplift, and that the basin's eastern margin is controlled by the Dewatto Fault where it is expressed as the Dewatto lineament. Late Quaternary deformation interpreted on our BB and CO seismic profiles implies that the Seattle Fault Zone continues to the

west of the Seattle basin and may merge with the Saddle Mountain deformation zone through a broad strain transfer zone. Potential-field lineaments and west-dipping late-Pleistocene strata near the Dewatto lineament suggest that the Seattle Uplift acts as a rigid block, juxtaposing Crescent Formation rocks to the east against the northwestern arm of the \sim 5-7 km-deep Tacoma basin (previously defined as the Dewatto basin). The strain transfer zone at the northwestern margin of the Tacoma basin and western extension of the Seattle Fault Zone may kinematically link the Seattle, Tacoma and Saddle Mountain Fault systems. This zone facilitates strain partitioning between the Olympic Massif and Puget Lowland. Rupture along the overall length of these linked faults systems could produce a $>$ M7 earthquake.

CHAPTER 3:

THE FIELD OF PAIN STUDY SITE

3.1 Introduction

We use 3-D seismic, self-potential, and DC electrical resistivity data to investigate an area of upwelling hot water in a site that is here termed Long's field after the surname of the property's owner. The DC electrical resistivity and self-potential data previously identified an area of upwelling hot water that has been interpreted to be the consequence of small tensile fractures located 500 m south of the intersection between the Sawatch and Chalk Creek faults (Richards *et al.*, 2010). These tensile fractures are likely related to the local dilatant stress field that have been shown to radiate from fault tips at intersecting faults in regions with similar structural geology (Roberts, 1996). Our objective is to identify and characterize these fractures through the use of various near surface geophysical methods. We use the results of our data processing to further enhance the interpretations of Richards *et al.* (2010) by jointly interpreting seismic results with DC resistivity and self-potential data.

3.1.1 Study Site Background

Long's field is Quaternary glacial till and alluvial sediments overlying geothermally altered Tertiary quartz monzonite. The field is at a lateral transition between hot and cold ground water as observed in water wells in the area (Figure 3.1). Hot water wells are aligned in east-west with the most northerly and southerly wells defining a 200 m

corridor with geothermal activity. Self-potential and DC resistivity surveys helped explain the possible reasons for the pattern of hot water wells in the valley (Richards *et al.*, 2010) and identified specific areas of upwelling hot water that were interpreted to coincide with Fault A Figure 3.1. To further investigate these upwelling hot water events, we designed a 235 m by 220 m high-resolution multicomponent 3-D seismic survey to coincide with the largest upwelling event located at the eastern portions of this corridor (Figures 3.1 and 3.2).

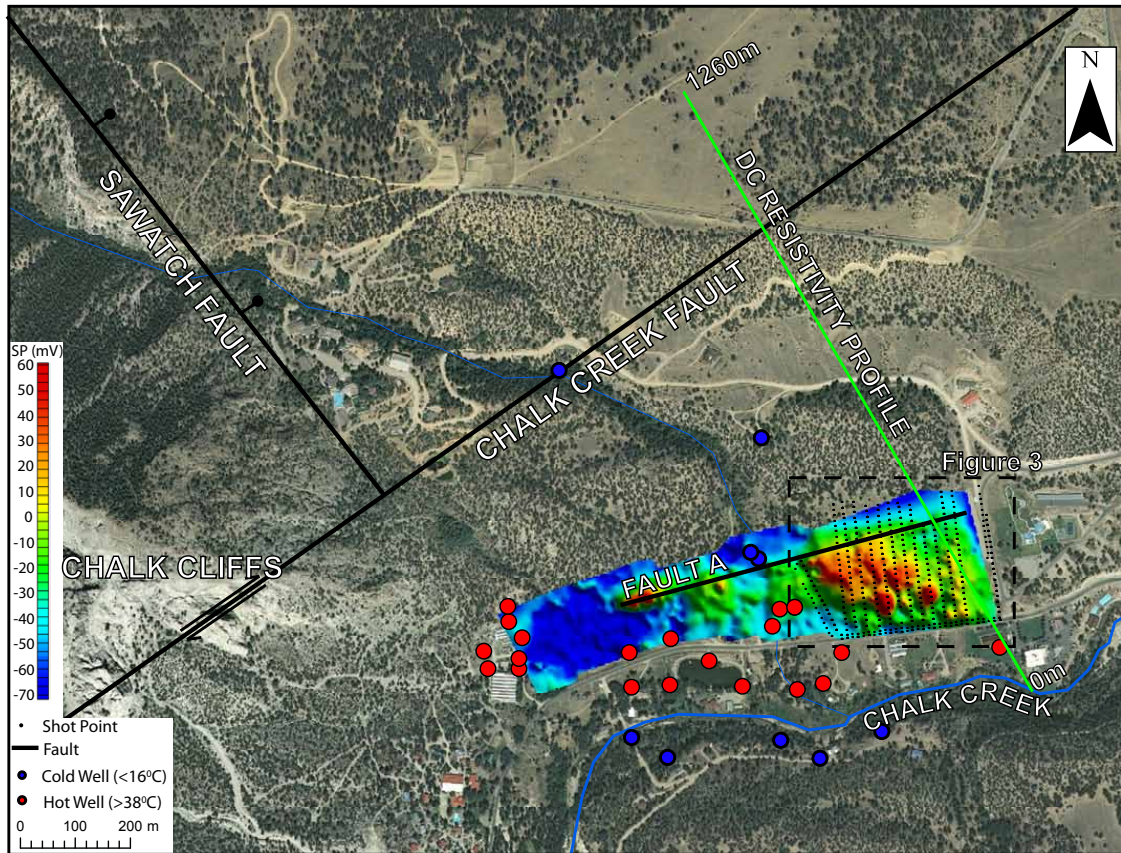


Figure 3.1: Major fault systems and Long's Field located at the north-west corner of Mount Princeton Hot Springs Resort where the 3-D seismic, self-potential, and DC resistivity surveys were conducted. The rainbow colors represent self-potential anomalies in mV with high (red) values indicating upwelling ground water and low values (blue) representing downwelling ground water. The self-potential anomaly data is overlaid with the 3-D seismic survey shot points that are shown in more detail in Figure 3.2.

3.2 Data Acquisition and Processing

The 3-D seismic survey design is shown in Figure 3.2 and the acquisition parameters are summarized in Table 3.1. With a 192 channel recording system and a 576-receiver spread, the active receiver spread was rolled over three times and all shot stations revisited for each of these three receiver spreads.

A standard reflection processing flow was undertaken to develop a 3-D volume stack (Yilmaz, 2001). Due to a complex geology and resulting wave-field, reflections were difficult to separate from other seismic modes. We therefore carried out a 2-D and 3-D refraction tomography analysis using two separate methods to characterize the subsurface and map the boundary between the upper sediments and geothermally altered quartz monzonite. Our 2-D and 3-D refraction tomography results were based upon the commercial refraction tomography softwares RayFract (Intelligent Resources Inc.) and Seismic Studio (FusionGeo LLC.), respectively. We used model grid cell resolutions of 0.5 m for the 2-D tomography and 2 m for the 3-D tomography. For this reason the 3-D refraction results show a significantly smoother representation of the subsurface than the 2-D refraction results.

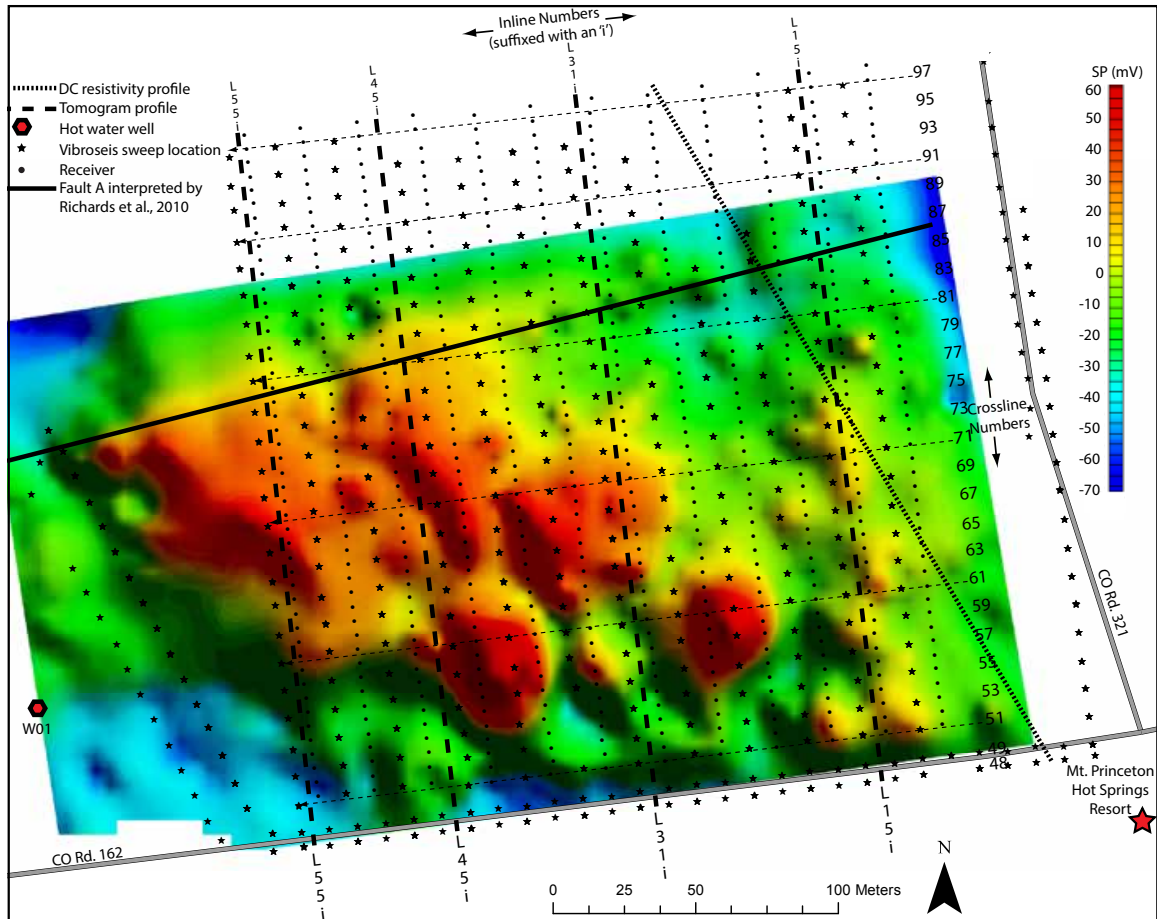


Figure 3.2: Long's Field, located at the north-west corner of Mount Princeton Hot Springs Resort where the 3-D seismic, self-potential, and DC resistivity surveys were conducted. The rainbow colors represent self-potential anomalies in mV with high and low values representing upwelling and downwelling ground water respectively. The self-potential anomaly data is overlaid with the 3-D seismic survey grid that shows the nomenclature used for inline and crossline receiver and shot stations and the lines along which velocity tomograms were modeled (dashed lines). The map also shows a 2-D DC resistivity profile which traversed in a north-northwest direction across the eastern portions of the field. Fault A shown to strike in an east-west direction across the field is based upon work by Richards *et al.* (2010).

| | |
|--------------------|--|
| Seismograph | 192-channel Geometrics geode |
| Vertical geophones | 40 Hz |
| Source | 6,000 lb Industrial Vehicles Minivib T-15000 |
| Sweep | 12 second linear 30-300 Hz |
| Shot spacing | 10 m inline (S-N) x 20 m crossline (E-W) |
| Receiver spacing | 5 m inline (S-N) x 20 m crossline (E-E) |
| Sample rate | 1 ms |

Table 3.1: Seismic acquisition parameters.

3.3 Results and Discussion

Panel A of Figure 3.3 shows the interpretation of a DC resistivity profile whose location is shown in Figure 3.2. The calculated resistivity values for the upper 100 m depth are relatively low, indicating an absence of competent bedrock and instead the presence of clays and severely altered bedrock. Typical resistivity values for altered, saturated and fractured quartz monzonite that may be further altered to kaolinite range from 100 to 2,000 ohm.m while competent quartz monzonite range from 2,000 to 10,000 ohm.m. Abrupt lateral contrasts in resistivity suggest offset stratigraphy that we interpret as near-vertical faults. Figure 3.4 also shows one of the shot gathers used to create the 2-D velocity tomogram. We interpret two primary refractions on this shot gather that are generally present on all shot gathers. This shot gather highlights the variability of the deep refraction and shows a 7 ms downward step along the interpreted bedrock surface near station 91. Linear moveout analyses were performed on the two dominant refractions observed in all of the 3-D seismic surveys shot gathers. This linear move-out analysis found the velocity for the first

refraction to be from 1750 m/s to 2100 m/s while the second refraction was found to be from 310 m/s to 3300 m/s. We interpret the first refraction as the interface that separates unsaturated and saturated sediments. Water table information from local wells supports this interpretation. We interpret the ~ 3200 m/s refraction to be from the bedrock surface and its depth is supported by a previous deep reflection seismic survey results that shows the basement reflector shallowing near our site (Blum *et al.*, 2009). In addition, vertical seismic profiling of wells in the valley showed similar bedrock depths and velocities (Blum *et al.*, 2009). The relatively low velocity of ~ 3200 m/s for what we expect to be quartz monzonite with velocities in the range of 5000 m/s suggest that the bedrock is severely altered and fractured. This low velocity in conjunction with the previously discussed low resistivities (>100 ohm.m) provides further evidence for severe fracturing and possible alteration to kaolinite as observed on the exposed Chalk Cliffs 800 m to the west of Long's field.

Figures 3.3 and 3.5 show velocity profiles from 2-D refraction modeling and each tomogram is plotted with the corresponding self-potential data. Our interpretations are based upon our combined observations on all the processed 2-D and 3-D seismic and potential field data. The refraction tomography inherently smoothes the subsurface structure and this is also true of the self-potential and DC resistivity inversions. For these reasons, our interpretations take into account these smoothing effects and faults are interpreted where large lateral gradients appear in the velocity or DC resistivity models. All of the 2-D velocity tomograms show the bedrock dipping to the south with average bedrock dips between 20° and 50° , and localized maximum dips of up to 50° (e.g., stations 73 and 85 on L31i and station 77 on L15i). The eastern lines L15i and L31i have the highest dip angles. Line L15i shows a 15 m

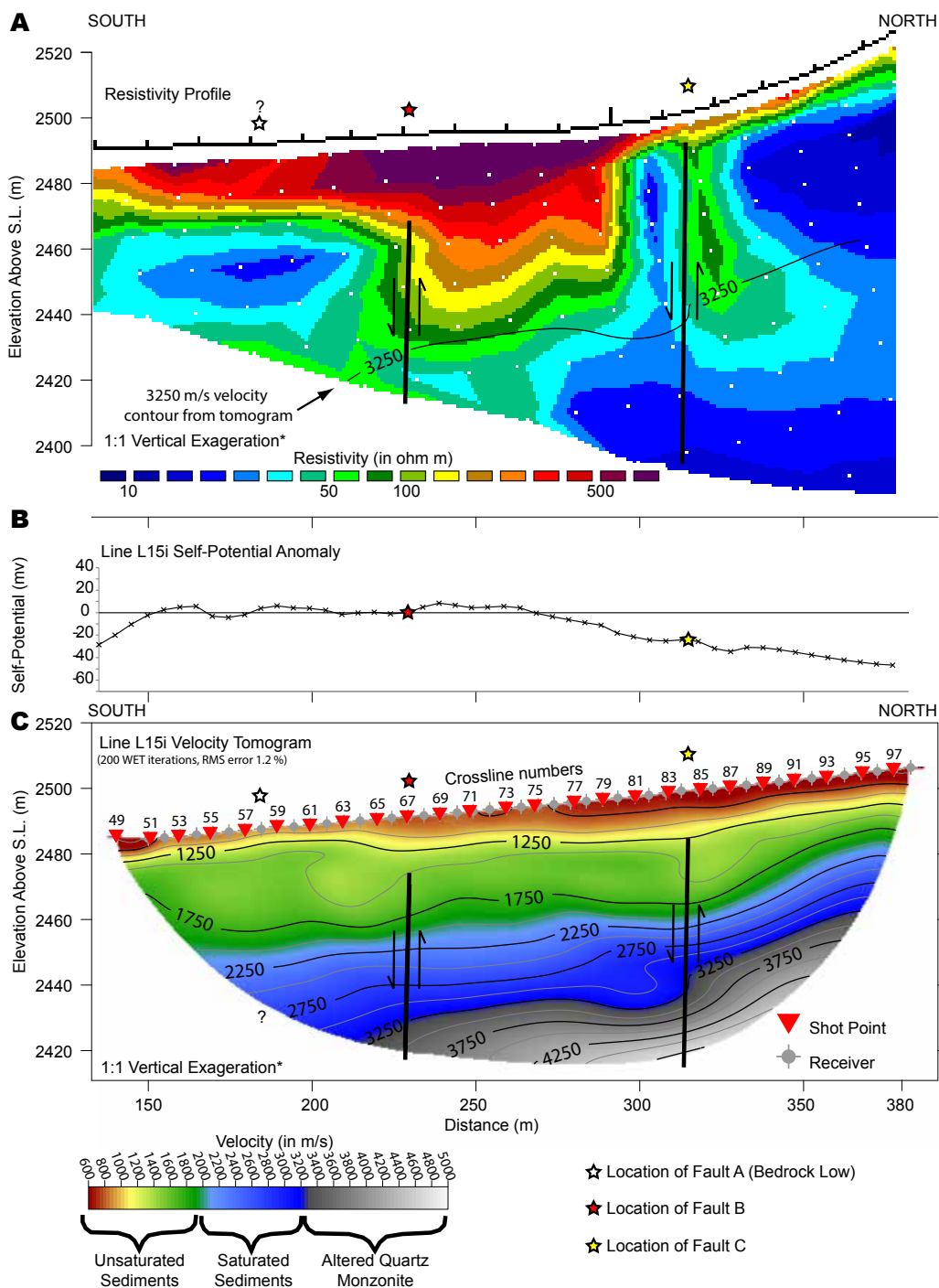


Figure 3.3: Panel A shows the DC resistivity inversion result for the DC resistivity line. Panels B and C show the self-potential and 2-D refraction tomography results for L15i. Line locations are shown in Figures 3.1 and 3.2

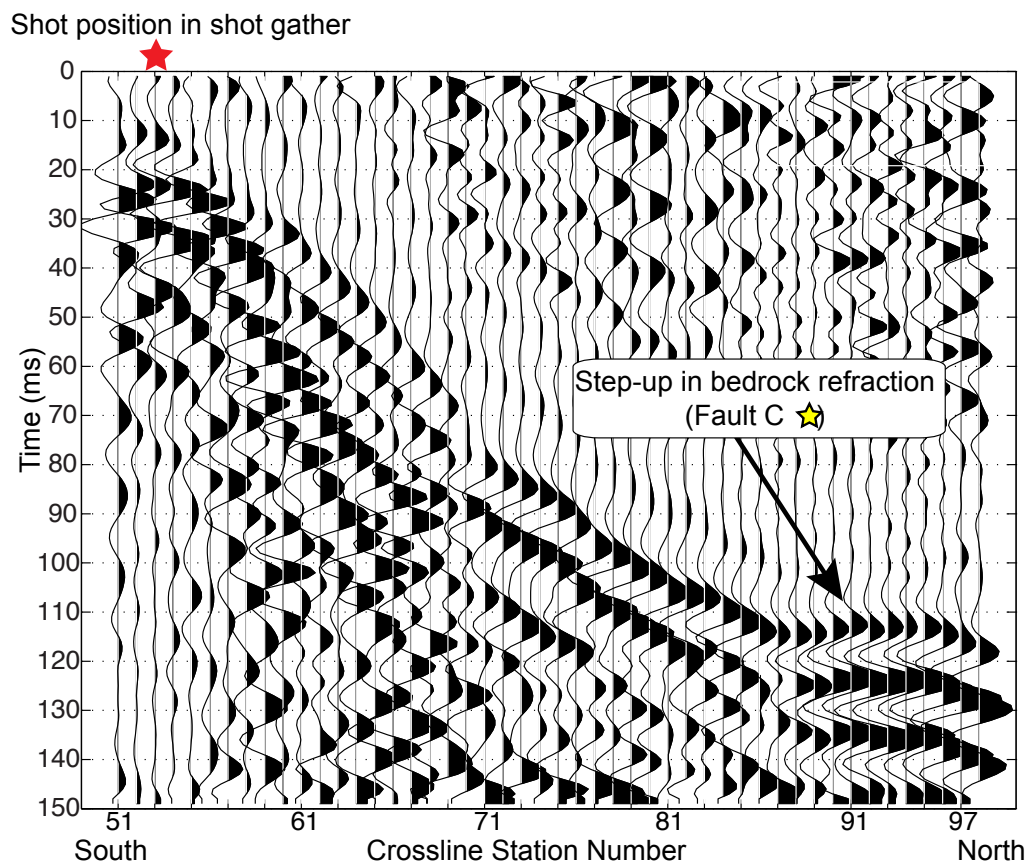


Figure 3.4: A shot gather on L15i at station 53 showing a step-up in the bedrock refraction at station 91 that is common to many of the shots shooting northwards in the eastern half of Long's field.

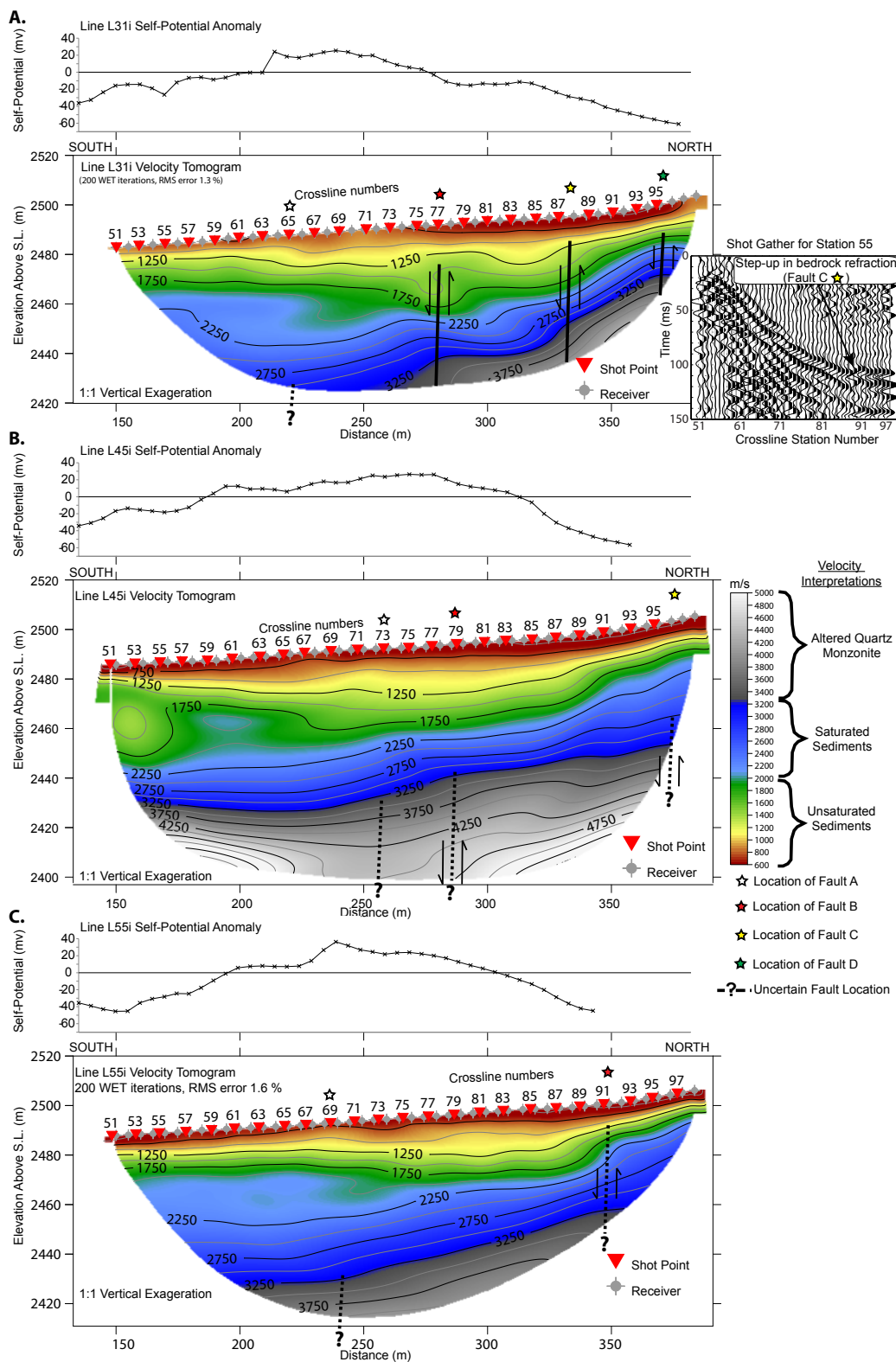


Figure 3.5: Panels A, B and C show the self-potential and 2-D refraction tomography results for lines L31i, L45i and L55i (see Figure 3.2). Our interpreted location of Faults A through D are shown on each of the three panels along with a shot gather from station 55 on line L31i.

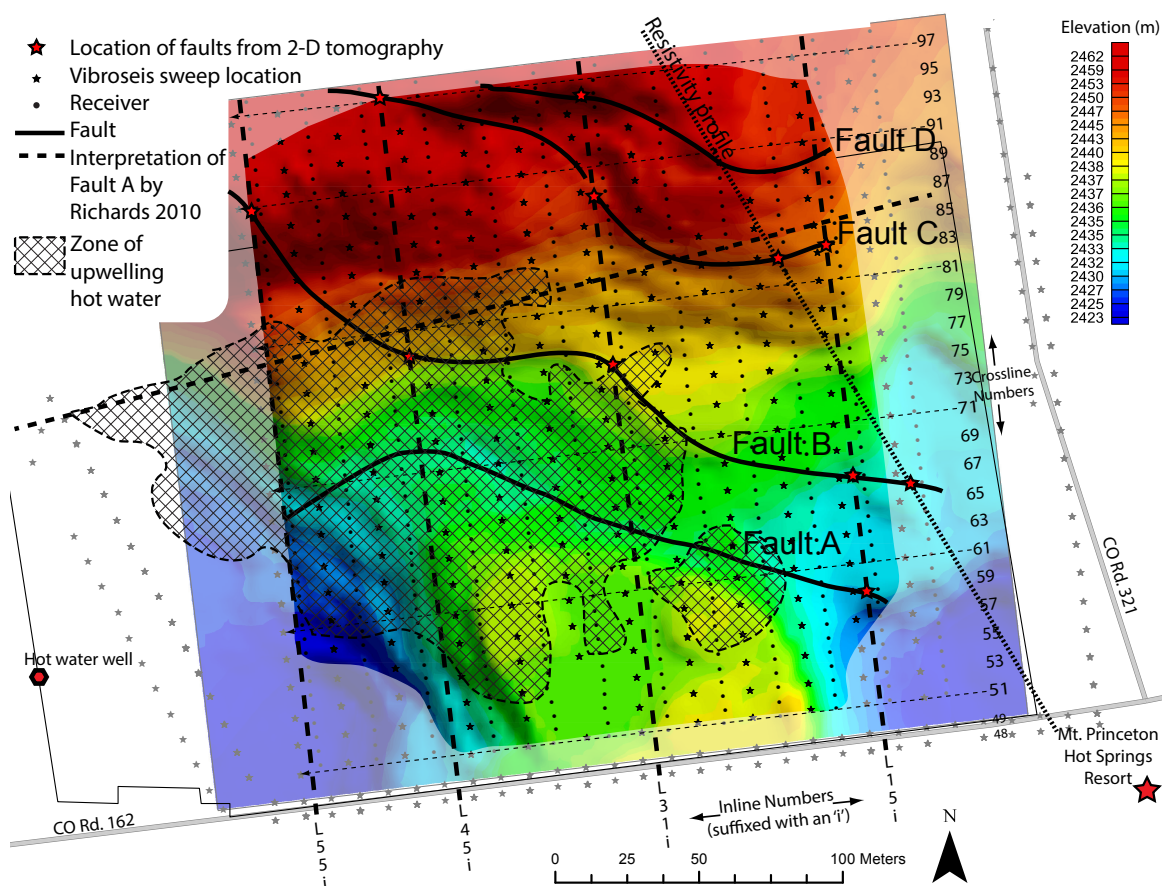


Figure 3.6: Figure showing the elevation above sea level for the 3250 m/s velocity isosurface using the 3-D tomography code. The figure is overlaid with our joint seismic, 2-D refraction, DC resistivity, and self-potential interpretations. The 3250 m/s velocity isosurface is interpreted to represent the top of the altered quartz monzonite where high elevation is represented by red and low elevation by blue. The bedrock surface elevation is overlaid with the 3-D seismic survey grid that shows the 2-D tomogram and resistivity profile locations. The subdued colors bordering the 3-D refraction results represent areas of low ray coverage for which the calculated velocities are not well constrained and therefore interpreted with caution.

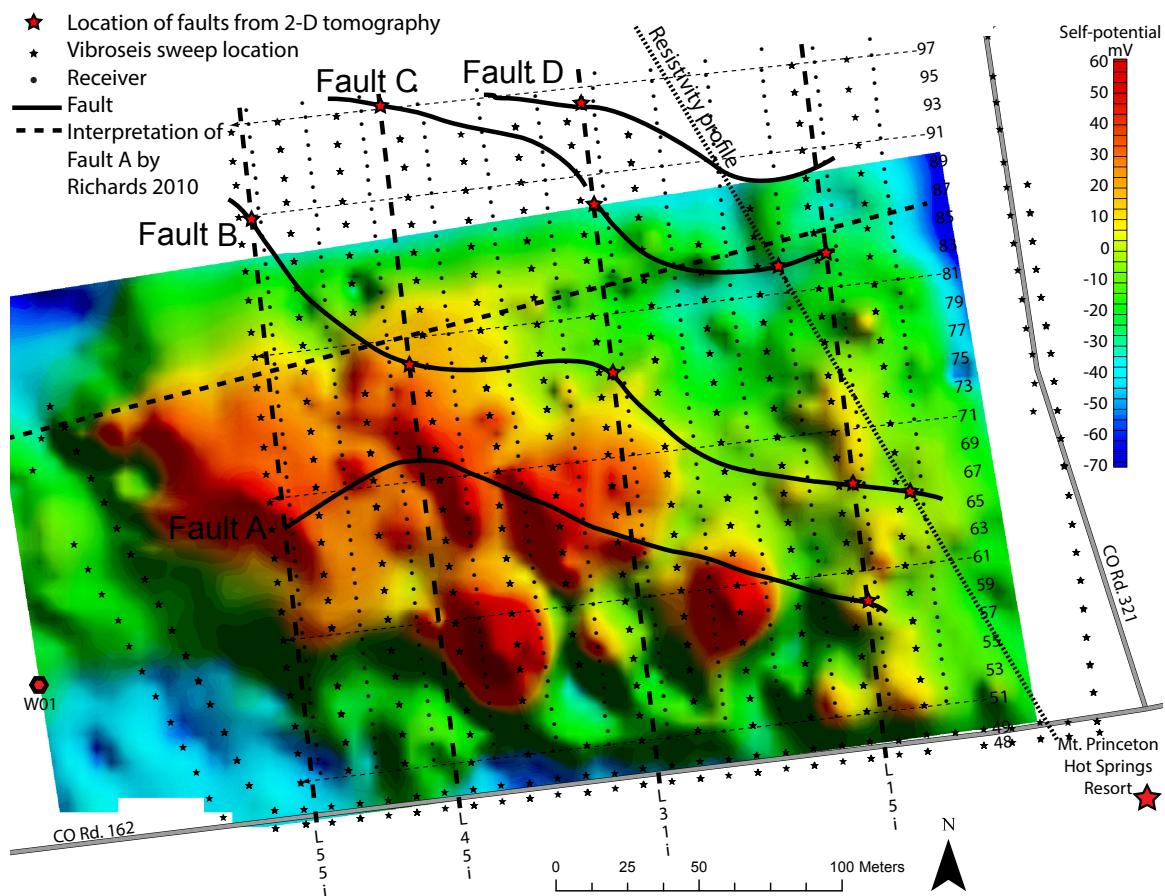


Figure 3.7: Figure showing our interpretations superimposed on the self-potential anomaly map. The figure is overlaid with the 3-D seismic survey grid that shows the 2-D tomogram and resistivity profile locations.

south-side down offset in the bedrock at station 84 and a further south-side down offset at station 67. These two south-side down bedrock offsets in line L15i correspond with two steep dipping low resistivity anomalies observed in the results of a 2-D DC resistivity profile that was acquired diagonally across L15i (Figures 3.2 and 3.3). These anomalies are indicative of faulting and their low resistivities may be due to the presence of hot water and increased alteration. The superposition of resistivity and seismic anomalies provides strong evidence for two faults that we term Faults B and C. We identify three south-side down bedrock offsets on Line L31i (Figure 3.5) at stations 95, 88, and 77. Offsets of 10 m at stations 88 and 77 are similar in throw to the offsets at stations 88 and 67 on line L15i and we interpret these steps in bedrock as continuations of Faults B and C. The L45i and L55i velocity tomograms (Figure 3.5) that lie further to the west do not exhibit similar bedrock offsets to lines L15i and L31i, however there are more subtle south-side down offsets at the mid to northern portions of these lines that may represent westward continuations of faults (see Figure 3.5).

The 3-D tomography and self-potential maps are presented in Figures 3.6 and 3.7. Figure 3.6 shows a 20° and 50° south dipping bedrock surface at the northern section of the field and both panels show evidence for northwest-southeast trending anomalies. These trends are more subtle in the 3-D tomography results than the self-potential results; however, a combined interpretation of these maps with our 2-D interpretations (shown in Figures 3.3 and 3.5) suggest that Faults B and C and the less well constrained Fault D likely follow a similar strike direction. Fault C lies along the northern margin of the self-potential anomaly and may therefore be a northern bounding fault for upwelling hot water. This interpretation is consistent with well

temperature data and Fault A interpreted by Richards *et al.* (2010), who showed that Fault A lies parallel to a boundary between hot water wells to the south and cold water wells to the north. The generally east-west trending bedrock contours in Figure 3.6 may represent glacial erosion within Chalk Creek Valley with Fault A coincident with a low in the bedrock surface. Faults B, C, and D all offset the bedrock surface in a northwest-southeast direction and appear to follow similar trends in the individual smaller scale self-potential anomalies of Figure 3.7. These faults have negative self-potential anomalies (representative of downwelling water) and may be conduits for downwelling cold water and boundaries for hot water upwelling along the positive self-potential anomaly. The west-east zone of larger scale positive self-potential anomalies, shown in Figure 3.1, align in the same general direction of the bedrock topography interpreted from seismic refraction data (Figure 3.6). The axial bedrock low is also coincident with Fault A that aligns with the larger scale positive self-potential to the west (Figure 3.2) and may be related to an area of structural weakness in the bedrock. It is also possible that the slower bedrock velocities are instead representative of a changing bedrock conditions. This slowdown in refractor velocity could be caused by upwelling hot water degrading the quartz monzonite. It is therefore inconsequential as to whether the bedrock low is real or apparent because a bedrock low or velocity slow down could both be interpreted to represent an area of structural weakness and a source of upwelling hot water.

3.4 Conclusions

Our investigations have shown a correlation between the seismic, self-potential, and DC resistivity data and how these combined datasets can be successfully used to

characterize the near surface of a geothermal system. We have presented evidence for three faults and a bedrock low axis by jointly interpreting seismic, self-potential, and resistivity data. Our interpretations indicate that the positive east-west self-potential anomaly follows a low axial surface in the bedrock that may alternatively be a low velocity zone representative of the quartz monzonite that is severely altered by upwelling hot water. Our interpretations also suggest that Faults B, C, and D may be a bounding fault for the northern edge of the self-potential anomaly and are conduits for downwelling cold water. The strike directions of Faults B, C, and D follow a northwest to southeast trend that align with the intersection of the Sawatch and Chalk Creek faults. The upwelling hot water events observed by self-potential methods appear to follow a bedrock low/weakness whose strike direction passes through the Mount Princeton Hot Springs resort. This bedrock low/weakness is likely responsible for the hot water springs naturally upwelling in the area, as previously stated by Richards *et al.* (2010). We also conclude that the staggered northwest-southeast striking faults and low bedrock velocities all suggest the quartz monzonite is both significantly fractured and geothermally altered.

CHAPTER 4:

DEADHORSE LAKE, MOUNT PRINCETON:

NEAR SURFACE CHARACTERIZATION WITH

MULTI-COMPONENT SURFACE WAVE

CORRELATIONS

4.1 Glossary of Mathematical Terms Used

| | |
|-----------------------------|---|
| z | vertical direction |
| x | radial direction |
| zx | A vertical/radial component that is based on the cross-correlations between the radial and vertical wavefields |
| $r(s_2, s_1)$ | distance between stations s_1 and s_2 in meters |
| $R(s_2, s_1)$ | number of station intervals between stations s_1 and s_2 |
| $U_z(s, t)$ | Vertical wavefield for receiver station s |
| $U_{zx}(s, t)$ | Vertical wavefield for a radial source function |
| $U_{zx}(r(s_2, s_1), t)$ | Vertical wavefield recorded at station s_2 for a radial source function at station s_1 |
| $G_{zx}(s_2, s_1, t)$ | The Green's function at station s_1 found by cross-correlating $U_x(s_1, t)$ with $U_z(s_2, t)$ |
| $\phi_{zx}(r(s_2, s_1), f)$ | The cross-correlation coefficient found by taking the real part of the Fourier transform of $G_{zx}(s_2, s_1, t)$ |
| $c_{zx}(r(s_2, s_1), f)$ | The phase velocity for $\phi_{zx}(r(s_2, s_1), f)$ |
| m_{zx} | Number of missed zero crossings for $\phi_{zx}(r(s_2, s_1), f)$ |
| c_{zx}^m | The phase velocity for $m = m_1$ missed zero crossings using ϕ_{zx} |

Table 4.1: Glossary of mathematical terms used.

4.2 Introduction

Retrieving near-surface information about the subsurface from surface wave dispersion is important for geotechnical applications, but also in exploration for deeper targets. Multichannel analysis of surface waves (MASW; e.g., Park *et al.*, 1999) and surface wave spectral analysis that uses both active and ambient noise sources (Refraction Microtremor (REMI); Louie, 2001) are popular techniques to map near surface structure. In a medium with heterogeneous velocities, waves with different frequencies will propagate at differing phase velocities. These dispersive properties of waves can be retrieved using such surface wave analysis techniques. Retrieving these dispersive properties allows us to invert for phase velocity as a function of depth. Here we introduce a new surface wave analysis method called the multi-component MuSPAC method. This method is an extension of the Spatial Autocorrelation (SPAC) method (Aki, 1957) and is similar in application to the REMI method (Louie, 2001). The REMI and SPAC methods (Ekström *et al.*, 2009; Stephenson *et al.*, 2009) cross-correlate only the vertical components of the wavefield to estimate phase velocity of the surface waves. The MuSPAC method takes advantage of the additional information involving the radial components of the wavefield to improve the signal to noise ratio and reduce error. The MuSPAC technique correlates every combination of vertical and radial components of the wavefield to extract the most accurate and robust estimates of the dispersive properties of Rayleigh waves. By using these additional components, it can potentially improve characterization and resolution of the near surface elastic parameters and depth of the layers.

An advantage of MuSPAC, just as in REMI and SPAC, over conventional analysis of source-receiver data, is that uncorrelated vibroseis data recorded at the receivers

can be used directly thereby avoiding introducing error through correlating with the source signature sweep. MuSPAC also requires no knowledge of source timing or orientation. This opens up the possibility of working in blended vibroseis acquisition (Berkhout, 2012) and expanding to case of 2-D acquisition, where the analytical solutions are zero and first order Bessel functions, instead of cosine and sine functions (Haney *et al.*, 2012).

Seismic interferometry pertains to the correlation of wavefields detected at two receivers, where correlation (or convolution) of these wavefields in the time domain result in an estimate of the impulse response between receivers. In the frequency domain, the SPAC method does the same (Aki, 1957), and is successfully applied throughout seismology (Ekström *et al.*, 2009; Stephenson *et al.*, 2009). The equivalence of these two methods in different domains is shown by Tsai and Moschetti (2010). van Wijk *et al.* (2011) explored correlations of the cross-components of the Green tensor of the wavefield and found these to be more robust in the presence of uneven illumination of the receivers. This was followed by an extension of the SPAC method to all components of the Green tensor by Haney *et al.* (2012). Here we use numerical modeling of the cross and diagonal terms in the frequency domain to explore how these improve retrieval of the Rayleigh wave velocity. We then apply the method to active source seismic data acquired at a geothermal field site at Mount Princeton Hot Springs, Colorado.

4.3 The SPAC and MuSPAC Methods as Applied to a Homogeneous Half-Space

In this section, the SPAC and MuSPAC methods are introduced by modeling a full-band Rayleigh wave chirp signal propagating through a homogeneous elastic infinite half-space. We examine the issues presented to us when we have body waves and partial-band frequency data, and examine how this may be overcome for application of the method to partial-band field data.

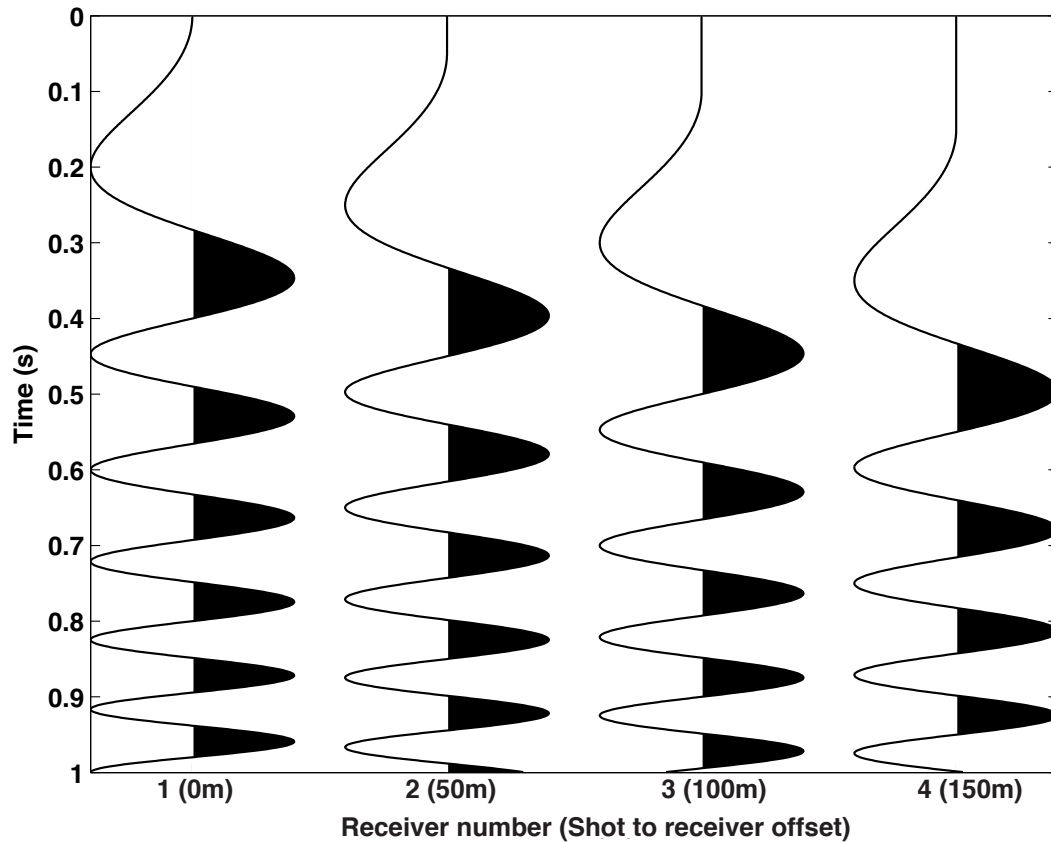


Figure 4.1: The vertical component $U_z(r, t)$ recorded by four receivers for a source located at the first receiver (0 m offset). The source swept from 0 to 150 Hz in 12 s. Only the first second of the time record is shown for viewing purposes.

Consider a Rayleigh wave traveling with a velocity $c = 400$ m/s along the interface of a homogeneous elastic infinite half-space with absorbing boundaries. The vertical component of this wavefield $U_z(r, t)$ is depicted in Figure 4.1 as a function of source-receiver offset. Without attenuation, geometric spreading, or variations in velocity, these wavefields are simply translated versions of each other. The time delay between receivers with increasing shot-receiver offset is a function of the wave velocity. It is therefore quite intuitive that the cross-correlation of the wavefields from two receivers $G_{zz}(s_1, s_2, t) = U_z(s_1, t) \otimes U_z(s_2, t)$ results in a (partial-band) impulse arriving at time $t = r/c$, where $r = s_2 - s_1$ is the inter-receiver offset and c is the Rayleigh-wave velocity.

Figure 4.2 shows $G_{zz}(2, 3, t)$, where the central pulse arrival at 0.125 seconds estimates a Rayleigh wave velocity of $c = 400$ m/s. In the idealized case where all frequencies are represented in the (chirp) source signal, the causal and anti-causal Rayleigh wave impulse response approaches the Dirac delta functions:

$$G(r, t) = \delta(t - r/c) + \delta(t + r/c). \quad (4.1)$$

This correlation technique is the basis of seismic interferometry, where correlating wavefields from a collection of sources provides the impulse response between receivers. This has the potential advantage of turning receivers into sources.

In the frequency domain, this technique is called SPAC, and the real part of the Fourier transform of the retarded Dirac delta function is

$$\phi_{zz}(r, \omega) = \Re[\mathcal{F}(\delta(t - r/c))] = \cos(\omega r/c), \quad (4.2)$$

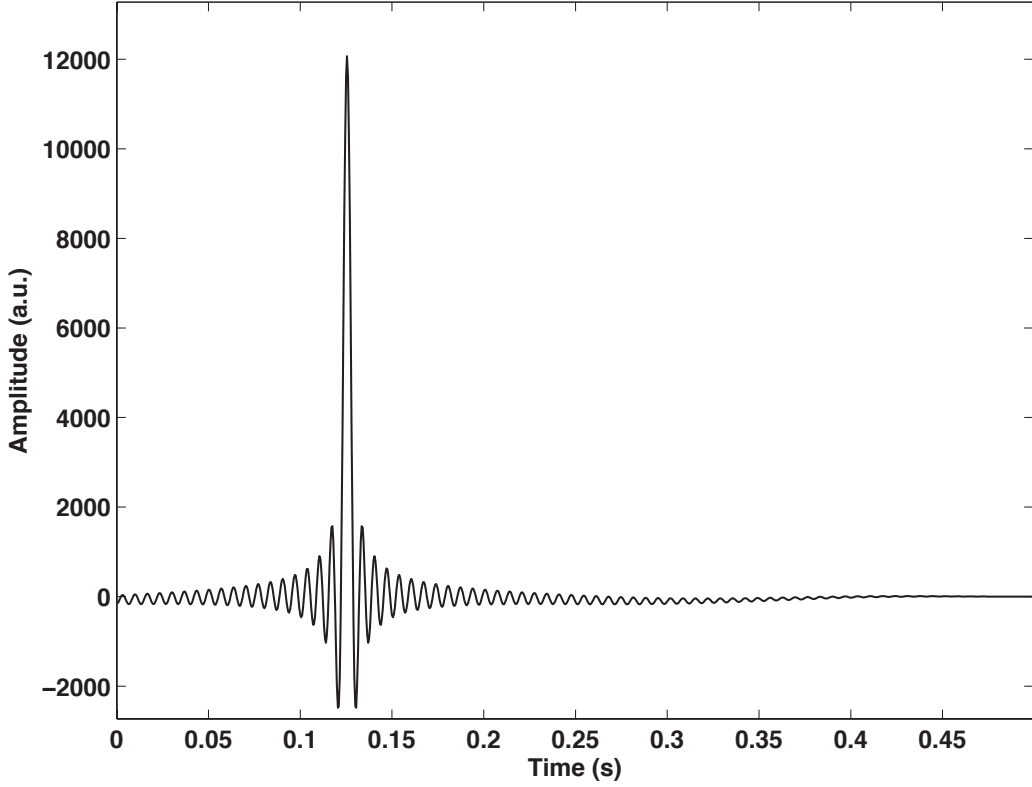


Figure 4.2: The causal Green's function, $G_{zz}(2, 3, t)$, found by cross-correlating the vertical wavefield components of $U_z(r, t)$ at receivers 2 and 3 with a separation distance of 50m. The center of the pulse arrives at $t = 0.125$ s, which indicates a Rayleigh-wave velocity of 400 m/s.

where ϕ was referred to by Aki (1957) as the SPAC coefficient.

The expression in equation 4.2 is confirmed by ϕ_{zz} in Figure 4.3. Equation (26) of Haney *et al.* (2012) summarizes the derivation for the extension of the 1-D version of the SPAC method for Rayleigh waves to include all components of the Green tensor:

$$\phi(r, \omega) = \begin{bmatrix} \phi_{zz} & \phi_{zx} \\ \phi_{xz} & \phi_{xx} \end{bmatrix} = P(\omega) \begin{bmatrix} \cos(\omega r/c) & -R \sin(|\omega|r/c) \\ R \sin(|\omega|r/c) & R^2 \cos(\omega r/c) \end{bmatrix} \quad (4.3)$$

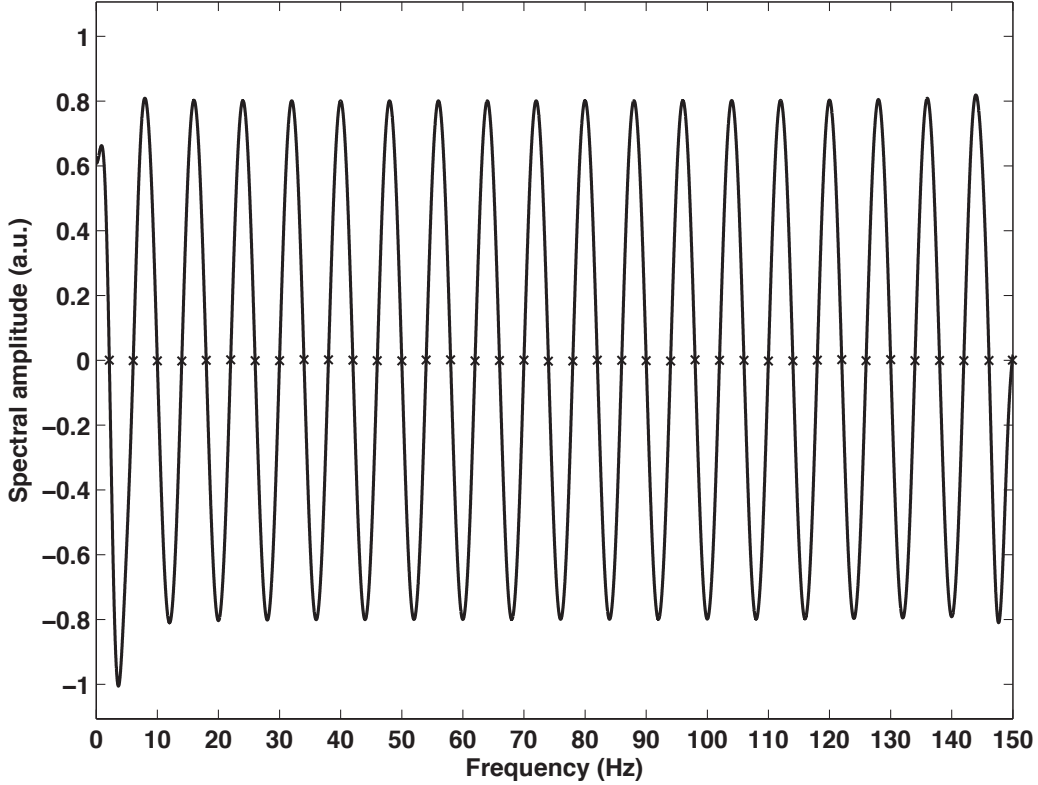


Figure 4.3: The SPAC coefficients $\phi_{zz}(2, 3, f)$ that are the real part of the Fourier transform of $G_{zz}(2, 3, t)$.

where R is the ratio of the horizontal-to-vertical displacement of the Rayleigh waves and $P(\omega)$ is the power spectrum of the Rayleigh waves.

In seismic interferometry one typically retrieves the phase, rather than the amplitude of the impulse response between receivers. It is therefore convenient to represent the n th root of the cosine function (where $\phi = 0$). By substituting the expression $\omega r/c = n\pi - \pi/2$ into the diagonal-terms of Equation 4.3, we find that

$$c_{zz}(\omega_n) = c_{xx}(\omega_n) = \frac{\omega_n r}{n\pi - \pi/2}, \quad (4.4)$$

where the subscripts on c represent each of the diagonal-terms in Equation 4.3. With this equation, we can estimate the Rayleigh velocity as a function of n frequency.

This is in essence the SPAC method in 1-D, as derived in Aki (1957), and leads to the estimate of the (homogeneous) Rayleigh-wave speed in Figure 4.4. The MuSPAC method extends the SPAC method by using the cross-terms in Equation 4.3. In this case, we represent the n th roots of the sine function by substituting the expression $\omega r/c = n\pi$ into the cross-terms of Equation 4.3, so that

$$c_{zz}(\omega_n) = c_{xx}(\omega_n) = \frac{\omega_n r}{n\pi}, \quad (4.5)$$

where the subscripts on c represent each of the cross-terms in Equation 4.3.

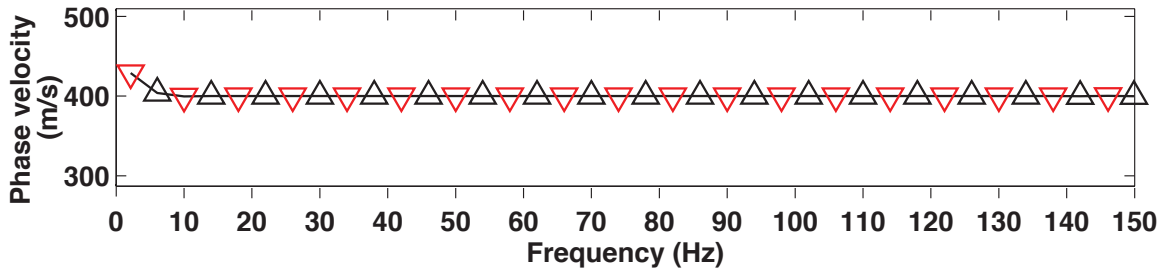


Figure 4.4: The zero crossings of the real part of the Fourier transform of the correlation between receivers 2 and 3 to estimate the wave speed as a function of frequency.

In summary, the MuSPAC methods ability to use interferometry and two-component recorded data has the ultimate benefit of improving the accuracy of our phase velocity estimations. This is done through: 1) the addition of three dispersion curves thus providing more resolution, 2) the inherent reduction in noise caused by cross-correlating the recorded wavefields, and 3) the ability to use any source term, thus eliminating any issues such as source timing and triggering.

4.4 MuSPAC and Partial-Band Data in a Homogeneous Half-Space

4.4.1 Introduction and Experimental Setup

In field settings, heterogeneity in the subsurface will add features to the estimated impulse response associated with reflections and other body waves. This, and inherent noise in field data, will contaminate the retrieval of the Rayleigh wave and its phase velocity as a function of frequency. The Rayleigh wave contains information on the subsurface velocity structure and by minimizing the contaminating noise and body wave artifacts we can use MuSPAC to retrieve the phase velocity dispersion curve and invert for the velocity structure. The realistic field setting will also have partial-band data and therefore there will be an unknown number of missed zero crossings in the interval between 0 Hz and the minimum frequency available in our data.

We use a homogeneous elastic infinite half-space with a velocity $c = 500 \text{ m/s}$ to compare the MuSPAC results for full-band and partial-band data. The full-band source used is a 0 to 150 Hz chirp signal swept over a 12 second interval and was previously shown in Figure 4.1. To create partial-band data we use a 30 to 150 Hz chirp signal swept over a 12 second interval.

4.4.2 Results

Here we present the results of our MuSPAC analysis for the full-band and partial-band cases.

The SPAC coefficients for the full-band and partial-band cases are shown in Figure 4.5. The full-band SPAC coefficients are depicted in this figure using semi-

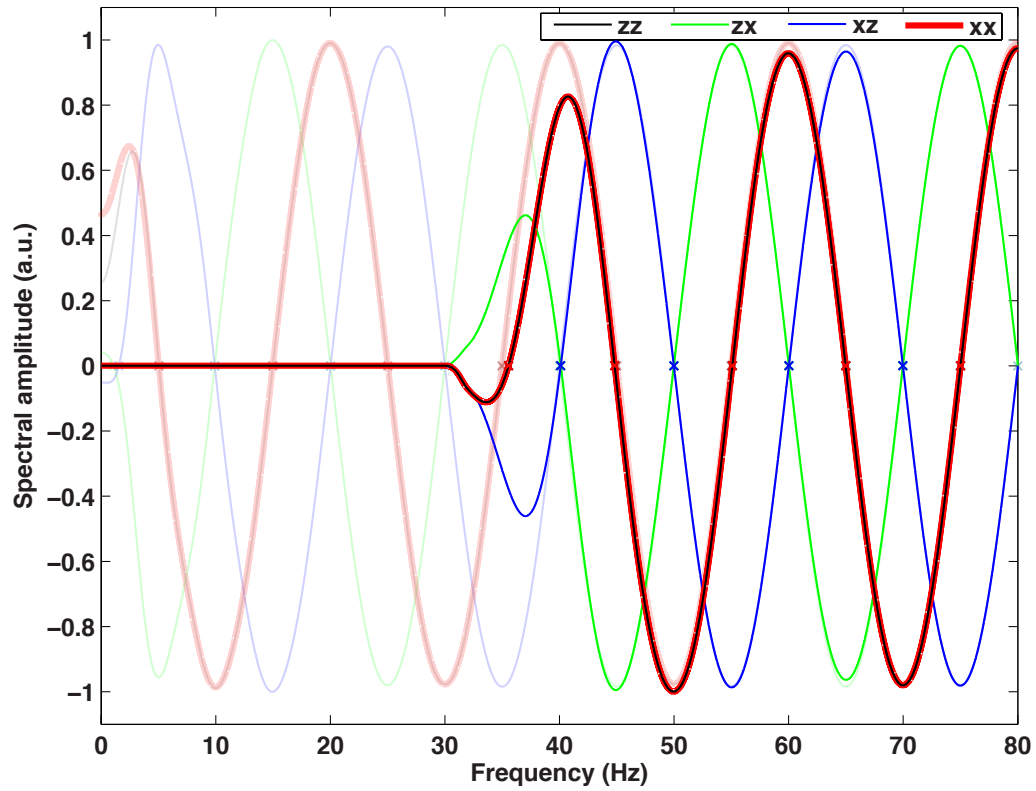


Figure 4.5: The semi-transparent and full-color SPAC coefficients, ϕ_{zz} , ϕ_{zx} , ϕ_{xz} , and ϕ_{xx} are for full-band and partial-band data respectively.

transparent lines and the partial-band SPAC coefficients are overlaid in full color.

In Figure 4.6, the phase velocity dispersion curves for the full-band case are shown using semi-transparent lines and the partial-band dispersion curves are shown in full color.

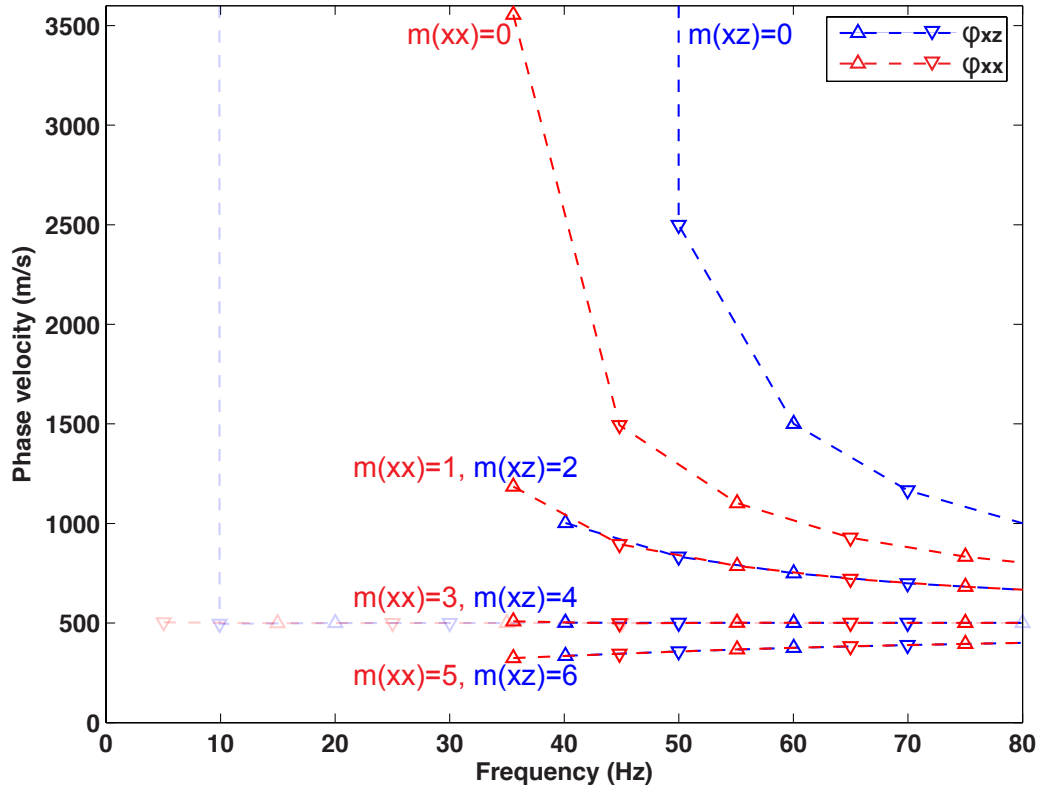


Figure 4.6: The semi-transparent and full color dispersion curves c_{xx} and c_{xz} are for full-band and partial-band data respectively. A sinusoidal chirp sweep from 0 to 150 Hz was used to impart a wavefield into a slab model that was recorded by receivers spaced 25-m apart. The effect of adding up to 6 missing zero crossings ($m=6$) on the partial-band data is shown with $m_{xx} = 3$ and $m_{xz} = 4$ resulting in a match between the partial-band and full-band dispersion curves.

4.4.3 Discussion

Figure 4.5 shows the similarity between the SPAC coefficient ϕ and its zero crossings for the full-band (semi-transparent lines) and partial-band (full-color lines) cases. It demonstrates how the partial-band case is a subset of the full-band case with a certain number of skipped or missing zero crossings. The number of missed zero crossings are related to the model's velocity profile that would have been sampled by the omitted lower frequencies between 0 and 30 Hz. In order to reproduce the correct phase velocities of the partial-band case, we must therefore estimate how many zero crossings have been missed in this 0 to 30 Hz range.

In order to account for missed zero crossings, we follow a similar procedure to Ekström *et al.* (2009), and calculate a series of phase velocity dispersion curves c^m that are based on adaptations of equations 4.4 and 4.5, where for the diagonal/cosine terms we have

$$c_{zz,xx}^m(\omega_n) = \frac{\omega_n r}{(n+m)\pi - \pi/2}, \quad (4.6)$$

and for the sine/cross terms we have

$$c_{zx,xz}^m(\omega_n) = \frac{\omega_n r}{(n+m)\pi}, \quad (4.7)$$

where m represents the number of missed or extra zero crossings and increments in multiples of 2.

Figure 4.6 shows a comparison between dispersion curves for full-band and partial-band data. The figure shows the variability of the dispersion curves should we guess the number of zero crossings below our minimum available frequency in the partial-band data incorrectly. We refer to these guesses as missed zero crossings, m . m can

also be interpreted to represent the sequence number of the first available crossing in our partial-band data, with $m = 0$ representing the first crossing in a full-band scenario if all frequencies were available.

In our MuSPAC method, we use all four SPAC coefficients (ϕ_{zz} , ϕ_{zx} , ϕ_{xz} , and ϕ_{xx}) to help estimate these missed zero crossings and thereby improve our estimation of the phase velocity dispersion curve. In practice, we estimate missed zero crossings by knowing that (1) the roots of the cross-terms must follow a sine function, and the roots of the diagonal terms must follow a cosine function; (2) the phase velocities at our minimum and maximum frequencies must fall within certain reasonable limits that may be further constrained by other field investigations, as done by Ekström *et al.* (2009); and (3) the dispersion curves for all four SPAC coefficients can be jointly interpreted to minimize error.

When m follows an odd number series (e.g., ± 1 , ± 3 , ± 5 ...), this means the first available zero crossing in our data occurs at a slope of ϕ that is opposite in direction to the slope of ϕ at the first missed crossing. Figure 4.5 shows how the slopes of the zero crossings vary between components. For example, the slope is positive for the first crossing of ϕ_{xz} and negative for the other three coefficients ϕ_{zz} , ϕ_{zx} , and ϕ_{xx} .

Figure 4.5 shows the partial-band case missing three crossings for the diagonal-terms ϕ_{zz} and ϕ_{xx} and four crossings for the cross-terms ϕ_{zx} and ϕ_{xz} . We therefore use $m = 3$ in Equation 4.6 for the diagonal-terms and $m = 4$ in Equation 4.7 for the cross-terms, to estimate the relevant phase velocity dispersion curves.

Figure 4.6 shows the phase velocity curves for just the c_{xz} and c_{xx} terms. Like Figure 4.5, the semi-transparent lines in the background are for the full-band case where no zero crossings have been missed. Other than the correct values of $m_{xz} = 4$

and $m_{xx} = 3$, Figure 4.6 shows two other cases where we have both overestimated and underestimated the missed zero crossings for the partial-band data by $m = \pm 2$. The correct velocity for this homogeneous half-space model is $c = 500$ m/s. In the case of overestimating missed zero crossings, we have $m_{xz} = 6$ and $m_{xx} = 5$, which causes the phase velocity to be underestimated by approximately 100 to 200 m/s. In the case of underestimating missed zero crossings, we have $m_{xz} = 2$ and $m_{xx} = 1$, which causes the phase velocity to be overestimated by approximately 200 to 800 m/s. This variability between the dispersion curves for $m = \pm 2$ becomes less with increasing receiver separation distance r , because the larger separation will cause the signals at each receiver to have more skipped phases. Increasing receiver separation therefore makes estimating the number of missed zero crossings more difficult in partial-band data, as there may be a range of values for m that produce realistic looking dispersion curves. This is best overcome by reducing r until two receivers are chosen that give dispersion curves with sufficient variability that enables the correct number of missed zero crossings to be estimated. The trade-off with selecting a smaller value of r is that we will have less zero crossings for the same frequency range thereby giving less resolution. However, this may be more appropriate in the case where the lateral change in velocity may be overly smoothed by using larger values of r .

As seen in Figure 4.6, estimating m is straight forward (through the use of a sine or cosine fit) in the case of no dispersion and a constant velocity; however, it is more difficult when the velocity is not constant. It is also more difficult to estimate the number of missed crossings when the range of the omitted frequency band is greater as this results in more phase changes between receivers and therefore more missed zero crossings.

4.5 MuSPAC and Body Wave Contamination in a Slab Model

4.5.1 Introduction and Experimental Setup

Here we use a partial-band (Ricker) source in a slab model as a means of examining the effects of reflections on the MuSPAC method. We do this by comparing the MuSPAC results using both the cross-correlation result from a single shot gather and the cross-correlation summation for eleven active shot gathers. The summed source data has less contamination from reflected waves because the summing of sources causes destructive interference of reflected energy and constructive interference of surface wave energy.

We use the Spectral Element Method (SEM) to generate synthetic receiver gathers for input into our MuSPAC model. SEM is a high-order variational numerical technique (Priolo *et al.*, 1994; Faccioli *et al.*, 1997) that combines the flexibility of the finite-element method with the accuracy of global pseudo-spectral techniques. The SEM is widely used in seismology (Komatitsch and Vilotte, 1998; Komatitsch and Tromp, 1999, 2002; Komatitsch *et al.*, 2002) and here we use it to simulate wave propagation in an elastic slab.

Figure 4.7 shows the configuration of the geometry and parameters that we use for our slab model. The slab is 50-m thick slab model and it uses P- and S-wave velocities of 900 and 500 m/s, respectively, and this results in a Rayleigh wave velocity

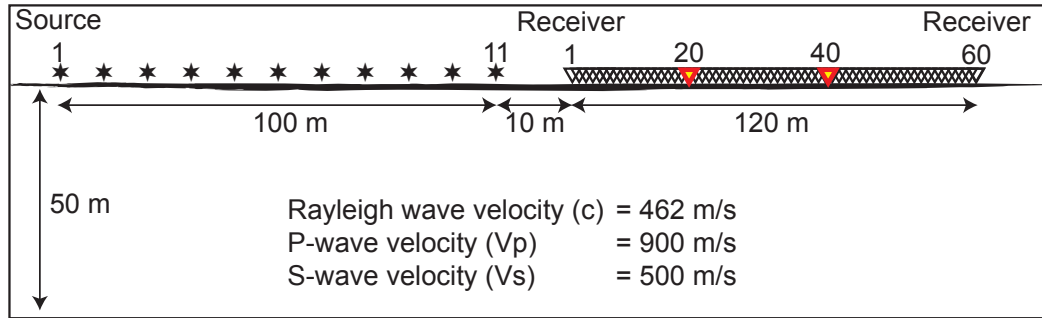


Figure 4.7: A schematic of the single layered slab model used to parameterize the SEM model.

of 462 m/s. This velocity model is parameterized for use in the SEM forward code to generate 11 shot records with offsets to the first receiver ranging from 10 to 110 m. An interval spacing between shot points of 10 m is used. A Ricker wavelet with a dominant frequency of 30 Hz is used as a source. 60 receivers with 2 m spacing are used to record our signal with a sampling rate of 0.5 ms.

Each set of source shot gathers is crosscorrelated using

$$G^s(x', x, t) = U(x^s, x', t) \otimes U(x^s, x, t), \quad (4.8)$$

where \otimes denotes the crosscorrelation, $G(x', x, t)$ is the Green's function for a source at location x' and receiver at x , and $U(x^s, x', t)$ is the particle acceleration at location x' for a source at location x^s .

$G(x', x, t)$ is next summed over N source positions using

$$\underline{G}(x', x, t) = \sum_{s=1}^N G^s(x', x, t) = \sum_{s=1}^N U(x^s, x', t) \otimes U(x^s, x, t), \quad (4.9)$$

where N is the number of sources and $\underline{G}(x', x, t)$ is the crosscorrelation summation for N source positions.

For our example, this process results in a total of 60 virtual shot gathers with receivers off-end to the left. We then use the virtual shot gather located at receiver 20 (shown in red in Figure 4.7) for analysis in the MuSPAC method. We calculate the SPAC coefficients and phase velocity dispersion curves using receivers 20 and 40 from this virtual shot gather. We do this for both single (un-summed) and summed virtual shot gathers. The resulting shot-receiver offset distance is $r = 40$ m.

4.5.2 Results

Figure 4.8 shows the results of a virtual shot gather located at receiver station 1. With this being the farthest virtual shot to the left, its shot gather contains the longest offsets that extend up to 118 m. For this reason, we use it to present the full range of wavefield events that are expected from our slab model and analyzed by the MuSPAC method. With no lateral change in the slab models velocity, all virtual shot gathers from the slab model will have the same wavefield events. The only differences will be that the shot gathers furthest to the right will have fewer traces.

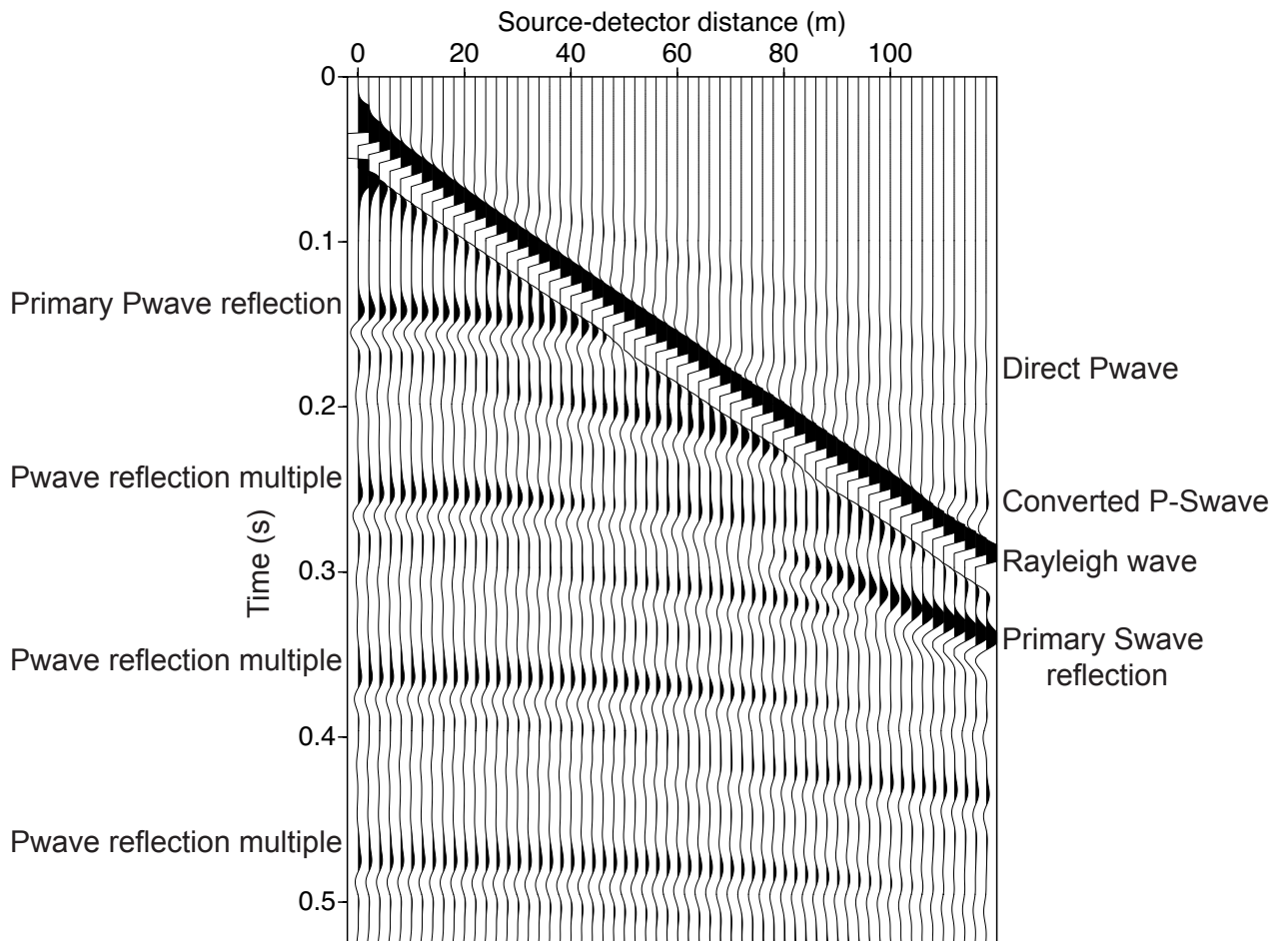


Figure 4.8: The vertical component of a synthetic shot record, U_z , as a function of source-detector offset. The source used is Ricker wavelet with a dominant frequency of 30 Hz. Interpretations of the main wavefield events are shown to the right and left of the shot record.

Figures 4.9 to 4.12 show the results of our MuSPAC analysis that use receiver stations 20 and 40 from a virtual shot record at receiver station 20. These figures compare both the cross-correlations and dispersion curves for both the single and summed versions of this virtual shot record.

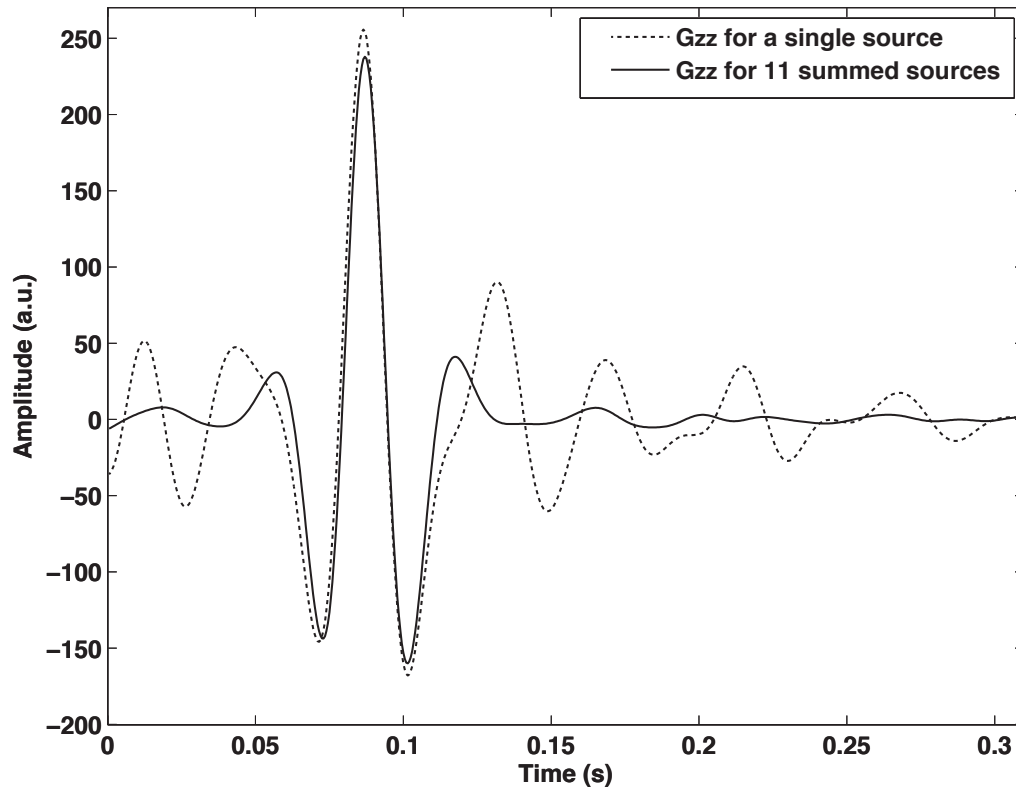


Figure 4.9: Cross-correlations of the vertical component of wavefields for a virtual shot at station 20. Receivers 20 and 40 were used to compare single shot (dotted) and summed shot (solid) correlations.

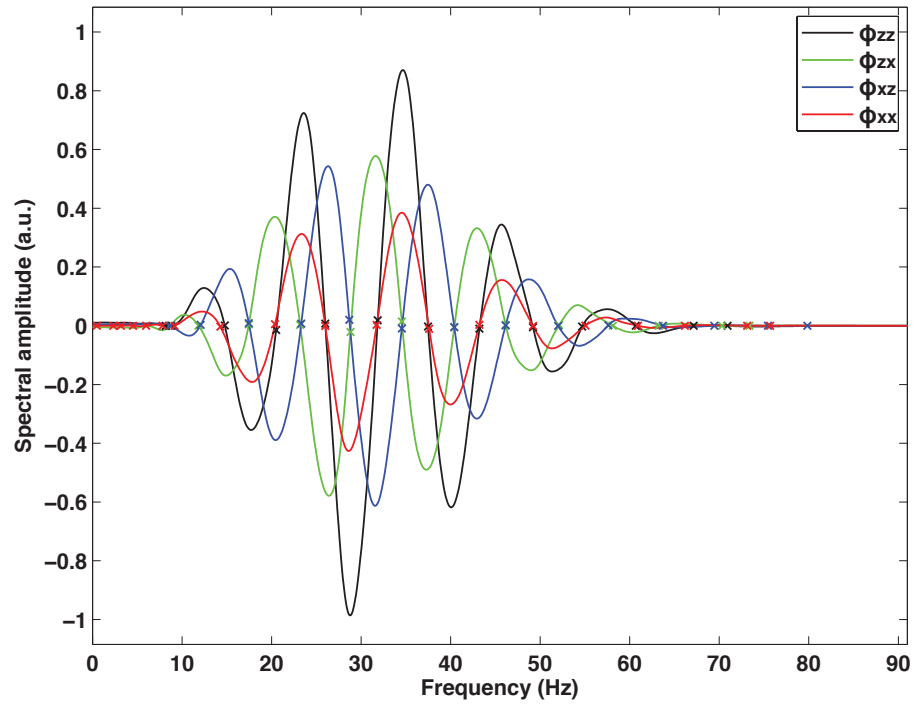


Figure 4.10: Cross-correlations of the vertical component of wavefields of receivers 20 and 40. The real part of the Fourier transform of SPAC coefficients, ϕ_{zz} , ϕ_{zx} , ϕ_{xz} , and ϕ_{xx} .

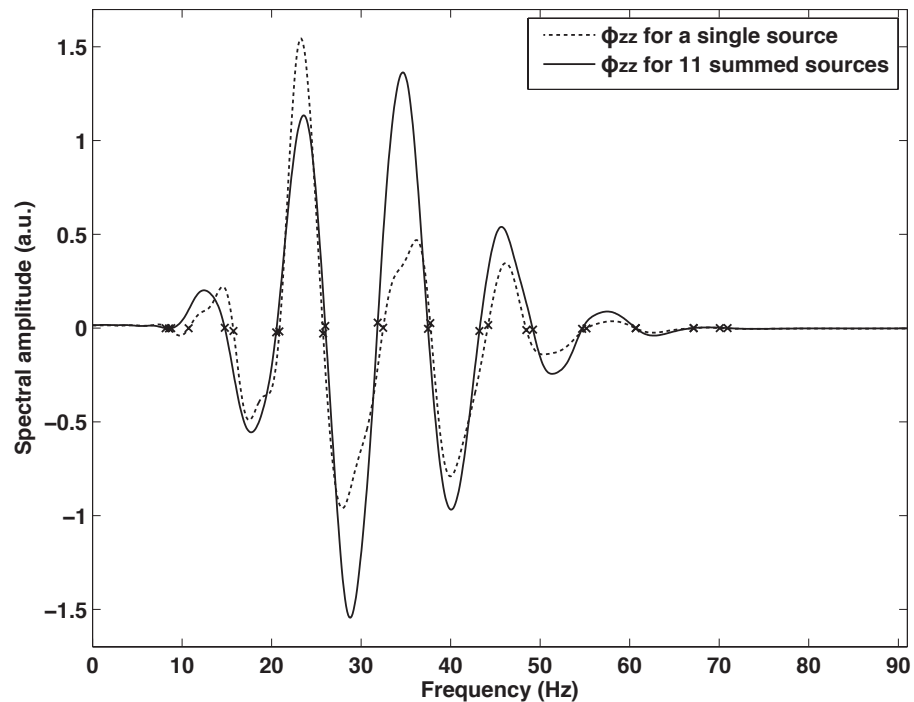


Figure 4.11: Cross-correlations of the vertical component of wavefields of receivers 20 and 40. Middle: The real part of the Fourier transform of the cross-correlation of the vertical components.

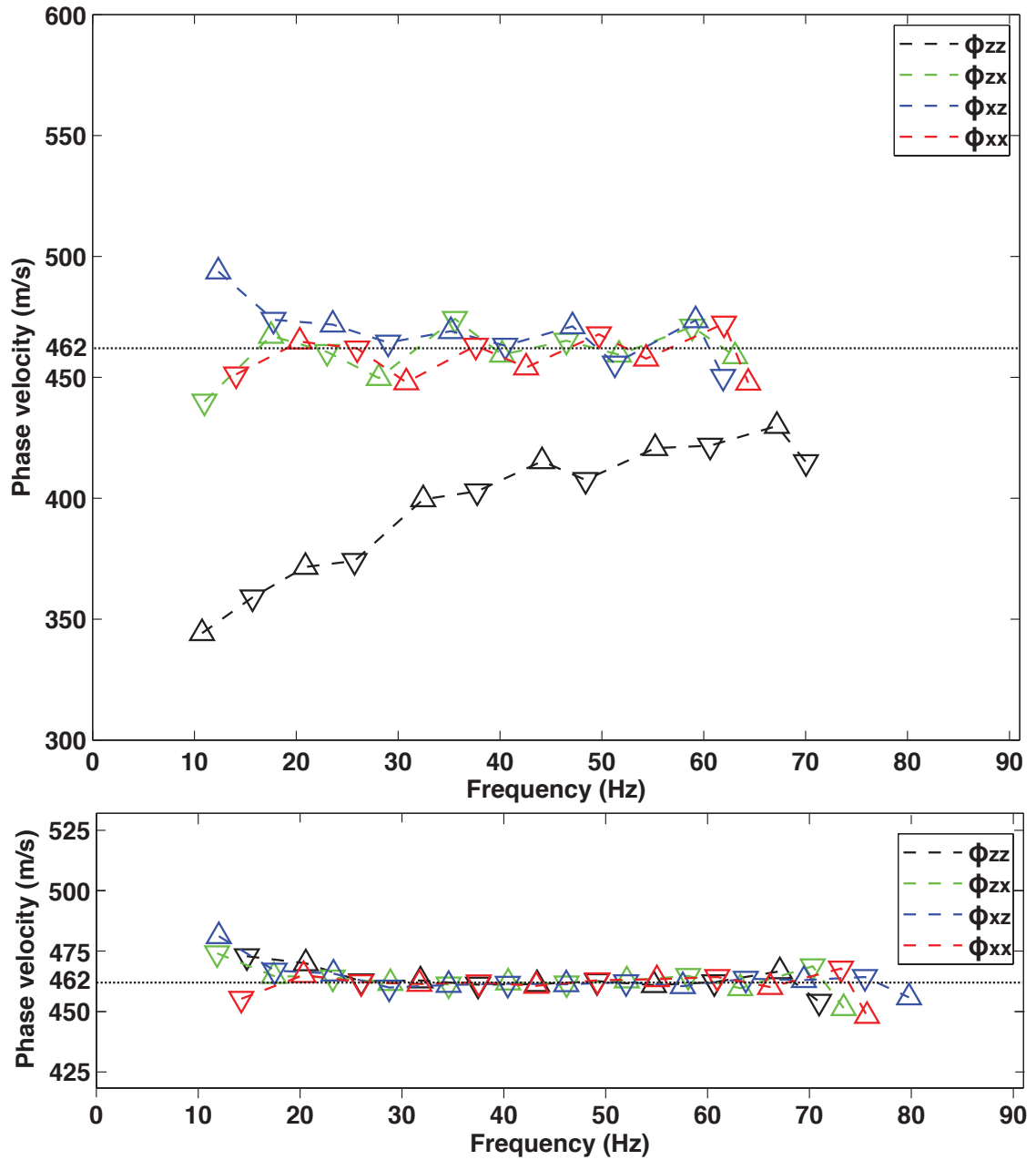


Figure 4.12: Zero crossings of the real part of the Fourier transform of the cross-correlations between receivers 20 and 40 for all four components for a single source (top) and the sum of 11 sources (bottom).

4.5.3 Discussion

Figure 4.8 shows that the surface wave is the most dominant event, whilst the weaker hyperbolic events can be attributed to both P- and S-wave primary and multiple reflections. The direct P-wave arrival is also evident with a faster move-out velocity of 900 m/s above the surface wave.

The dotted line in Figure 4.9 shows the Green's function $G_{zz}(20, 40, t)$. This is the result of cross-correlating the 0 and 40 m offset traces for a virtual shot gather located at receiver station 20. With no lateral change in velocity, these traces are identical to those shown at the 0 and 40 m offset distances in Figure 4.8. The main energy is associated with the Rayleigh wave, but correlations from the reflections and their multiples contaminate the retrieval of the Rayleigh-wave impulse response. Things improve when we sum cross-correlated wavefields from sources at different positions to the left of the 0 m offset receiver. The correlation between Rayleigh waves is stationary, but the correlated energy related to reflections comes in at varying times. This results in constructive interference of Rayleigh waves, and destructive interference of everything else. The solid line in Figure 4.9 is for the summed cross-correlation results using 11 shot records with a range of offsets to the first receiver of 0 to 100 m. The interval distance between shot points is 10 m. The same receiver pair is used in the summed and single shot cross-correlations. The summed shot cross-correlations, shown by the dashed line in Figure 4.9, has a more prominent spike than the single shot cross-correlation, which is likely due to the suppression of noise and non-linear moveout events. This suggests that the summing is more closely retrieving the Rayleigh-wave Green's function, removing artifacts caused by the reflections and their multiples.

Keeping the real part of the Fourier transform of $G(20, 40, t)$ for all four components gives the SPAC coefficients $\phi_{zz}(20, 40, f)$, $\phi_{zx}(20, 40, f)$, $\phi_{xz}(20, 40, f)$, and $\phi_{xx}(20, 40, f)$, shown in Figure 4.10. The diagonal coefficients ϕ_{zz} and ϕ_{xx} have the same phases and they follow a cosine function. The figure also shows how the cross-term coefficients ϕ_{zx} and ϕ_{xz} follow a sine function and are 180° out of phase with each other. The cross-term coefficients are $\pm 90^\circ$ out of phase with the diagonal-term coefficients. With the SPAC coefficients for each component having the same periods, their zero crossings have the same frequency intervals and both the cross-term and diagonal-term coefficients have coincident zero crossings.

Figure 4.11 shows a comparison of the $\phi_{zz}(20, 40, f)$ SPAC coefficients derived from the single and summed source cross-correlations. As in Figure 4.9, that shows the same comparison for $G_{zz}(20, 40, t)$, the comparison shows how summing of the sources reduces the variability in ϕ and its zero crossings. This variability is largely due to body wave contamination. Reducing its effect by summing shots will give a more robust estimate of phase velocity c . This is demonstrated by comparing the top and bottom panels of Figure 4.12 where the dispersion curves for all four SPAC coefficients are shown. The top panel shows the variability in phase velocity for all coefficients that are based upon cross-correlations from a single source. With the exception of the ϕ_{zz} SPAC coefficient, they are centered about a Rayleigh velocity of 462 m/s with an approximate variability of ± 15 m/s. ϕ_{zz} in the upper panel of Figure 4.12 has a lower phase velocity than the other three components because the single shot gather does not provide sufficient suppression of noise and body wave events. The bottom panel shows significantly less variability between dispersion curves due to the improvements gained by summing cross-correlations over 11 sources. It shows the phase velocity

converging closer to the true Rayleigh wave velocity in the slab of 462 m/s. These improvements include the removal of random noise and the suppression of non-linear moveout wavefield events such as reflected energy.

The first zero crossing closest to 0 Hz will be more susceptible to error as it is closest to the lower limits of the frequency band where the signal to noise ratio starts to fall off. It is therefore common practice that this first crossing is not used, as done by Ekström *et al.* (2009) and Tsai and Moschetti (2010). In cases where the cross-term SPAC coefficients that follow a sine function are almost full-band, it may be necessary to ignore the velocities calculated from the first two zero crossings. This is because the first crossing theoretically occurs at 0 Hz and depending on the selection of r , the subsequent crossings may be influenced by limitations in the available low frequency content of the data. The number of zero crossings to ignore will therefore be dependent upon the selection of r . A high value of r will cause a tighter crossing interval, and therefore an increase in zero crossings near the lower limits of frequency band. This may therefore result in more initial zero crossings being susceptible to weak signal to noise and needing to be ignored.

4.6 MuSPAC and Dispersion in a Simple Two Layered Model

4.6.1 Introduction and Experimental Setup

Here we apply the MuSPAC method to a two layered velocity model to explore the method's effectiveness at retrieving the velocities for each of the two layers in a dispersive medium. The two layer velocity model is shown in Figure 4.13. The

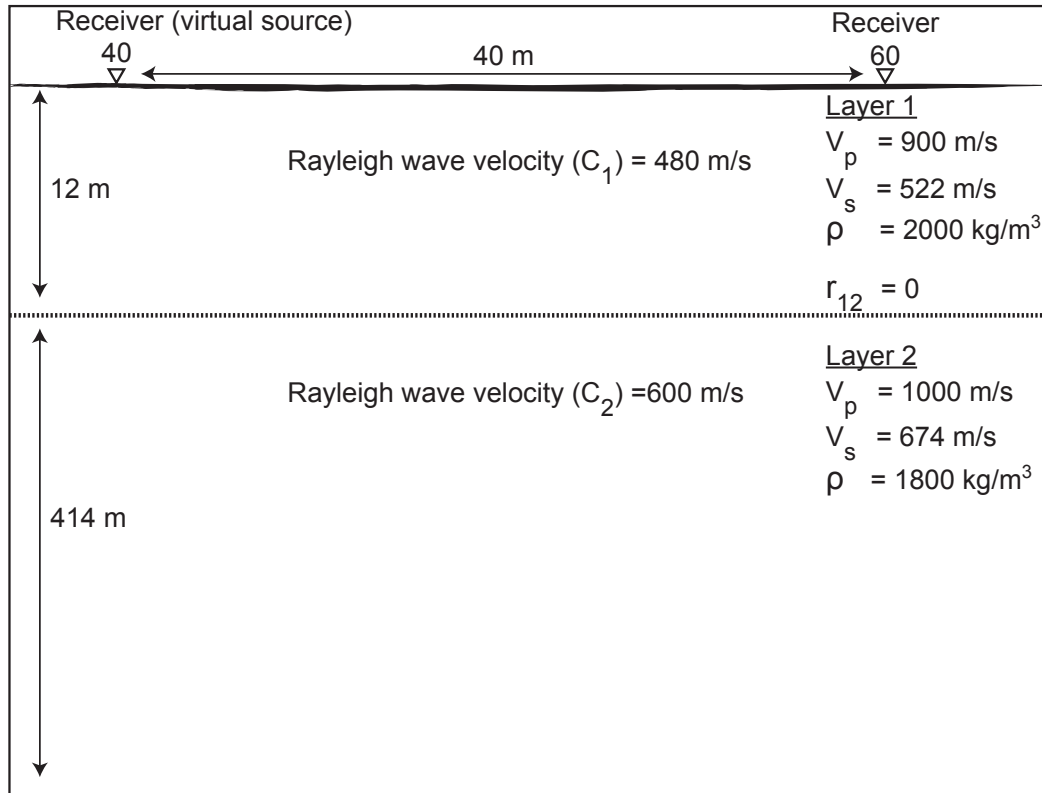


Figure 4.13: A schematic of the 2 layered model used to parameterized the SEM model.

velocity model in this figure is parameterized for use in the SEM forward code to generate 12 shot records with offsets to the first receiver ranging from 10 to 120 m. An interval spacing between shot points of 10 m is used. A Dirac source is used to give a full frequency band and the recorded signal is filtered using a low-pass 0-150 Hz filter. 60 receivers with 2 m spacing are used to record our signal with a sampling rate of 0.5 ms. Each set of shot gathers is correlated and summed to give the corresponding Green's functions for subsequent analysis in our MuSPAC method.

4.6.2 Results

In this section, we present a shot record and the results of our MuSPAC analysis for a virtual shot located at receiver 40 and the wavefield recorded on receiver 60. This gives a source-receiver separation distance of $r = 40$ m.

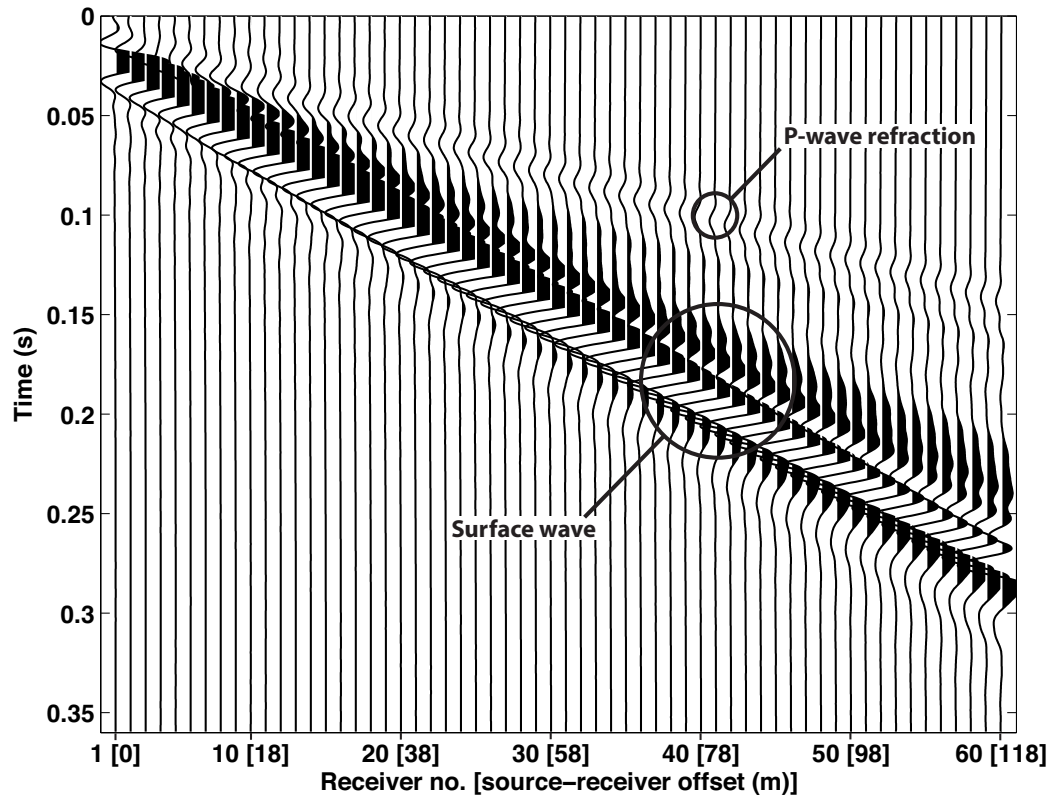


Figure 4.14: A synthetic shot record showing the radial component U_x for the two layered model.

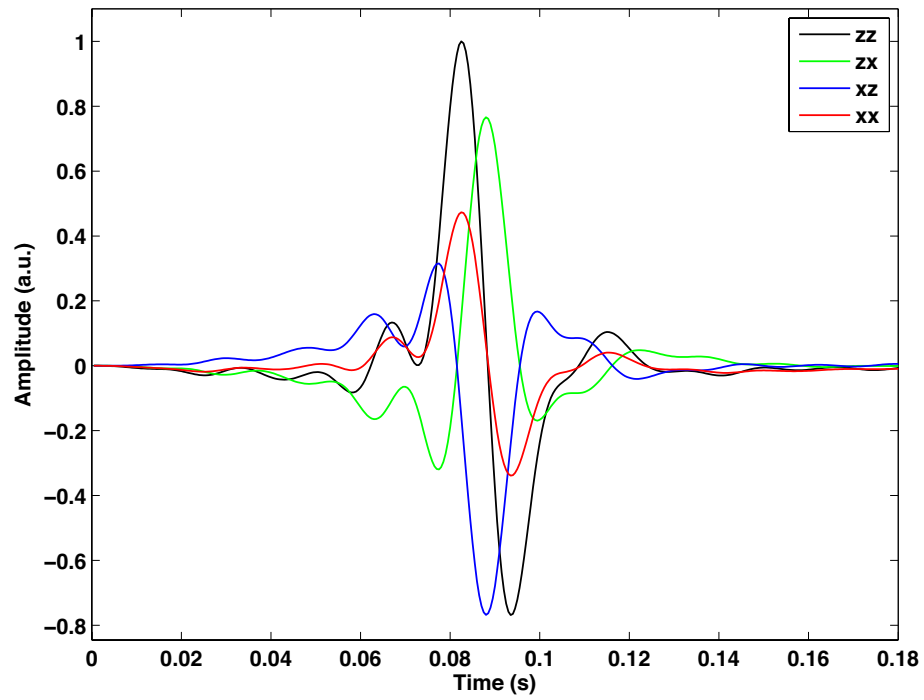


Figure 4.15: The Green's functions $G_{zz}(60, 40, t)$, $G_{zx}(60, 40, t)$, $G_{xz}(60, 40, t)$, and $G_{xx}(60, 40, t)$ found by cross-correlating the vertical and radial wavefield components for the two layered model.

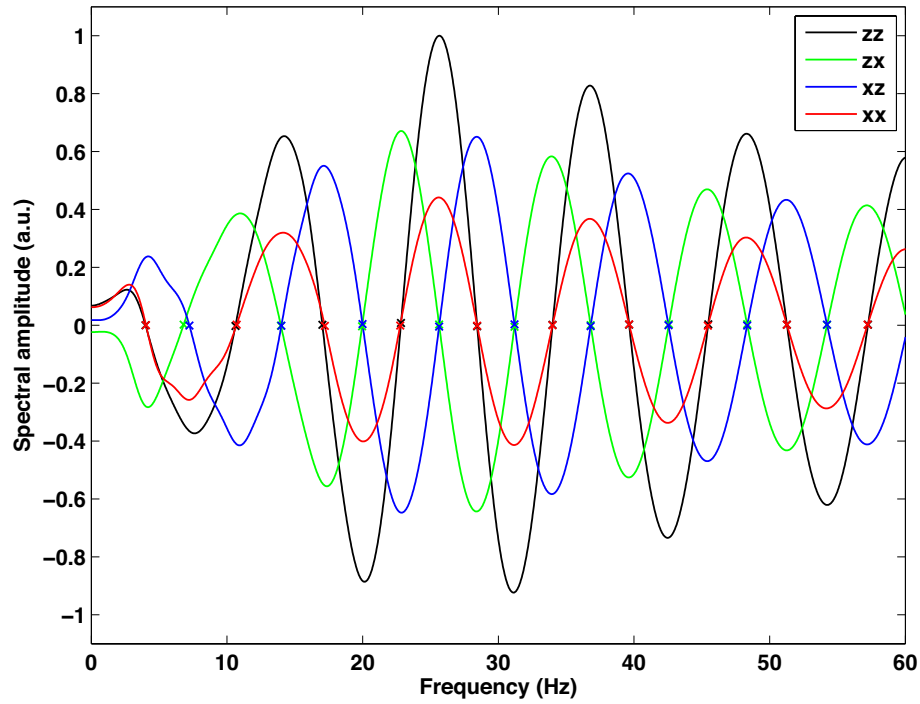


Figure 4.16: $\phi_{zz}(60, 40, f)$, $\phi_{zx}(60, 40, f)$, $\phi_{xz}(60, 40, f)$, and $\phi_{xx}(60, 40, f)$ for the two layered model.

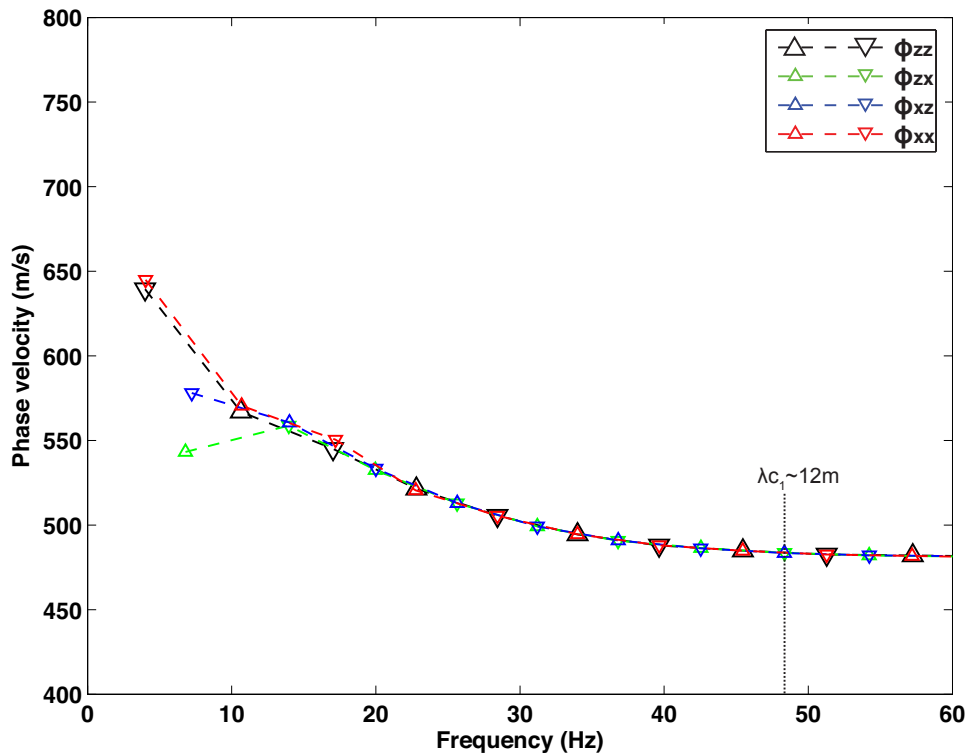


Figure 4.17: Phase velocity dispersion curves $c_{zz}(60, 40, f)$, $c_{zx}(60, 40, f)$, $c_{xz}(60, 40, f)$, and $c_{xx}(60, 40, f)$ for the two layered model. $\lambda_c \approx 12$ m represents one wavelength at 48 Hz and $c_1 = 480$ m/s. Waves below 48 Hz increasingly sample the faster velocity of layer 2 with decreasing frequency.

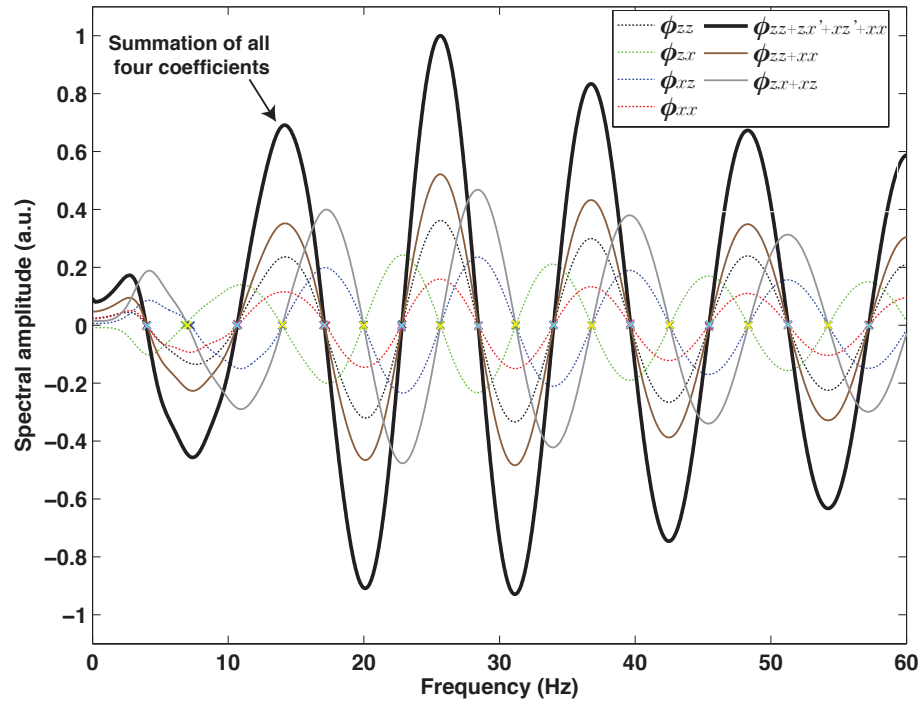


Figure 4.18: The solid line represents the average ϕ for all four coefficients. The primed $\phi_{zx'}$ and $\phi_{xz'}$ coefficients indicate that they have been rotated by -90 deg and 90 deg respectively to match the cosine function of the ϕ_{zz} and ϕ_{xx} coefficients.

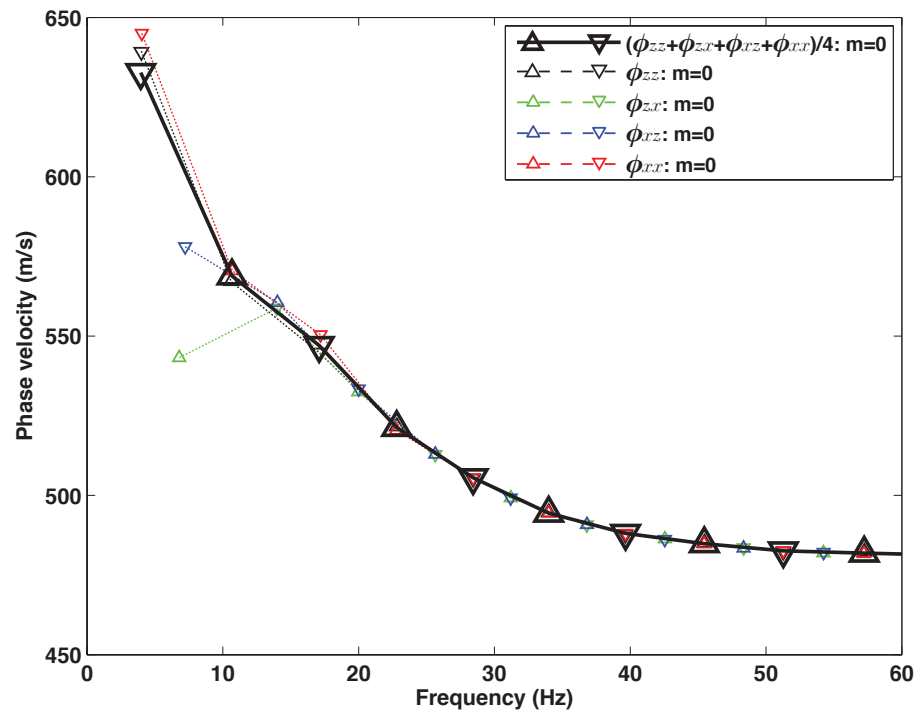


Figure 4.19: The solid black line shows the result of using the average ϕ to calculate phase velocity.

4.6.3 Discussion

Figure 4.14 shows the shot record being dominated by the surface wave. The surface wave exhibits dispersion with increasing offset. A low amplitude refraction can be observed above the surface wave and it extends to 0.15 seconds at receiver 60. This refraction with a linear moveout velocity of 900 m/s is the P-wave headwave refraction from layer 2. The other body wave events are not easily seen, because the surface wave amplitude is dominant.

Figures 4.15 and 4.16 show the Green's functions and SPAC coefficients for all four components. Both figures show similar results to the homogeneous and slab model results in Section 4.3. In Figure 4.16, $\phi_{xx}(60, 40, f)$ in the frequency interval 5 to 12 Hz shows an uneven signal as compared to $\phi_{zz}(60, 40, f)$. This may be a result of body wave contamination, which would occur at these lower frequencies where the faster portion of the dispersed Rayleigh wave is contained. It's unclear why the vertical component does not exhibit the same effect. It may be that the vertical component has a higher ratio of surface wave to body wave energy than the radial component, and this in turn helps mask out body wave contamination.

The dispersion curves in Figure 4.17 show the average phase velocity decreasing with increasing frequency from ~ 600 m/s to 480 m/s. The dispersion curves are more variable at the low frequencies because this is where the body waves contaminate the faster portions of the dispersed Rayleigh wave. The slower portion of the Rayleigh wave, that is predominantly sampled by the higher frequencies, is less variable between each of the components. This is because the faster body waves are not present at these slower velocities. λ_c in Figure 4.17 denotes the approximate frequency (48 Hz) where the one wavelength is ~ 12 m. This is where the Rayleigh wave is starting to

sample the faster 600 m/s velocity of layer 2 that lies at a depth of 12 m. Below 48 Hz, the Rayleigh wave increasingly samples the higher velocity (600 m/s) of layer 2 and this causes the dispersion curve to converge towards 600 m/s in the limit of $f = 0$ Hz.

In the cases when the method is applied to field data, summing ϕ_{zz} and ϕ_{xx} and ϕ_{xz} and ϕ_{zx} may improve zero crossing calculations by reducing instances where body wave contamination or low signal to noise cause additional zero crossings. It may even be advantageous to sum all four components by assuming the cross-coefficients are $\pm 90^\circ$ out of phase with the diagonal coefficients. The error introduced by this summation process, may be less than the error introduced due to additional zero crossings being calculated through body wave contamination or low signal to noise causing ϕ to cross zero. This is because the summation process assumes a straight line between SPAC coefficient zero crossings. It also causes the cross-coefficients to be translated along a straight line when the 90° phase rotation is applied. This rotation is applied for the purposes of aligning and summing all four SPAC coefficients.

Figure 4.18 demonstrates the effect of summing the two cross components, the two diagonal components, and all four components of the two layered model. Figure 4.19 shows a comparison between the individual dispersion curves for each coefficient versus the dispersion curve for the summed coefficients. The summing of ϕ has resulted in a dispersion curve that more closely retrieves the correct phase velocities.

4.7 MuSPAC and Body Wave Contamination in a Complex 31 Layer Model

4.7.1 Introduction and Experimental Setup

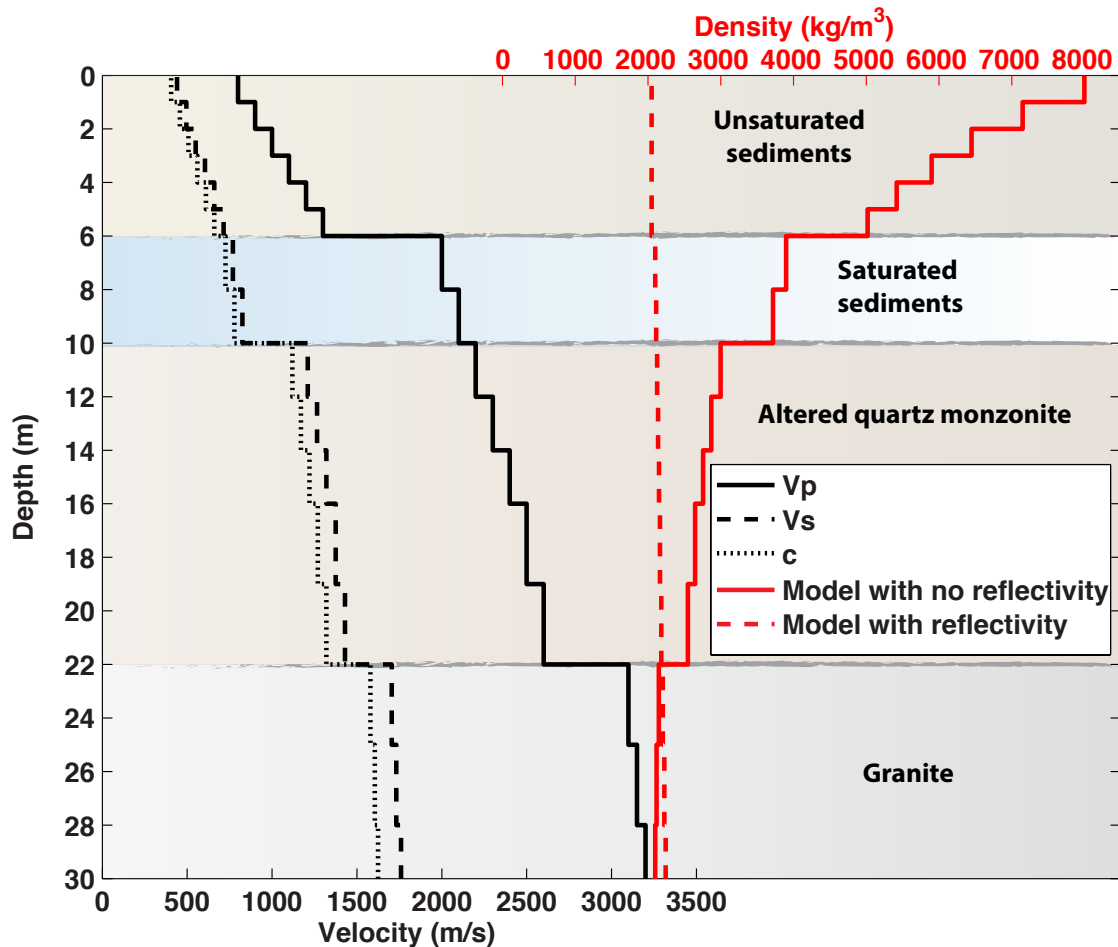


Figure 4.20: A schematic of the 31 layered model used to investigate how body waves effect our estimation of phase velocity. Two separate density profiles are used in the modeling and these are represented by dashed (increasing density with depth) and solid (decreasing density with depth) red lines.

Here we investigate the effects that body waves have on our estimation of phase

velocity by using a numerical 31 layer model with a full frequency band. The velocity model that we use is presented in Figure 4.20. There are 4 primary layers that characterize the model and these are intended to represent unsaturated, saturated, altered quartz monzonite, and granite layers. The dashed red line represents increasing density with depth and this, in conjunction with the increasing interval velocities, causes a reflectivity series between the layers. We refer to this parameterization with increasing density as the model with reflectivity. The solid red line represents decreasing density with depth and the densities have been chosen to cause no impedance contrast between the layers. We refer to this parameterization with decreasing density as the model with no reflectivity.

The reflectivity and no-reflectivity models are used in the SEM forward code to generate two sets of 21 shot gathers with offsets ranging from 10 to 110 m to the first receiver. A Dirac source is used to give a full frequency band and the recorded signal is filtered using a low-pass 0-150 Hz filter. 60 receivers with 2 m spacing are used to record our signal with a sampling rate of 0.5 ms. Each set of the 21 shot gathers is correlated and summed using equation 4.9 to give the corresponding Green's functions for subsequent analysis in our MuSPAC method.

4.7.2 Results

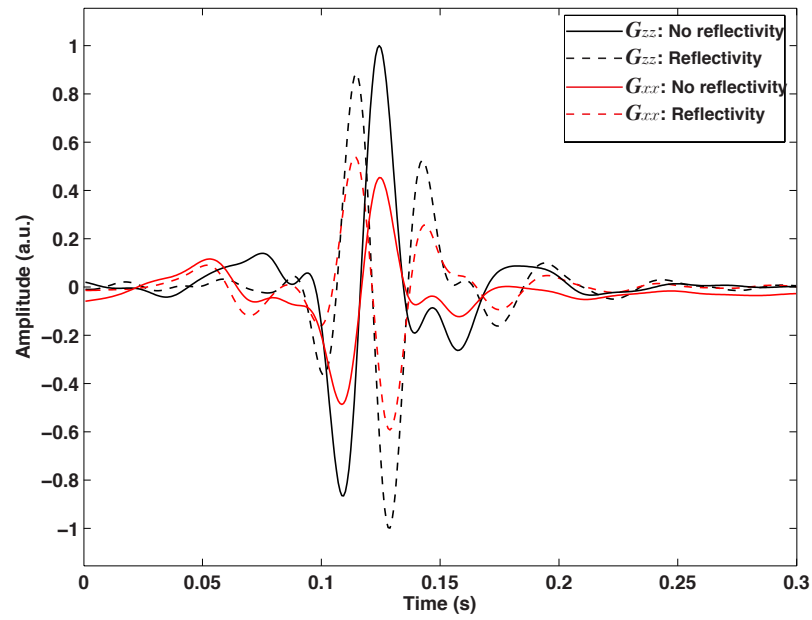


Figure 4.21: A comparison of the Green's functions $G_{zz}(s_{16}, s_1, t)$ and $G_{xx}(s_{16}, s_1, t)$ for the 31 layer models with and without reflectivity.

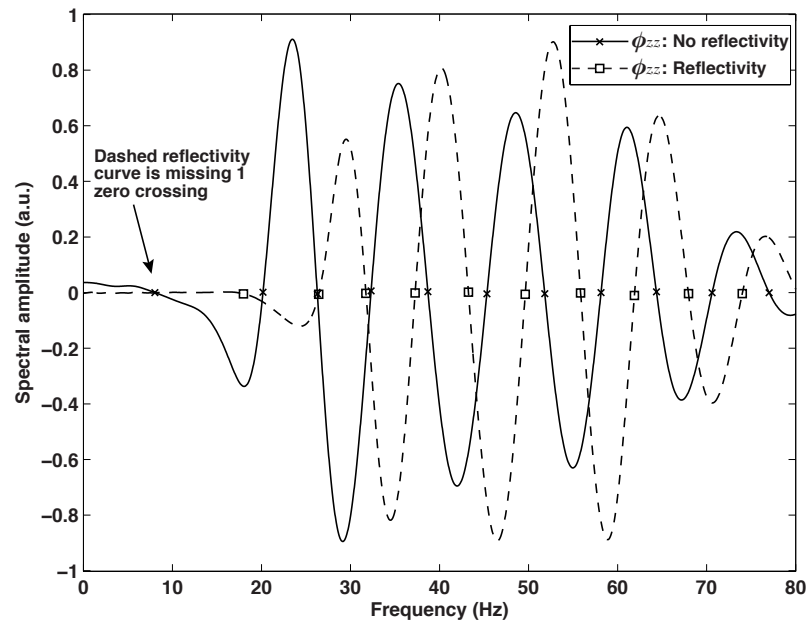


Figure 4.22: A comparison of SPAC coefficients $\phi_{zz}(s_{16}, s_1, f)$ for the 31 layer models with and without reflectivity.

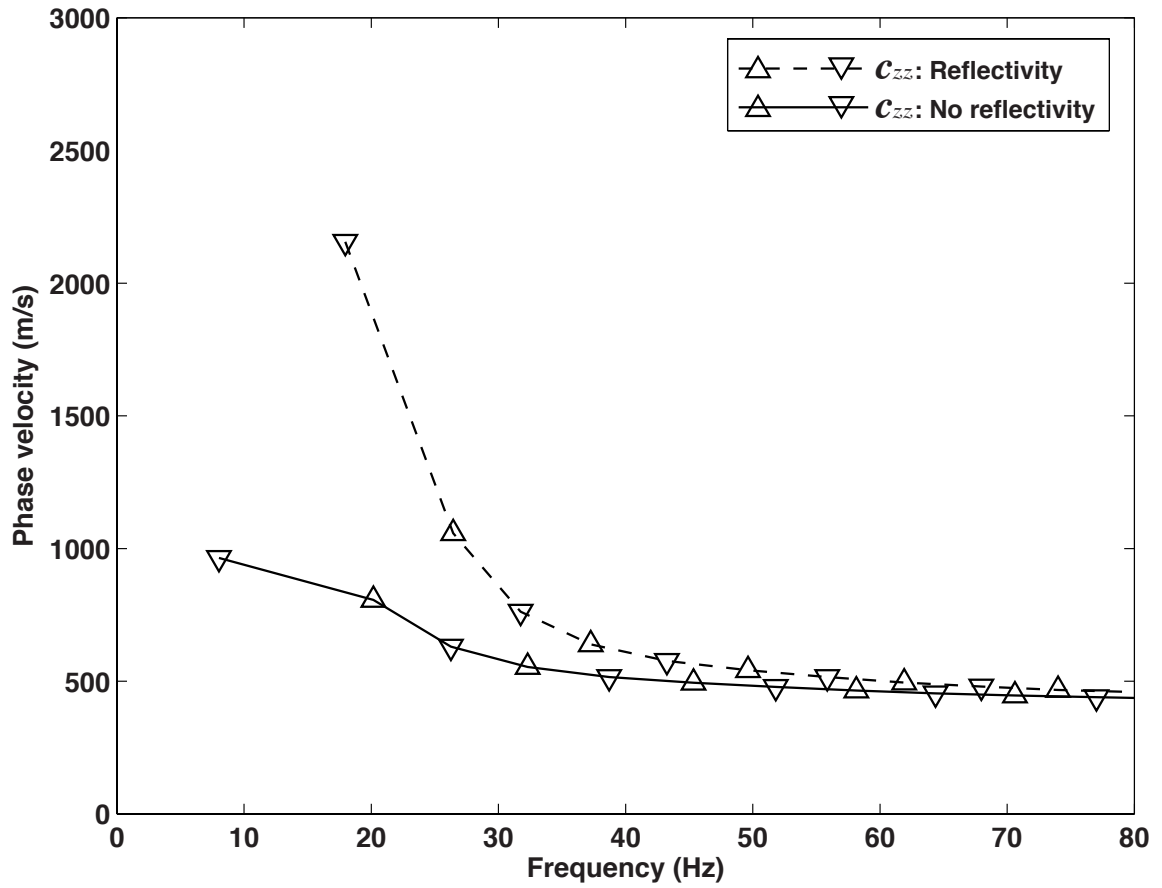


Figure 4.23: A comparison of phase velocities $c_{zz}(s_{16}, s_1, f)$ for the 31 layer models with and without reflectivity.

4.7.3 Discussion

Figure 4.21 shows how both $G_{zz}(s_{16}, s_1, t)$ and $G_{xx}(s_{16}, s_1, t)$ with no reflectivity have a more pronounced spiked impulse response between 0.1 and 0.13 seconds than the Green's functions with reflectivity. In both cases, this central impulse response is primarily related to the strong surface wave event. In the case of the reflectivity model, the surface wavefield is broadened and contaminated by waves trapped between layers that are multiply reflected until their energy is either transmitted out or attenuated. This contamination and therefore change in the Green's function for the model with reflectivity will cause a change in the zero crossings of ϕ and ultimately the estimated phase velocity dispersion curve.

As expected from the difference in Green's functions, Figure 4.22 shows the $\phi_{zz}(s_{16}, s_1, f)$ with reflectivity to be shifted to the right of the $\phi_{zz}(s_{16}, s_1, f)$ without reflectivity. This shift is evident by comparing the frequencies of the respective zero crossings and the shift between corresponding zero crossings becomes less with increasing frequency. This will result in the phase velocities converging at higher frequencies and this can be observed in Figure 4.23 where the phase velocities have converged by about 80 Hz. The reason for the reflectivity causing elevated velocities at the lower frequencies is because the reflectivity in the shallow layers (0-40 m) traps the high frequency waves and allows a greater proportion of the lower frequency waves to pass through. This trapping of higher frequency body waves has the effect of contaminating the Green's function with early multiples that cause the MuSPAC method to over-estimate the phase velocities. This can be remedied by muting out the early wave modes, however this can also mute out the lower frequencies of the Rayleigh wave that, in the case of this 31 layer model, can be expected to have ve-

locities that exceed 2000 m/s below 10 Hz. Muting out the lower frequencies of the Rayleigh wave would thus cause us to possibly miss zero crossings, so care must be taken when applying a top mute. The best approach may be to use a time and space variant band-pass filter that is applied to the region above the dominant surface wave. This band-pass filter could be designed to pass the lower frequencies expected in the Rayleigh wave and cut out the higher frequencies of the multiply reflected body waves.

4.8 MuSPAC and Partial-Band Data in a Complex 32 Layered Model

4.8.1 Introduction and Experimental Setup

Here we use a 32 layer numerical model to investigate how we can retrieve the correct phase velocity dispersion curve in partial-band data. We do this by comparing the MuSPAC results of full-band and partial-band data and explore how muting out body wave contamination impacts our phase velocity estimates. The 32 layer model is parameterized to represent the field case presented in the later Section 4.9. This was done through some back and forth iterations with our field data results until we found a good fit between the numerical and field based shot gathers and dispersion curves. By matching the results of this 32 layer model with our field shot gathers and background analyses, the MuSPAC results therefore give us a good estimate of how many zero crossings are missed in our partial-band field data of Section 4.9.

The 32 layer model we use is presented in Figure 4.24. There are 4 primary layers that characterize the model and these are intended to represent the field case covered in the next section of this chapter. The velocities in this 32 layer model are used in

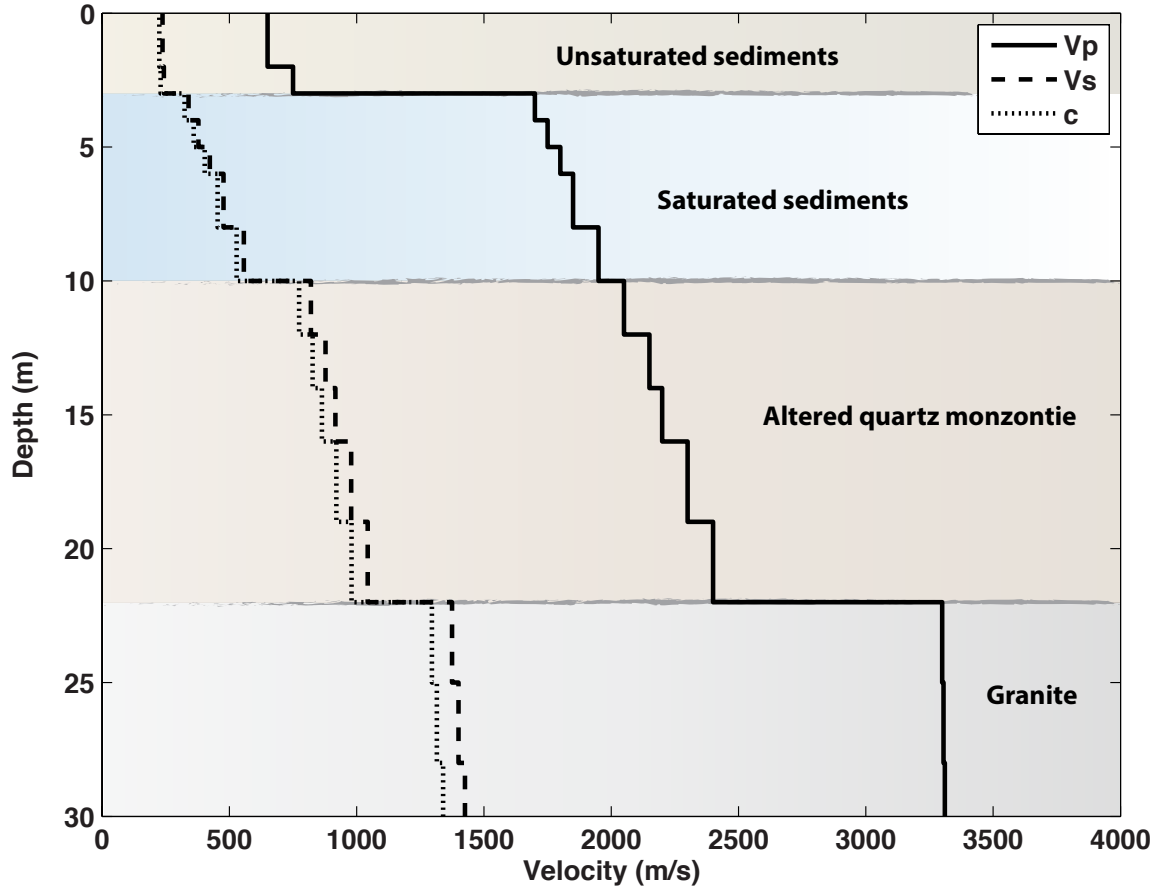


Figure 4.24: A schematic of the 32 layered model showing the P-wave (V_p) and S-wave (V_s) velocity profiles used to parameterized the SEM model. The corresponding Rayleigh wave velocity c is also shown and is based upon equations from White (1983).

the SEM forward code to generate 21 shot gathers with offsets ranging from 10 to 110 m to the first receiver. A Dirac source is used to give a full frequency band and the recorded signal is filtered using a low-pass 0-150 Hz filter. 60 receivers with 2 m spacing are used to record our signal with a sampling rate of 0.5 ms. Each set of shot gathers is correlated and summed to give the corresponding Green's functions for subsequent analysis in our MuSPAC method. We mimic the partial-band case by applying a high-pass filter on the shot gathers that removes frequencies below 30 Hz.

4.8.2 Results and Discussion of Synthetic Shot Records

Figures 4.25 and 4.26 show the low-pass filtered (0-150 Hz) 10 m offset shot gathers, U_z and U_x , for the vertical and radial components, respectively. The dominant surface wave train has a linear moveout velocity of about 225 m/s from 0.06 to 0.58 seconds. Shear wave reflections from the altered quartz monzonite layer can be seen beneath the surface wave train. As offset increases, these reflections converge with the surface wave train due to their similar velocities and the slightly longer path lengths of the multiply reflected shear wave events. The surface wave dispersion caused by the higher velocities of the altered quartz monzonite and granite layers is masked by the multiple P-wave and S-wave events above the surface wave train. These events are a combination of reflections, refractions, converted waves, and their corresponding multiples. The U_z shot gather in Figure 4.25 shows the faster refractions from the altered quartz monzonite and granite layers arriving at about 0.4 to 0.6 seconds at the far offsets. In this example, these refractions have a relatively low amplitude as compared to the surface wave train.

Figures 4.27 and 4.28 show the vertical and radial component shot gathers at receiver station 2. As expected, they have retained the linear events such as the dispersion wave train and refraction events. This linear events also originate at $t = 0$ seconds at zero offset. The reflections will have stacked in at stationary phase points although these are not readily observable largely due to the relative dominance of the surface wave energy.

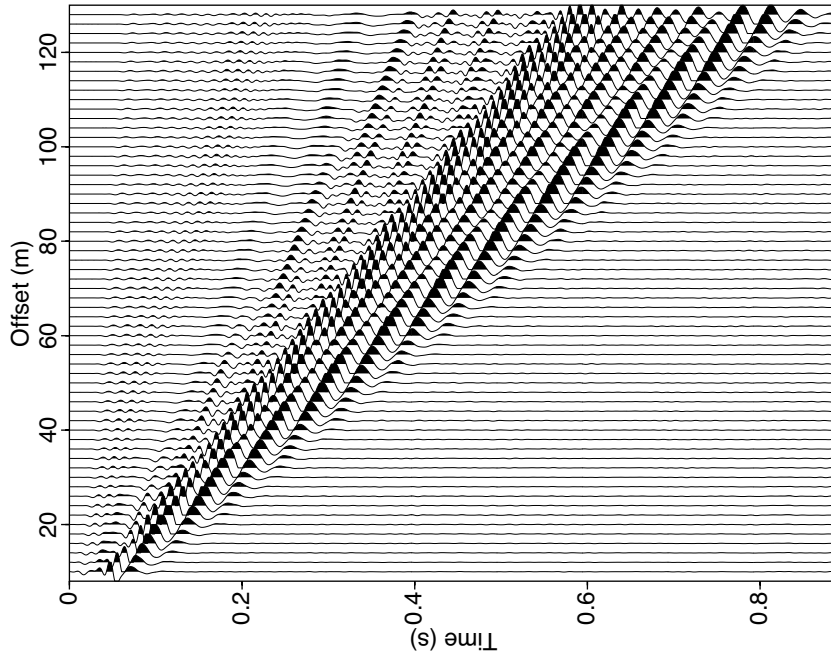


Figure 4.25: U_z for the 32 layer model with an offset of 10 m to the first receiver. A Dirac source was used and a bandpass filter from 1 to 90 Hz was applied. Receiver separation is 2 m.

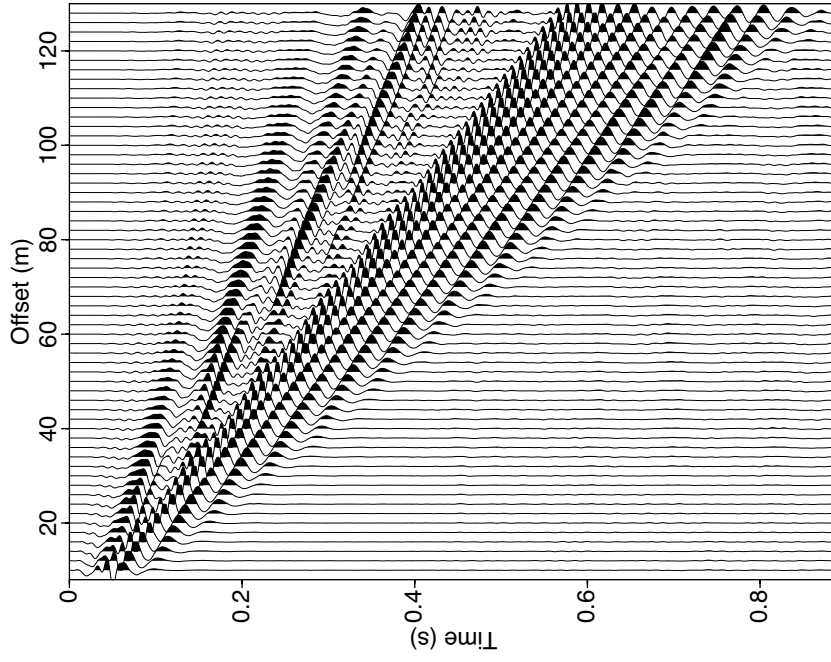


Figure 4.26: U_x for the 32 layer model with an offset of 10 m to the first receiver. A Dirac source was used and a bandpass filter from 1 to 90 Hz was applied. Receiver separation is 2 m.

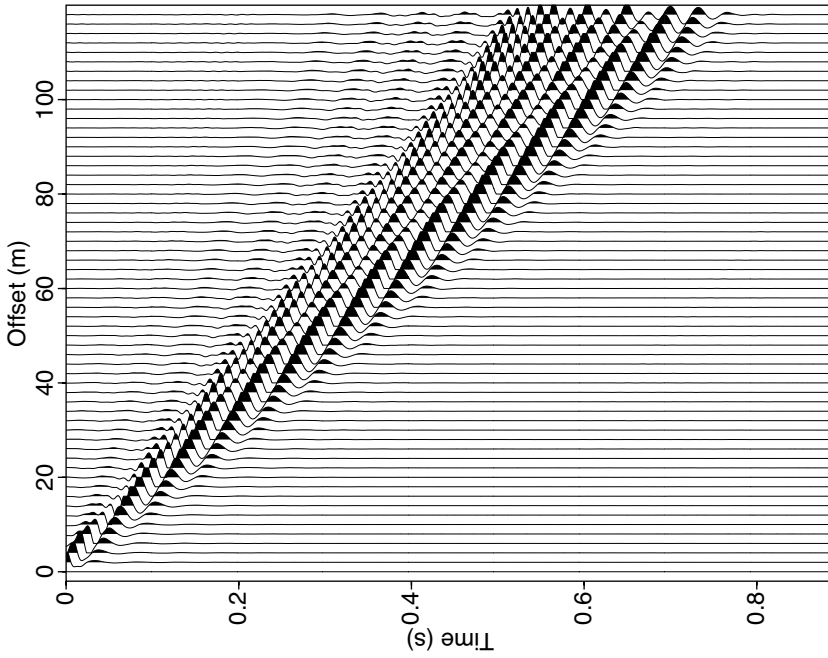


Figure 4.27: A numerical virtual shot gather of $G_{zz}(r, s_2, t)$ for the 32 layer model. A Dirac source was used and a bandpass filter from 1 to 90 Hz was applied. The virtual shot position is at receiver 2 and is created by summing together the cross-correlations between 23 real shots. The real shots are located to the left of the first receiver and have an offset range of 58 to 10 m with interval spacings ranging from 2 to 4 m.

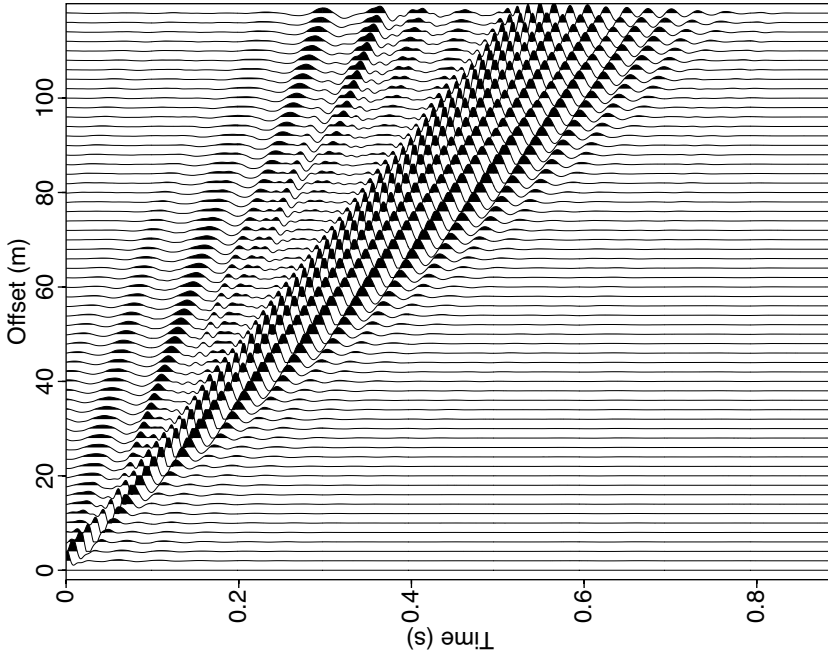


Figure 4.28: A numerical virtual shot gather of $G_{xx}(r, s_2, t)$ for the 32 layer model. The shot position is at receiver 2 and is created by summing together the cross-correlations between 23 real shots. The real shots are located to the left of the first receiver and have an offset range of 58 to 10 m with interval spacings ranging from 2 to 4 m.

4.8.3 Results and Discussion for MuSPAC and Full-Band Data

Here we take the receiver pair 1 and 15 that recorded data generated by the full-band Dirac source and calculate the phase velocity dispersion curve using the MuSPAC method. With receiver offsets of 2 m, this gives a separation of $r = 28 \text{ m}$ for these two receivers.

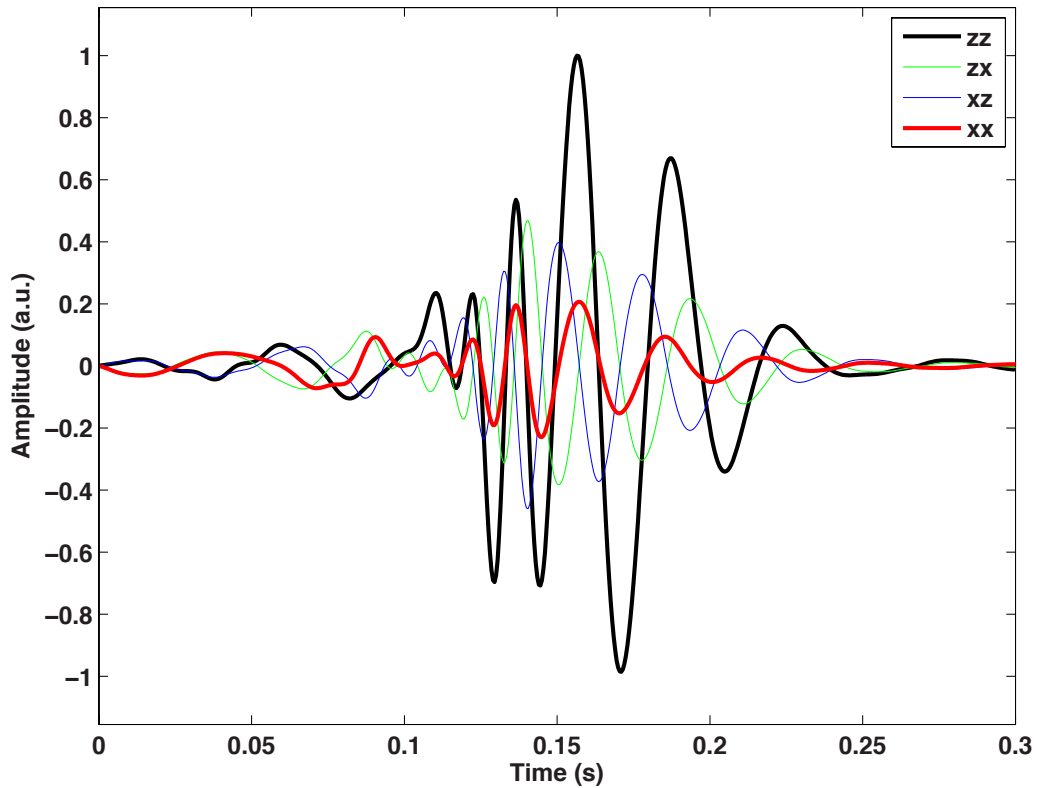


Figure 4.29: Full-band Green's functions $G(s_{16}, s_2, t)$ for the 32 layer model. The Green's functions were created using the virtual shot gathers and summing over all receiver pairs that have $r = 28 \text{ m}$.

With our 32 layer model having no lateral variation in velocity, we reduce the numerical noise of the Dirac source by summing all cross-correlated receiver pairs

with a separation of $r = 28 \text{ m}$. The resulting full-band Green's function, that has been muted with a cosine taper to subdue early arriving events before time 0.1 s, is presented in Figure 4.29. The 90 degrees phase shift between the $G_{xx}(s_{15}, s_1, t)$, $G_{zz}(s_{15}, s_1, t)$ and their cross-terms can be observed at 0.15 s where the surface wave train is dominant.

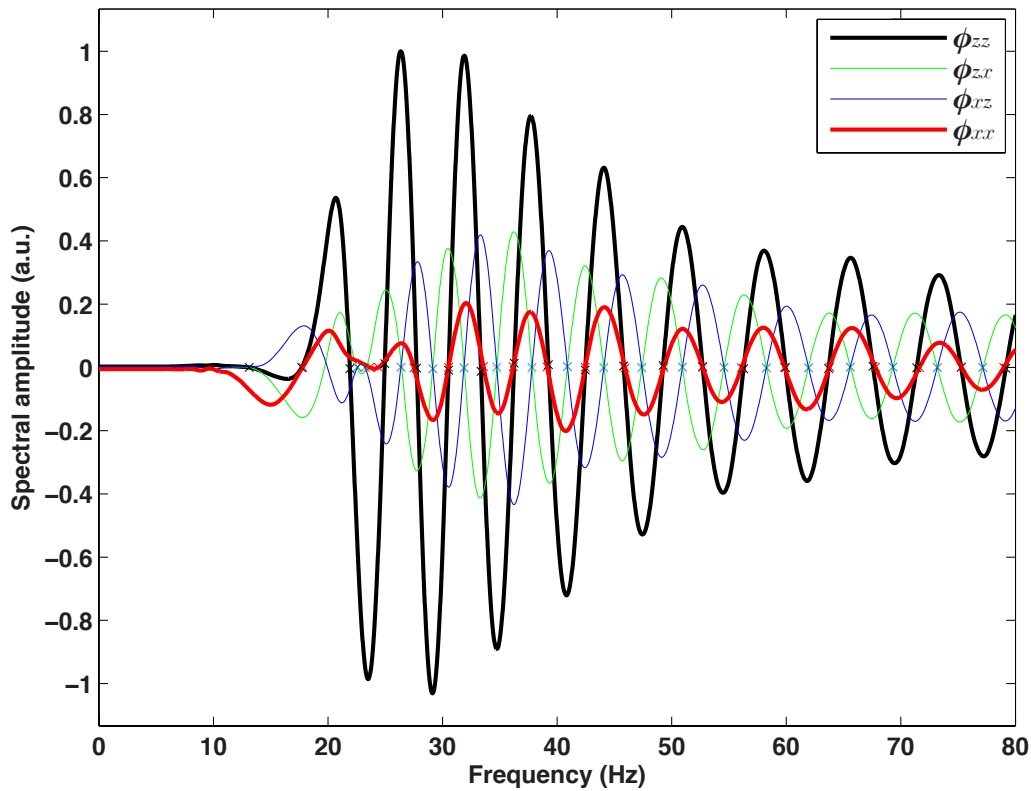


Figure 4.30: Full-band SPAC coefficients $\phi(s_{15}, s_1, f)$ for the 32 layer model with $r = 28 \text{ m}$.

Figure 4.30 shows the SPAC coefficients for the full-band case using $\phi(s_{15}, s_1, f)$. The $\phi_{xx}(s_{15}, s_1, f)$ coefficient in Figure 4.30 appears to have been influenced by a non-surface wave based event at around 24 Hz with a related affect on the cross-terms $\phi_{zx}(s_{15}, s_1, f)$ and $\phi_{xz}(s_{15}, s_1, f)$. This has resulted in the two cross-terms having an

extra zero crossing in the 22 to 25 Hz interval thereby causing a subsequent over-estimation of the phase velocity by these components at 22 to 25 Hz. This over-estimation of velocity can be seen in Figure 4.31 where the velocities of $c_{xz}(s_{15}, s_1, f)$ and $c_{zx}(s_{15}, s_1, f)$ are elevated above the diagonal terms at around 22 to 25 Hz. This is an example of how all four components can be used to identify such sources of error through dissimilarities between the four components.

Figure 4.31 shows the phase velocity estimated for the full-band 32 layer model. The full-band $c_{zz}(s_{15}, s_1, f)$ dispersion curve with $m = 0$ converges to $c = 225 \text{ m/s}$ at 80 Hz, which is the correct Rayleigh wave velocity as the unsaturated layer is 3 m deep and was parameterized to give a Rayleigh wave velocity of $c = 225 \text{ m/s}$. The Rayleigh wave velocity in the 32 layer model is $\sim 1400 \text{ m/s}$ by depth 25 m and increases linearly to $c \sim 2000 \text{ m/s}$ by depth 100 m. This would suggest that the first crossing of the full-band $c_{zz}(s_{15}, s_1, f)$ dispersion curve with $m = 0$ is over-estimated at 15 Hz due to body wave contamination. This is supported by our 31 layer model reflectivity versus no reflectivity comparison in Section 4.7, where we found the phase velocities for the low frequency crossings in the model with reflectivity to be significantly higher than the model with no reflectivity.

4.8.4 Results and Discussion for MuSPAC and Partial-Band Data

Here we take the receiver pair 1 and 15 that recorded data generated by the partial-band Dirac source and calculate the phase velocity dispersion curve using the MuSPAC method. As in the full-band case, the separation between the chosen receivers is $r = 28 \text{ m}$ and we have muted events in the Green's functions using a cosine taper

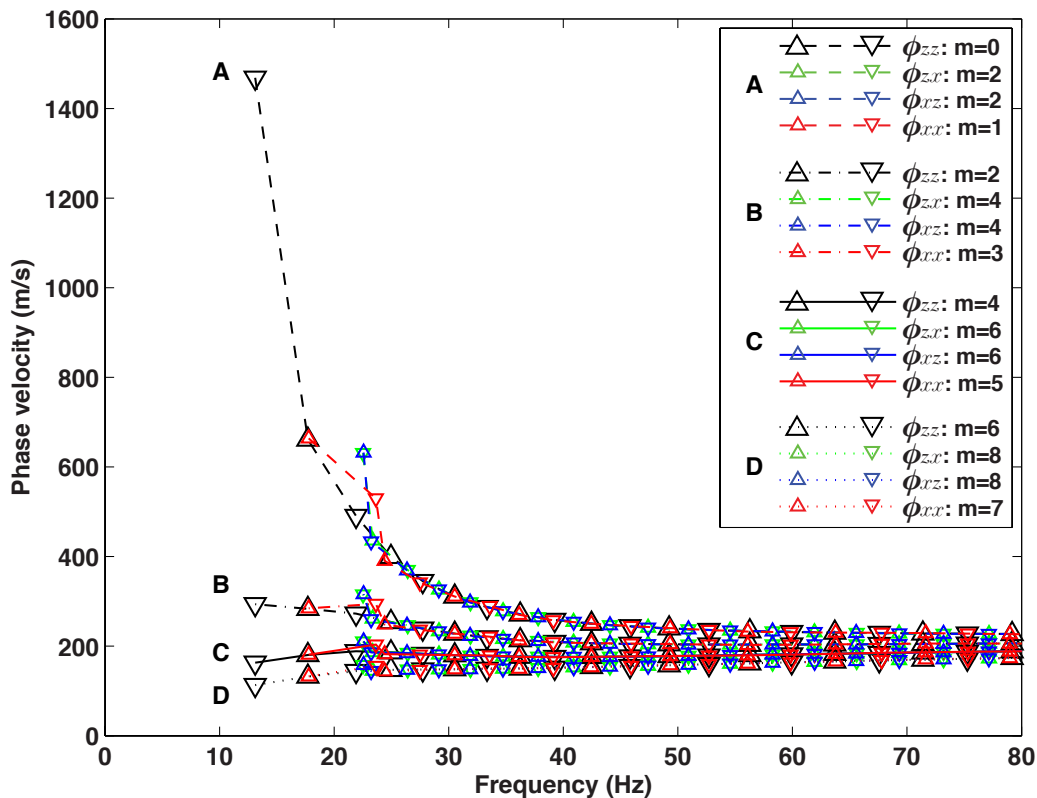


Figure 4.31: Full-band phase velocity dispersion curves $c(s_{15}, s_1, f)$ for the 32 layer model with $r = 28 m$. The curves show the effect of adding zero crossings in intervals of 2. The differences in m between components is related to the requirement that the first crossing direction must follow either a cosine or sine function as demonstrated by the homogeneous half-space examples.

before 0.1 s.

The cross-correlations were performed using the same procedure described for the full-band case with the only difference being that the data has had a high-pass filter of 30-150 Hz applied to it. The resulting partial-band Green's functions for all components are presented in Figure 4.32. Figure 4.33 shows a direct comparison between the full-band and partial-band for just the $G_{xx}(s_{15}, s_1, t)$ functions. Both of these figures show the partial-band case has less amplitude at the earlier times to the

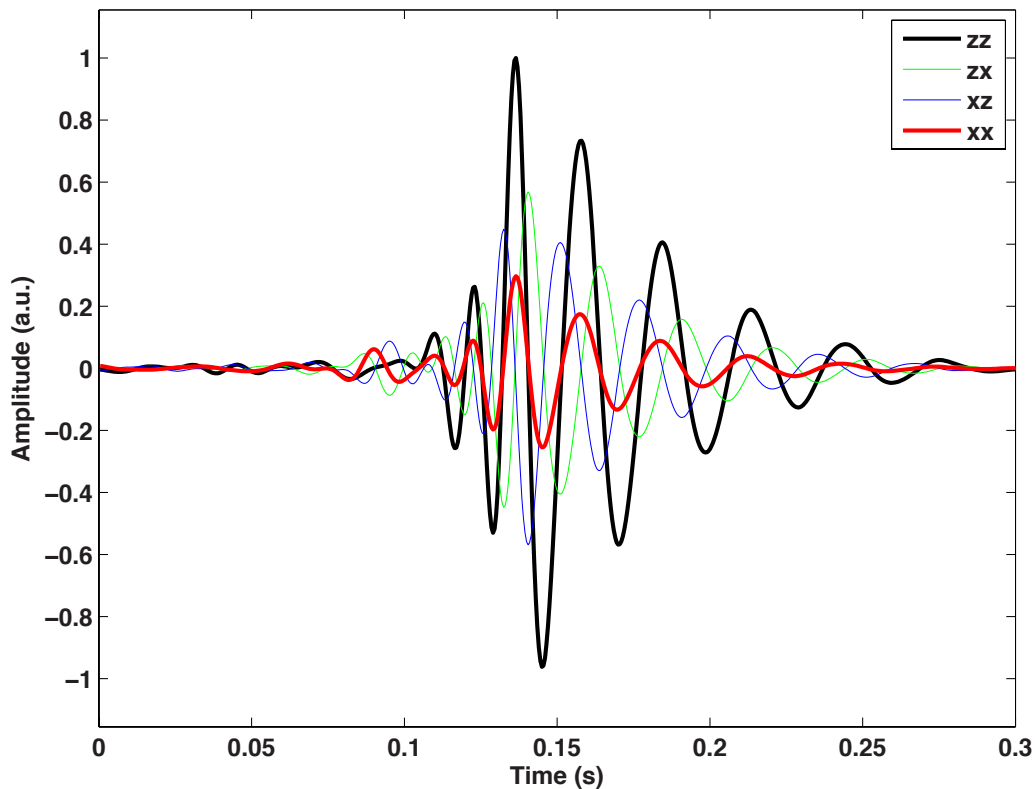


Figure 4.32: Partial-band Green's functions $G(s_{15}, s_1, t)$ for the 32 layer model. The Green's functions were created using the virtual shot gathers and summing over all receiver pairs that have $r = 28 m$.

right of the central peak ($t = 0.14 s$). This suggests that the frequencies below 30 Hz contained information about the faster Rayleigh wave velocities that is missing in the partial-band example.

The corresponding partial-band $\phi(s_{15}, s_1, f)$ coefficients in Figure 4.34 no longer show the disruption to the $\phi_{zx}(s_{15}, s_1, f)$ and $\phi_{xz}(s_{15}, s_1, f)$ zero-crossings as the frequencies where this occurred in the full-band case have been removed. Figure 4.34 shows a direct comparison between the full-band and partial-band for just the $\phi_{xx}(s_{15}, s_1, t)$ coefficients. This Figure 4.34 shows the similarity between the full-band and partial-

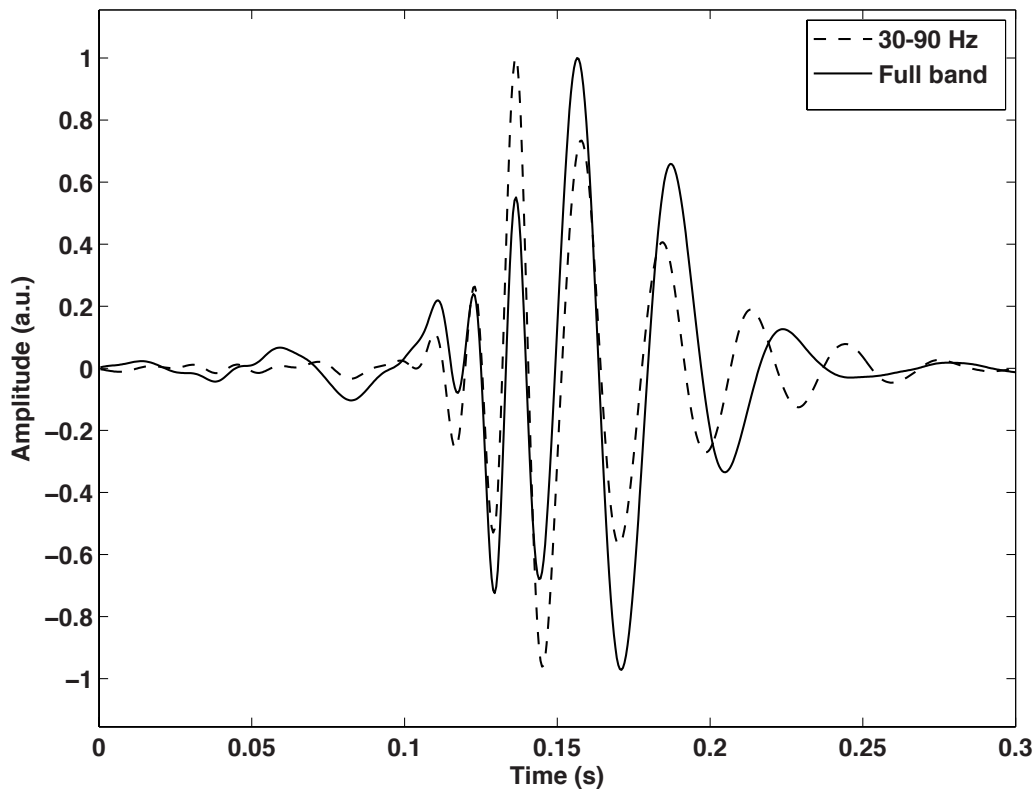


Figure 4.33: A comparison of the full-band and partial-band Green's functions $G_{xx}(s_{15}, s_1, t)$ for the 32 layer model.

band zero-crossings for the partial-band frequency range of 30 to 80 Hz.

The removal of the disrupted $\phi_{zx}(s_{15}, s_1, f)$ and $\phi_{xz}(s_{15}, s_1, f)$ zero-crossings below 30 Hz has resulted in the dispersion curves having less variability amongst components, as shown in Figure 4.36. This figure also shows that a value of $m_{zz} = 5$ is needed to match the partial-band curves to the full-band curve.

To summarize this section, Figure 4.37 shows the dispersion curves for the partial-band case superimposed with the full-band $c_{zz}(s_{15}, s_1, f)$ dispersion curve. This demonstrates that our phase velocity estimates over our available frequency band is not impacted by a partial-band source. The only complication is try to estimate

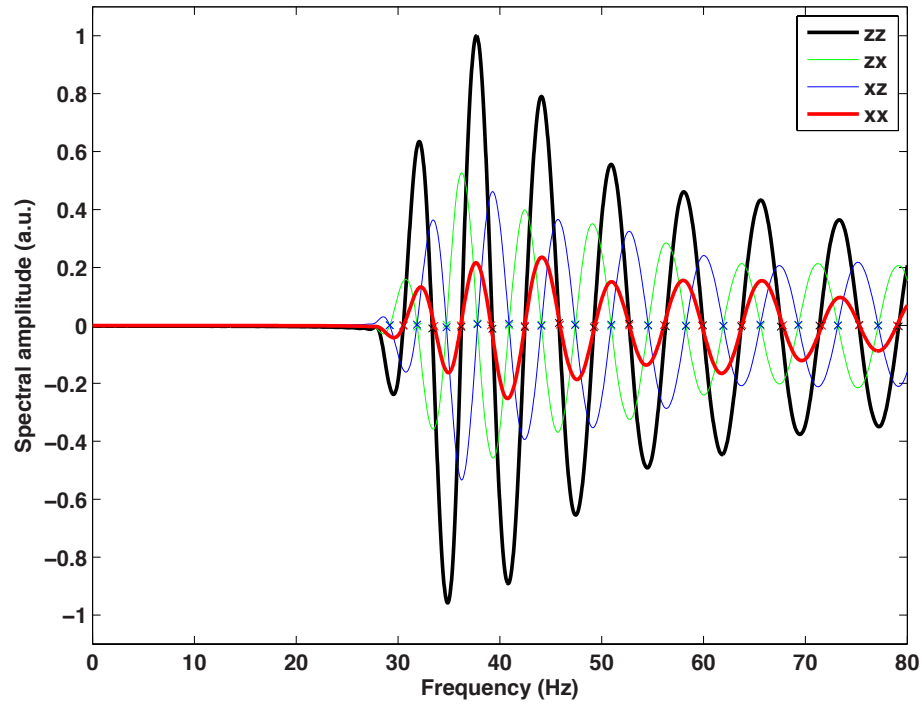


Figure 4.34: Partial-band SPAC coefficients $\phi(s_{15}, s_1, f)$ for the 32 layer model where only frequencies of 29 Hz and up are band passed.

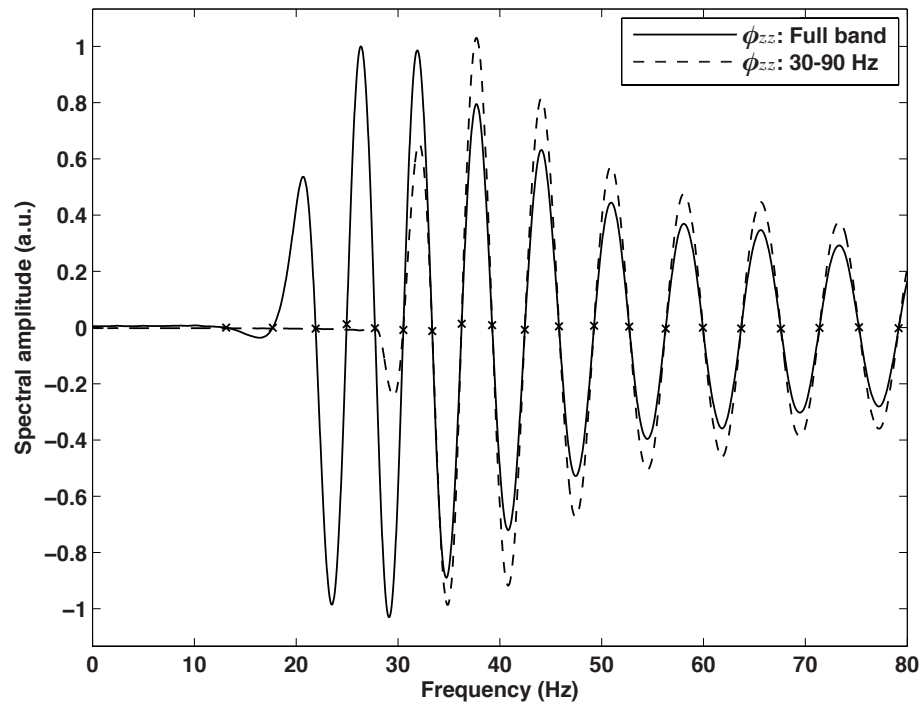


Figure 4.35: A comparison of the full-band and partial-band SPAC coefficients $\phi_{xx}(s_{15}, s_1, f)$ for the 32 layer model.

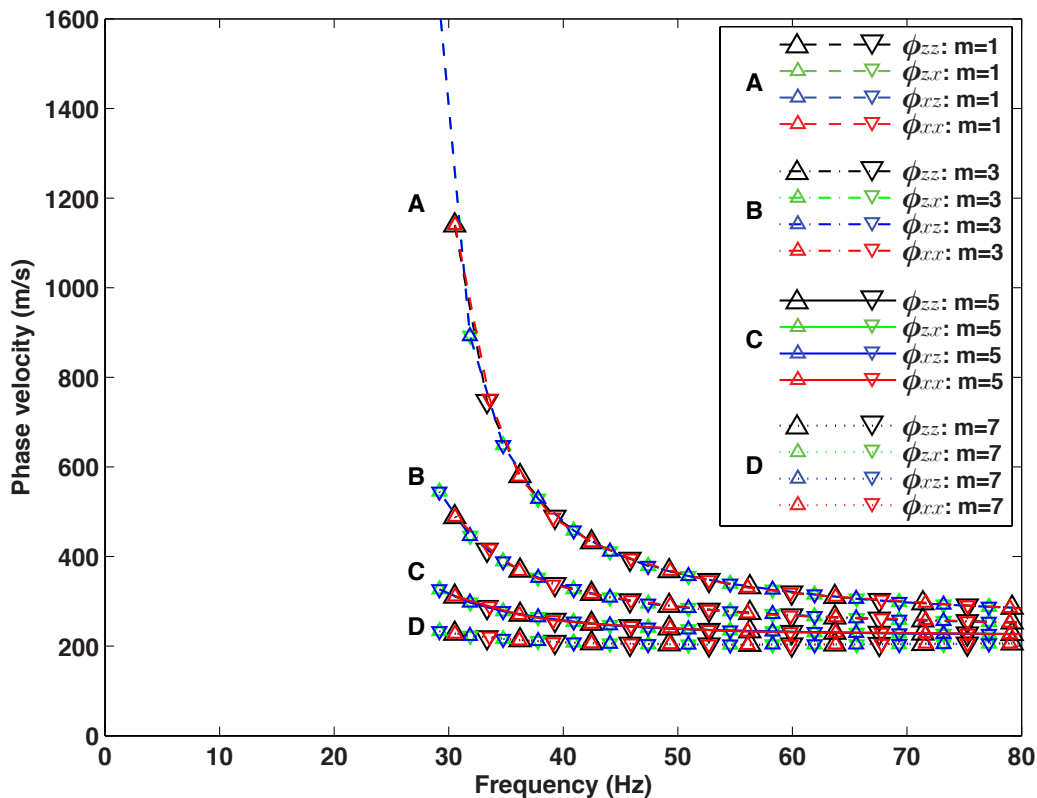


Figure 4.36: Partial-band phase velocity dispersion curves $c(s_{15}, s_1, f)$ for the 32 layer model where only frequencies of 29 Hz and up are band passed. The curves show the effect of adding zero crossings in intervals of 2.

how many zero crossings were missed. This must be achieved by having an understanding of the maximum and minimum Rayleigh wave velocity bounds and looking at the variation in dispersion curves through adjusting m . This will prove more difficult with increasing receiver separation as greater r will cause more phase changes between receivers. This in turn makes estimating the number of missed crossings more difficult in the absence of having lower frequency sources. It is therefore apparent, that to use this method to its maximum potential, that one should strive to use the lowest source frequency available and choose the upper source frequency limit to

match the minimum depth resolution that is required.

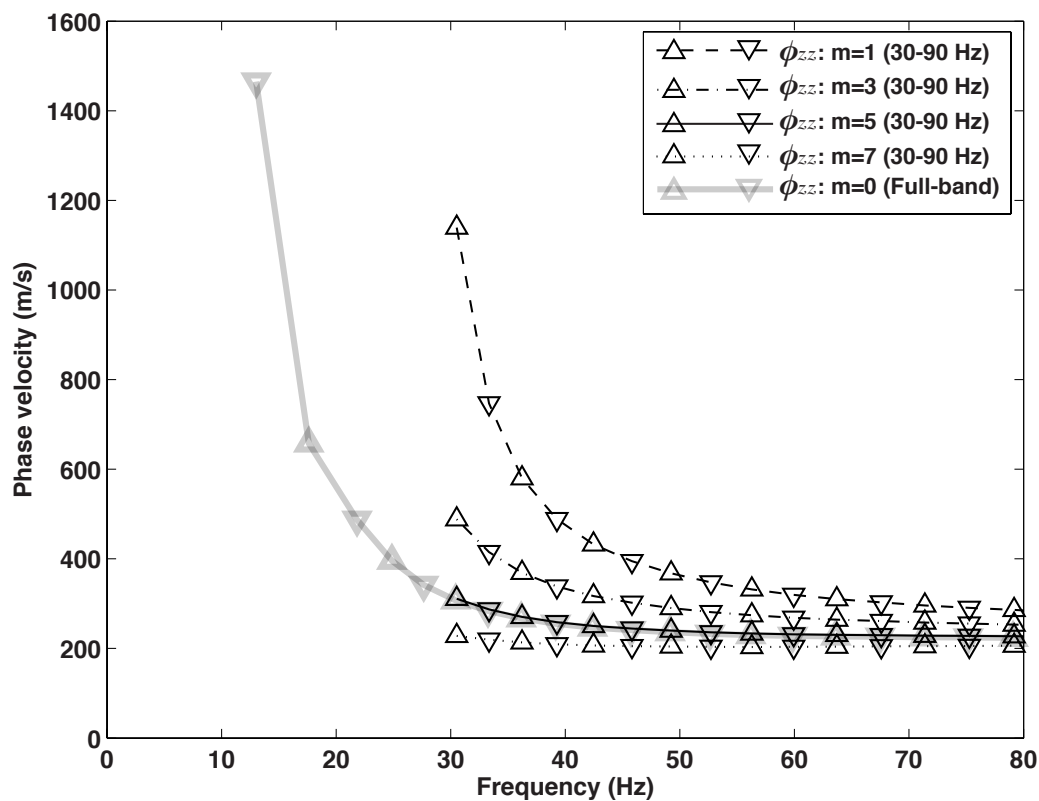


Figure 4.37: A comparison of the full-band and partial-band dispersion curves using the $c_{zz}(s_{15}, s_1, f)$ curve. This shows that five missed zero crossings must be added to the partial-band curves in order to retrieve the correct phase velocities.

4.9 Deadhorse Lake Field Site

4.9.1 Introduction

In this section, we introduce the Deadhorse lake (DHL) study site shown in Figure 1.1. The DHL study site is located in Chalk Creek Valley, which extends eastwards into the Upper Arkansas Basin in central Colorado. The site is approximately 1.2 km southwest of the FOP (Longs field) study site and is located within the Chalk Creek accommodation zone. The site coincides with a north-south aligned boundary between hot and cold water wells to the west and east, respectively. The site is characterized by 10 to 50 m deep glacial, fluvial, and alluvial deposits overlying a quartz monzonite, and granite basement rock. Despite its name, Deadhorse lake is a dry lake for most of the year.

At this site, we acquired and processed a series of geophysical data with the goal of imaging the subsurface and trying to find sub-surface structures that are possible geothermal pathways. The processed results of these data are presented in Section 4.9.2 and our interpretations of them are discussed in Section 4.9.3. We then use a subset of these data to apply our MuSPAC method in and our findings are presented in Sections 4.9.4 through 4.9.6. The goal of the MuSPAC analyses is to assess the methods effectiveness with application to field data and to further enhance to our interpretation of the subsurface.

The extent of our data collection throughout the DHL site is shown in Figure 4.38. We conducted a gravity survey across a portion of the site and the results of this survey are displayed in the figure. The gravity data were acquired using a Scintrex CG-5 gravimeter on a 50 m grid. The gravity data have had drift, latitude, free-air,

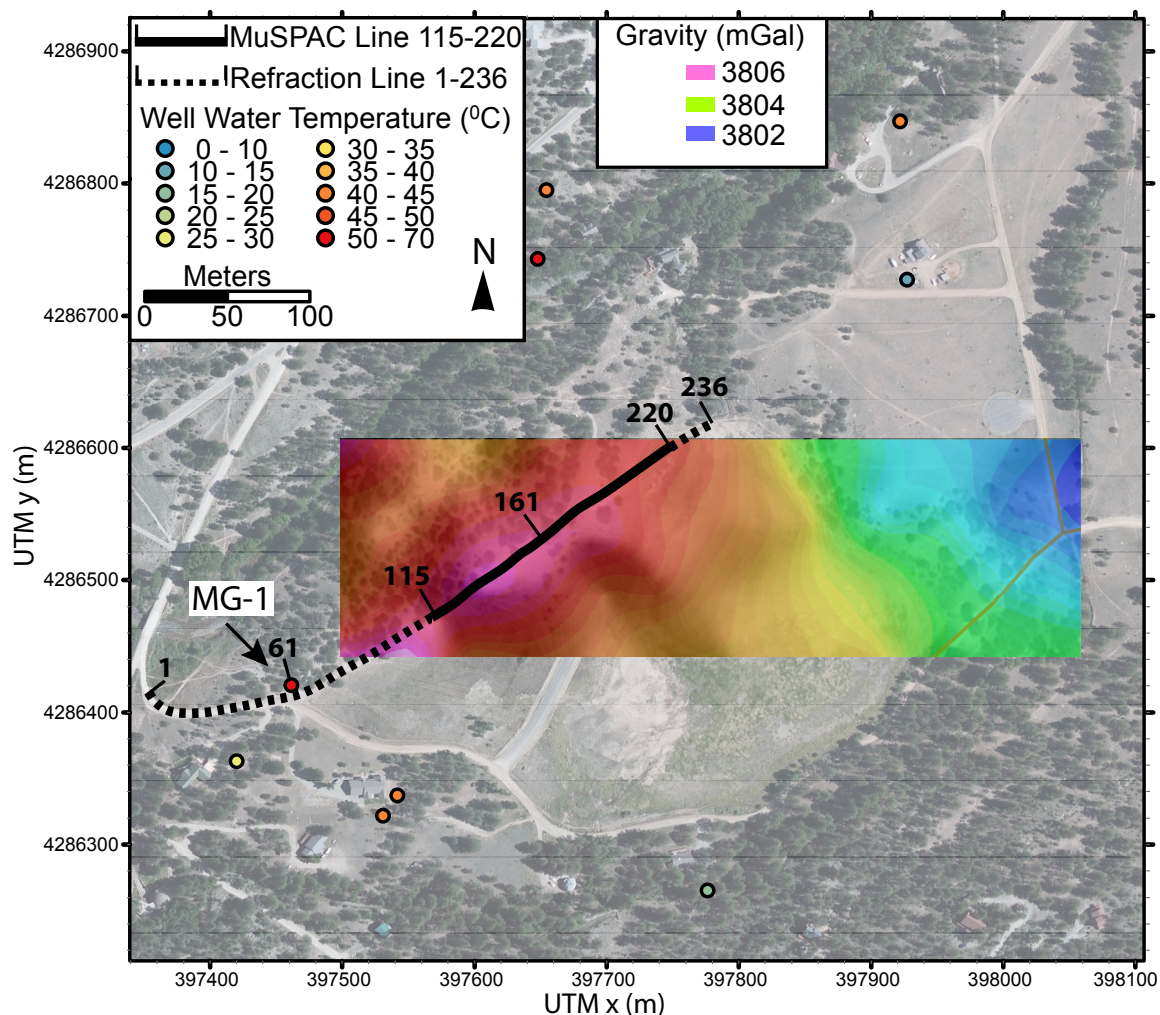


Figure 4.38: The DHL study site showing water wells and their temperatures, the location of the seismic lines, and overlaid with the results of a gravity survey we acquired.

Bouguer, and terrain corrections applied. The gravity data are interpreted to have an eastward dip in the underlying bedrock with a difference of approximately 4 mGal across the 600 m wide survey area.

We conducted a vertical seismic profile (VSP) survey in the 168 m deep MG-1 borehole and these results are presented below. We acquired an active seismic data

set along a dirt track shown traversing Figure 4.38 in an east-northeasterly direction. This line is represented by the coincident dashed and solid lines that extend from station 1 to 236. The station interval along this line is 2 m, thus giving a total line length of 472 m. A refraction tomography analysis was performed on a vertical component seismic data acquired along the 472 m line. An active 9 component seismic data set was acquired between stations 115 and 236. We used the station interval of 115 and 220, represented by the solid black line, to apply our MuSPAC method. The results of this are presented in Section 4.9.5.

4.9.2 Results: Background Data

VSP and Well-Logs

The VSP gather in Figure 4.39 shows the processed results of our VSP survey along with our interpretations of these data. The interpretations in this figure are discussed in Section 4.9.3.

Multi-Component Seismic Survey

All the multi-component shot records presented in this section are for a shot position of 161 shown in Figure 4.38. An additional 46 shots offset in 2 m intervals from stations 161 to 115 were used during the Green's function correlation process giving a total maximum offset of 92 m between shot points. These shots were always recorded on the same 60 receivers from stations 161 to 220 giving a total receiver offset of 118 m.

The multi-component seismic data were acquired using a 2720 kg Industrial Vehicles T-15000 vibroseis source. The vibroseis data were recorded using a 120 channel

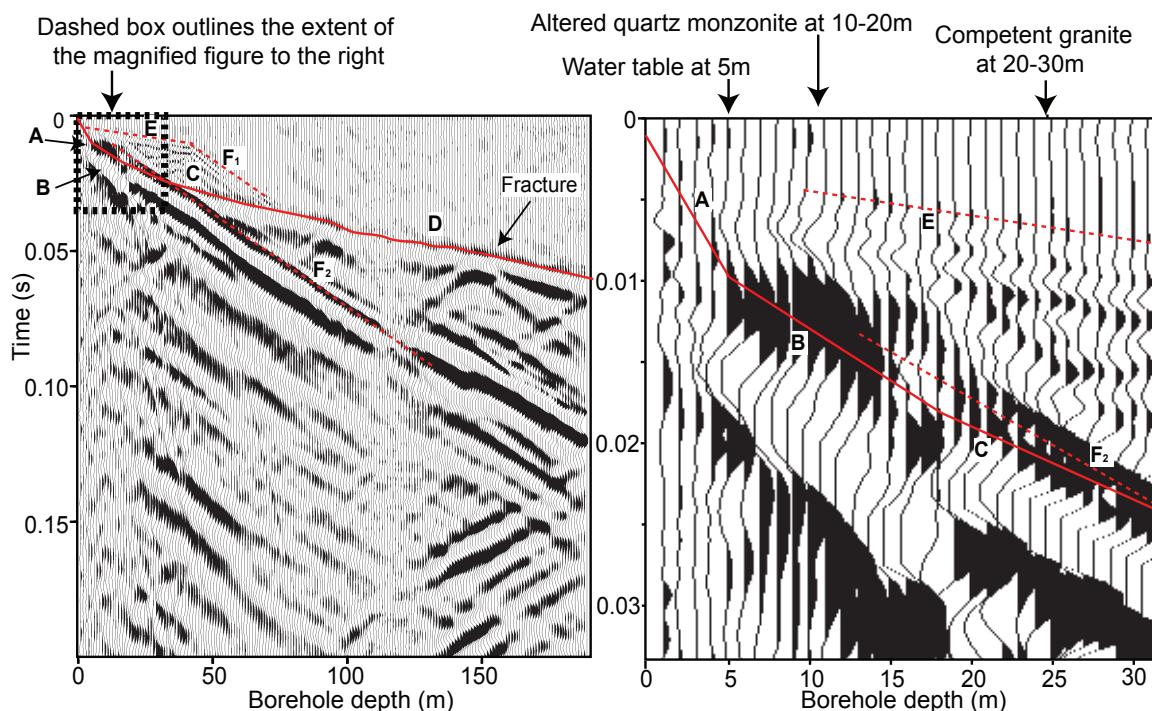


Figure 4.39: Left panel: Vertical seismic profile at MG-1 using a zero offset sledge hammer source and a hydrophone string with 1 m receiver spacings. Right panel: A zoomed in portion of the left panel, designated by the dashed box, that highlights the difficulty of interpreting the near-surface wavefields due to interference from waves related to the steel well casing and water. The letters are associated to dominant wavefield events that we interpret as: A, unsaturated sediments with $V_p=600$ m/s; B, saturated sediments with $V_p=1800$ m/s; C, altered quartz monzonite with $V_p=2400-3600$ m/s; D, granite with $V_p=3600-4400$ m/s; E, borehole steel casing with $V_p=5500$ m/s; F1, water wave radiating from the steel casing with $V_p=1433$ m/s; F2, water wave originating from the top of the well with $V_p=1433$ m/s.

recording system and a 0.5 ms sample rate. The sweeps were linear and extended from 30 to 300 Hz over a 14 second period. The total record time was 16 seconds. The vertical and radial phones were separate units and have a resonant frequency of 10 Hz. With only having 120 channels available to record, each of the nine source and receiver components were recorded as separate events. In some cases, this introduced some spatial error, as replanting receivers and revisiting the same shot points for each

iteration was done by planting station flags adjacent to the line. The approximate variation in this repositioning is estimated to be on the order of 0.5 m. The receivers were not surveyed for each iteration and instead the station flags were surveyed once using a Trimble survey grade instrument with a roving base station. The entire field survey was conducted over a 10 day period.

All the shot gathers presented in this section are derived from vibroseis data that were correlated using a synthetic trace. This is purely to facilitate a discussion about our interpretations of the dominant the wavefield events in the shot gathers. In the MuSPAC field analysis, Sections 4.9.5 and 4.9.6, we show the advantages of not correlating the vibroseis data with the source sweep and instead using the uncorrelated sweeps.

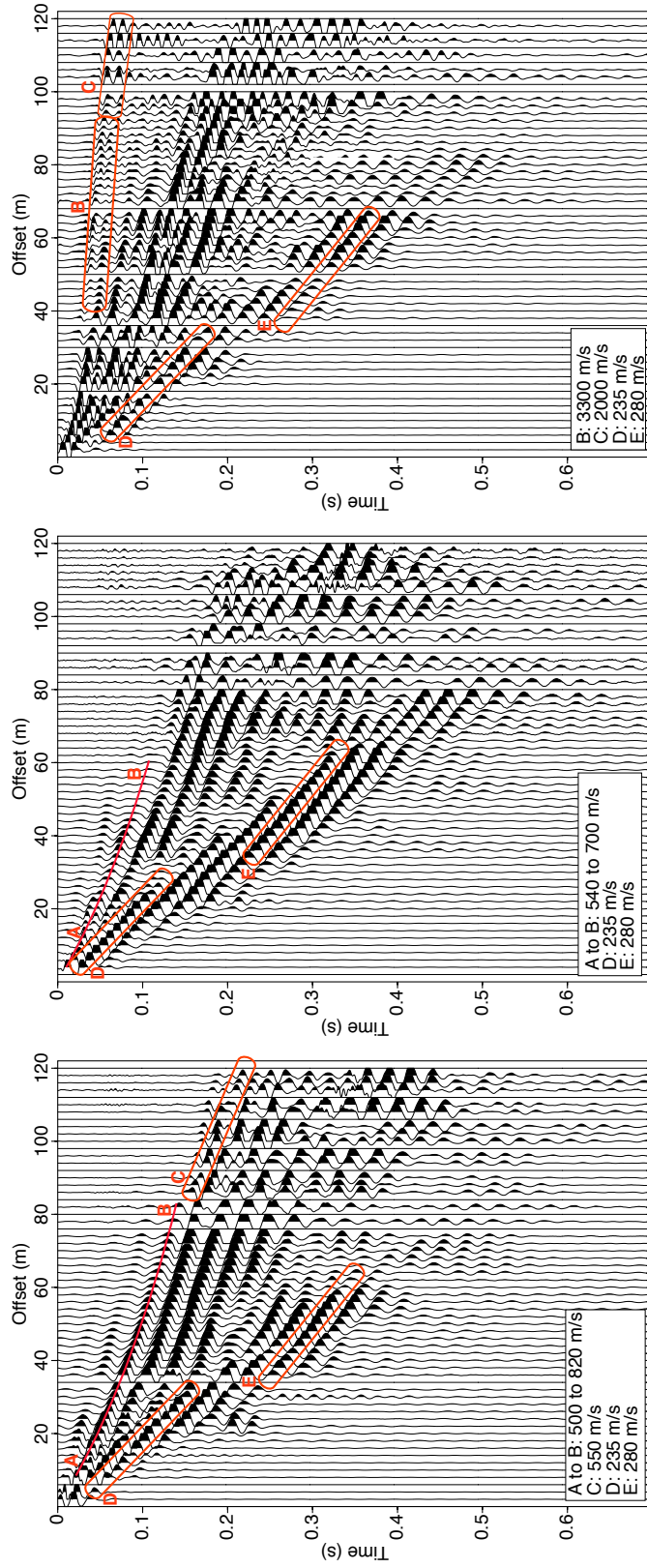


Figure 4.40: U_{xx} shot record acquired using a radial source at shot position 161 and recorded by radial receivers spaced 2 m apart from 161 to 220. The shot gather has been trace normalized.

Figure 4.41: U_{zx} shot record acquired using a radial source at shot position 161 and recorded by vertical receivers spaced 2 m apart from 161 to 220. The shot gather has been trace normalized.

Figure 4.42: U_{zz} shot record acquired using a vertical source at shot position 161 and recorded by vertical receivers spaced 2 m apart from 161 to 220. The shot gather has been trace normalized.

Refraction Tomography

We carried out a 2-D refraction tomography analysis using the correlated U_{zz} component seismic data. A commercial refraction tomography software code called RayFract (Intelligent Resources Inc.) was used. The vibroseis data were correlated using a synthetic sweep trace, time shifted to account for time shifts in the clipped pilot trace.

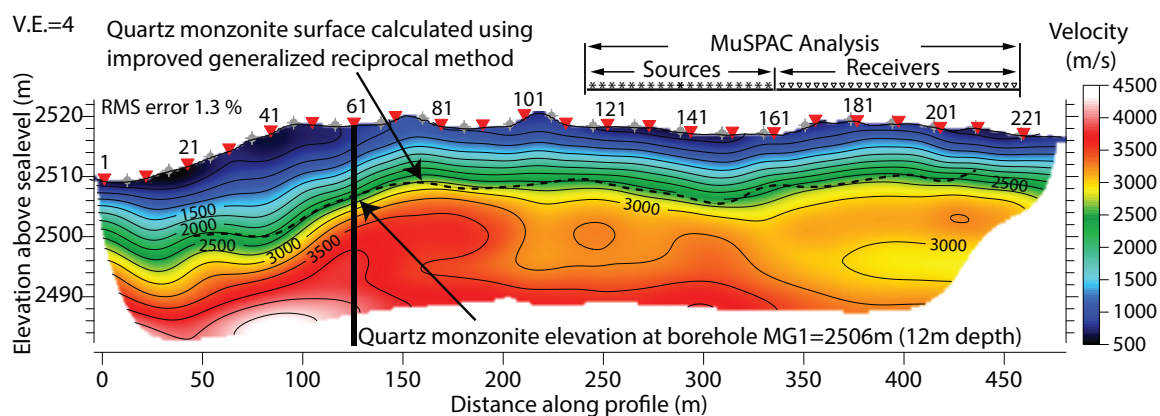


Figure 4.43: Velocity profile results from a refraction tomography analysis along the seismic acquisition line represented as the solid and dashed line in Figure 4.38. First breaks were picked from the correlated U_{zz} shot gathers extending from stations 1 to 236.

4.9.3 Discussion: Background Data

VSP and Well-Logs

The upper 30 m of the VSP gather presented in Figure 4.39 has interference from water and casing related wave modes. Well logs found the water table to vary between 6 and 8 m with measurements taken approximately 12 months apart. The water wave F2 and its intersection with the direct wave A, suggests that the water table depth is approximately 5 m. The well drillers log found a transition from sediments to quartz

monzonite at a depth of 10 m. The VSP gather in both panels of Figure 4.39 shows a high amplitude event at a depth of 10 to 12 m, however this event coincides with the water wave F2, and this hinders our ability to achieve a confident estimate of the velocity, depth, and extent for the quartz monzonite layer. Interpreting the VSP becomes easier at depths greater than 30 m, as the water wave no longer obscures the other wavefields. Events C and D show how the layer velocity transitions from a range of 2400-3400 m/s for C to 3400-4400 m/s for D at a depth of approximately 100 m. There appears to be a velocity slowdown in the depth interval of 95-105 m, which may be related to a fractured layer caused by hot water alteration. It may also be related to a geometry/observer logging error in the data acquisition.

Multi-Component Seismic Survey

A synthetic sweep trace was used to correlate the shot records presented in Figures 4.40, 4.41, and 4.42. This was because the pilot sweep trace recorded on the baseplate of the vibroseis was clipped. The main advantages of using the pilot sweep trace recorded on the baseplate is: 1) it provides the closest estimate of the source impulse imparted into the ground, and 2) it inherently ensures all correlated shots will have the same absolute zero time as the sweep and receivers are recorded using the same time trigger. However, the clipping of our pilot sweep trace would introduce significant errors during correlation. To avoid this error, yet retain the correct absolute times, a synthetic sweep trace is substituted and time shifted to match the static time shift of each clipped pilot sweep trace. This is done by autocorrelating our synthetic pilot sweep trace with all the clipped pilot sweep traces to estimate a series of static time shifts for each shot gather. The static time shifts were found to

vary by about +/-5 ms and these time shifts were applied to each of the synthetic sweeps used to correlate their respective shot gather.

The autocorrelation of vibroseis data creates a zero phase Klauder wavelet (Yilmaz, 2001). Sharp velocity gradients with a tight reflectivity series can make it difficult distinguish between the side lobes and central peak of these Klauder wavelets. This is because each layer velocity contrast has a different resultant amplitude caused by its associated reflectivity coefficient. Deconvolution can be used to collapse the Klauder wavelet to a spike (Robinson and Saggaf, 2001), however this was tried on a set of vibroseis shot gathers from the area without success. This failure is likely related to the complicated wavefield events of the sharp velocity gradients, which are discussed in further detail below.

In our field case, the near offsets prove to be the most difficult portion of our shot gathers to pick the correct absolute first arrival times. This is caused by the rapidly changing P-wave velocity profile in the 0-20 m depth range, which is estimated to vary from 600-3400 m/s. The wavefield events start to separate at the mid to long offsets, thus making it easier to identify their moveout velocities. We still cannot be certain of whether we are picking the central peak or related side lobe though. This does not matter if all we are interested in is estimating velocities of individual events, as the velocity of the side lobe and central peak for each specific event will be the same. The problem arises when we want to determine the absolute times for these events using first arrival picks. This cannot be done with any certainty and therefore our estimations of depths to layers and direct wave velocities using shot gather first arrival picks should be used with knowledge of this potential error.

Figure 4.40 shows a U_{xx} shot gather using a radial source located at station 161 and

recording the radial component on stations 161 to 220 off-end to the east (Figure 4.38). The shot gather shows a complicated wavefield with events arriving at the surface being reflected back and forth a number of times. These events are commonly referred to as multiples. This series of multiples are likely caused by the strong velocity contrasts in the upper 40 m between unsaturated sediments, saturated sediments, and basement rocks. The more prominent events are highlighted using red lines and their respective velocities are shown at the bottom left of the figure.

Events A and B in Figure 4.40 exhibit a transition in velocities from 500 to 820 m/s. This is indicative of a series of thin layers with increasing velocities across this depth range. We interpret this as a series of shear wave refractions radiating from the top of the altered quartz monzonite layer at $z = 10$ m through to the more competent granite at $z = 22$ m. Event C shows a slowdown in the shear wave refraction from 820 m/s to 550 m/s at receiver offset 86 m onwards, which may be caused by either an eastward dip in the altered quartz monzonite, or a series of offsetting faults. This deepening of the altered quartz monzonite is supported by the gravity gradient shown in Figure 4.38 and further evidence is presented below in Section 4.9.2, where we use refraction tomography. The loss of coherence in the signal between events B and C is also suggestive of a faulting structure that has been severely deformed. We term this velocity slowdown between receiver offsets 86 m and 118 m, as the DHL fracture zone.

Event D we interpret as part of the surface wave train and it has a group velocity of 235 m/s. The 280 m/s event E could be a multiple of the shear wave reflection from the top of the altered quartz monzonite layer. The other events with similar velocities to E look like they could be converging with D at larger offsets, which

would be indicative of a shear wave reflection. The lack of hyperbolic moveout over the 36-118 m offset range would be expected from a shallow 10 m layer interface.

Events A through C exhibit a series of multiples that attenuate with time. This is typical of a strong velocity gradients in shallow layers and can their amplitudes are similar to that of the surface wave train, which may cause contamination of our surface wave analyses and we will explore their effects through muting them in time.

Figure 4.41 shows a U_{zx} shot gather using a radial source at station 161 and recording the vertical component on stations 161 to 220. It shows the same events as the radially recorded component in Figure 4.40, with the exception of event C which is not as coherent. This is because the radial source is generating less amplitude on the vertical component and the signal has been attenuated more at longer offsets. An amplitude analysis showed that the ratio of amplitudes between the radial and vertical components is approximately 1.7:1.

Figure 4.42 shows a U_{zz} shot gather using a vertical source at station 161 and recording the vertical component on stations 161 to 220. It shows the same events D and E as the U_{xx} and U_{zx} shot gathers, with the exception of events B and C which are the parallel P-wave refractions to the S-wave refractions in Figures 4.40 and 4.41. The V_p/V_s ratio for the B refraction event on the altered quartz monzonite is approximately 4.0. This gives a Poissons ratio of 0.46. These ratios are not uncommon for highly altered and incompetent granite (Olona *et al.*, 2010) and would be classified with a weathering grade in the range of II-IV (Brown, 1981).

Refraction Tomography

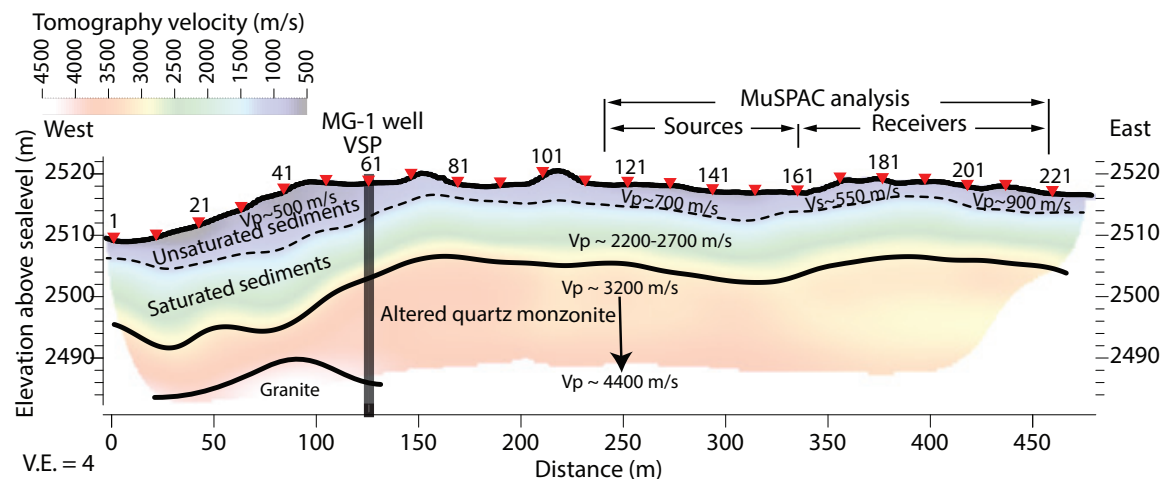


Figure 4.44: Interpretation along the seismic acquisition line extending from stations 1 to 236 in Figure 4.38. The interpretation is based upon refraction tomography velocities, VSP velocities, single shot gather interpretations, gravity data, and the well-log for borehole MG-1.

The refraction tomography velocity model presented in Figure 4.43 has an RMS error of 1.3% between the forward-modeled and observed first arrival picks. Figure 4.44 shows an accompanying interpretation of this velocity model. This interpretation was constrained by the MG-1 well log and VSP results presented in Sections 4.9.2 and 4.9.3. Our interpretation shows that the saturated sediments and altered quartz monzonite interfaces to the east of MG-1 appear to have little variability in elevation. There is a decrease in the velocity of the quartz monzonite to the east and this may be a result of geothermal alteration and more fracturing of the rock. The velocity profile shows a region of over 4000 m/s at an elevation of 2486 m near MG-1. This is further supported by the 4400 m/s event D in the VSP profile shown in Figure 4.39. The absence of this velocity to the east of the refraction velocity profile and slower

refraction events C shown in the shot gathers of Figures 4.40 and 4.42, further suggest a deepening in elevation of the competent granite to the east. Estimating the depth of this >4000 m/s layer is difficult to the east, however through observation of the slower quartz monzonite velocities and negative gravity gradient, we interpret this faster layer to be in the elevation range of 2480 to 2420 m, which corresponds to depth of range of 40 to 100 m. The lower elevation of 2420 m could be facilitated by an north-south offset ramp fault which is interpreted to cross in this region. This fault is shown traversing the DHL site in the left-hand panel of Figure 1.1 and its location based upon work by Miller (1999). This north-south ramp fault may also be responsible for the gravity gradient although this is speculation without having further gravity profiles to the east.

4.9.4 Introduction: MuSPAC Field Analysis

For the field case of the MuSPAC analysis, we use the 47, 60 channel, U_{xx} and U_{zx} shot records presented in Section 4.9.2, as the actual source used imparted a radial sweep from 30 to 300 Hz into the ground. For the purposes of demonstrating the advantages of the MuSPAC method when applied to field data, we choose to use different components of the four Green's functions that highlight specific discussions described later in the section. The results from the MuSPAC analysis were used to iterate through a number of numerical SEM models until the field and modeled data matched well. The 32 layer model shown in Figure 4.24 and discussed in Section 4.8 was the final iteration of this process and here we use the numerical ϕ coefficients and dispersion curves to estimate the missing zeros in our partial-band field data.

We explore a number of processing steps to enhance our MuSPAC analyses and

the results of these are presented in the following sections. We then end the section with a discussion of our MuSPAC results and how our interpretations from these results apply to our previous background data interpretations.

4.9.5 Results: MuSPAC Field Analysis

Virtual Shot Gathers

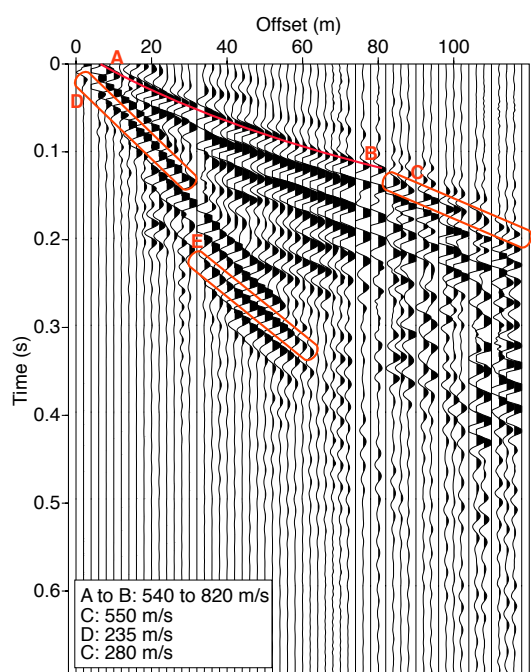


Figure 4.45: $G_{xx}(r, s_{162}, t)$ virtual shot record located at station 162. The virtual shot is calculated using cross-correlations of the uncorrelated sweep field data. The virtual shot gather has been trace normalized.

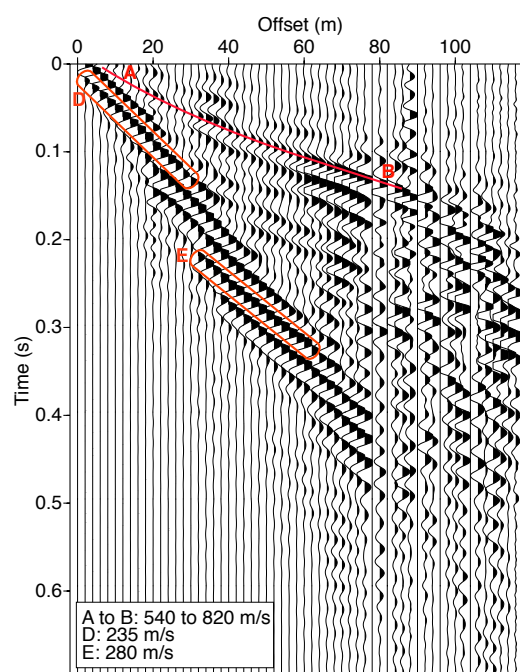


Figure 4.46: $G_{zz}(r, s_{162}, t)$ virtual shot record located at station 162. The virtual shot is calculated using cross-correlations of the uncorrelated sweep field data. The virtual shot gather has been trace normalized.

Uncorrelated Versus Correlated Vibroseis Sweep Data

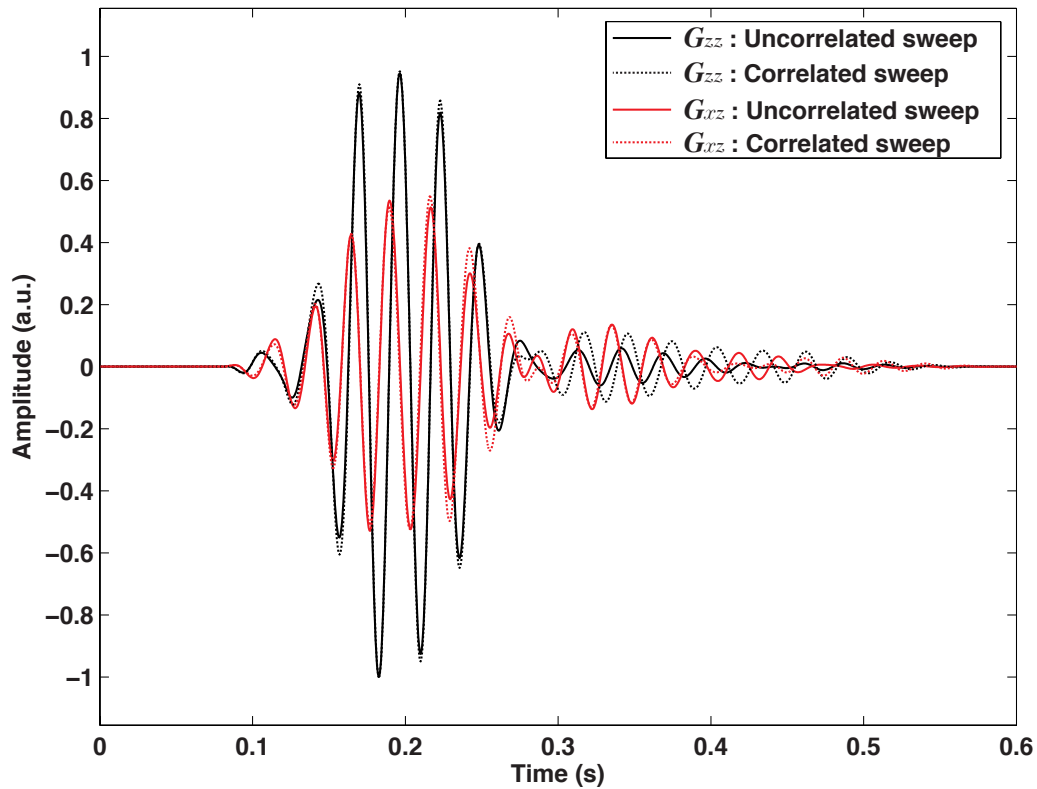


Figure 4.47: A comparison of Green's functions calculated from correlated and uncorrelated sweep data. Top muted $G_{zz}(s_{180}, s_{165}, t)$ and $G_{xz}(s_{180}, s_{165}, t)$ with a receiver separation of $r = 30$ m have been used.

Figure 4.47 compares the $G_{zz}(s_{180}, s_{165}, t)$ (black lines) and $G_{xz}(s_{180}, s_{165}, t)$ (blue lines) Green's functions for correlated (solid lines) and uncorrelated (dashed lines) receiver pairs. The data are for a virtual shot at station number 165 and a receiver position of 180 giving a total offset of $r = 30$ m. The signal at times before 0.08 seconds have been muted to zero and a cosine taper has then been applied from 0.08 seconds to 0.1 seconds.

Figure 4.48 shows the SPAC coefficients $\phi_{zz}(s_{190}, s_{162}, f)$ and $\phi_{xz}(s_{180}, s_{165}, f)$ that

are calculated from the Green's functions presented in Figure 4.47. The X and X' symbols in the inset figure, show the change in frequency for the fifth zero crossing ($m = 5$) between the uncorrelated and correlated vibroseis sweep data, respectively.

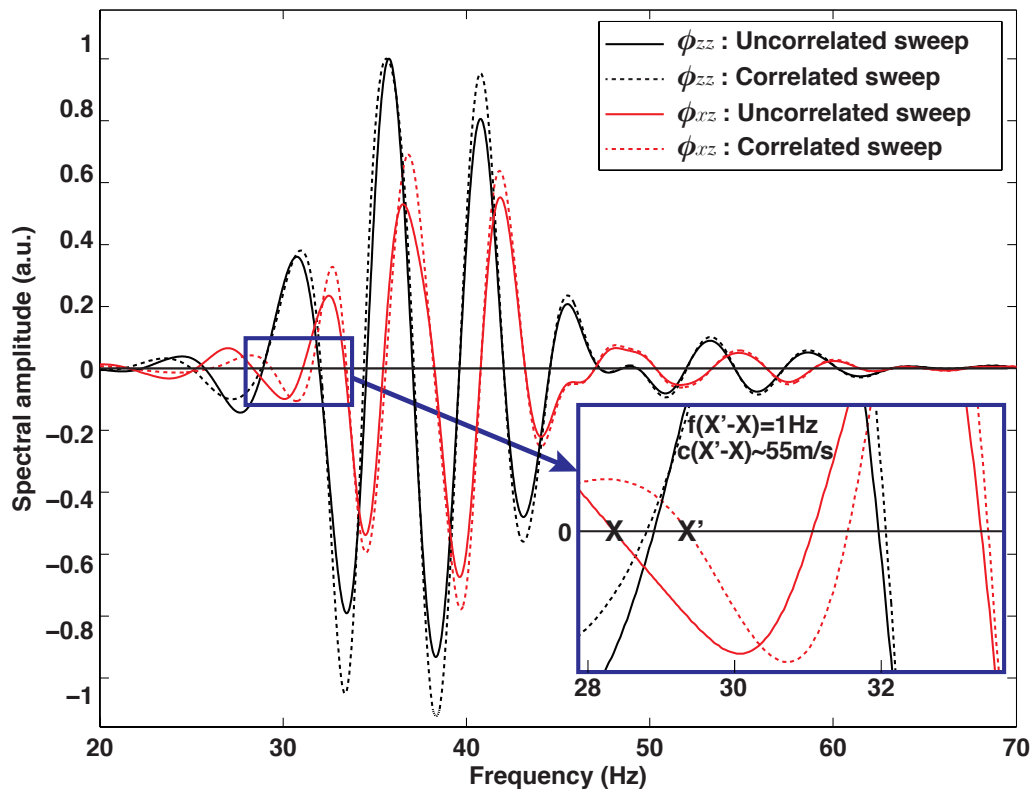


Figure 4.48: A comparison of SPAC coefficients calculated from correlated and uncorrelated sweep data. Top muted SPAC coefficients $\phi_{zz}(s_{190}, s_{162}, f)$ and $\phi_{xz}(s_{180}, s_{165}, f)$ with a receiver separation of $r = 30 \text{ m}$ have been used. The $\phi_{xz}(s_{180}, s_{165}, f)$ components show a difference of 1 Hz for their crossings between 28 and 30 Hz. X and X' shown in the inset box represent the shift in the fifth zero crossing to a higher frequency between the uncorrelated and correlated vibroseis data respectively.

Figure 4.49 shows a comparison of the dispersion curves for the correlated and uncorrelated based data. The frequency shift of the fifth zero crossing shown in Figure 4.48 for the $\phi_{xz}(s_{180}, s_{165}, f)$ cross-correlation coefficient is highlighted using

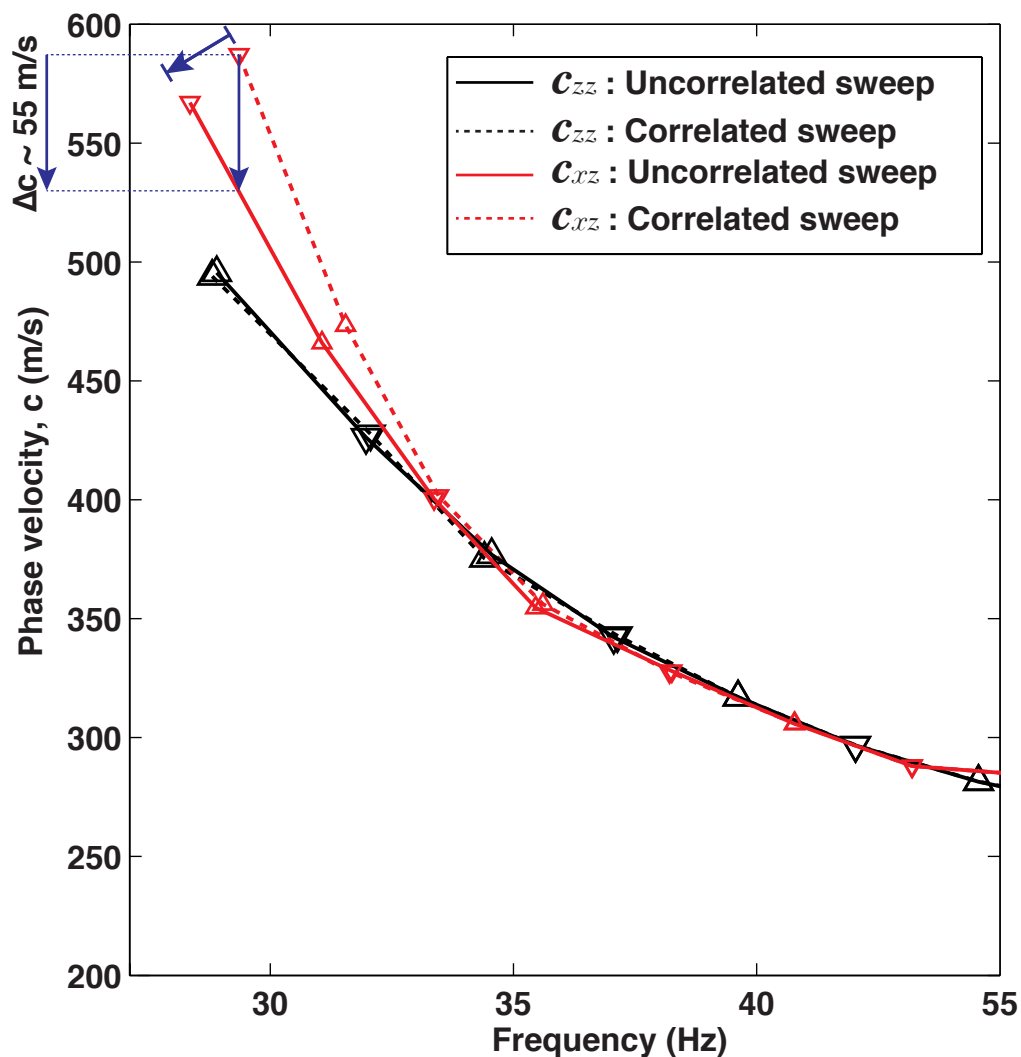


Figure 4.49: A comparison of velocity dispersion curves showing the differences between using correlated and uncorrelated sweep data. $m = 3$ for both components.

red arrows.

A MuSPAC Field Example Using $r = 28$ m

Here we present the Green's functions, SPAC coefficients, and phase velocity dispersion curves for $U_{xx}(176, 162, t)$ and $U_{zx}(176, 162, t)$. The location of the receiver

stations 162 and 176 used for this analysis is shown in Figure 4.38.

Figure 4.50 shows the $G(s_{176}, s_{162}, t)$ Green's functions for a single receiver pair with no muting.

Figure 4.51 shows the $G(s_{176}, s_{162}, t)$ Green's functions for a single receiver pair where all signal before 0.06 seconds has been muted to zero and a cosine taper has been applied between times 0.06 seconds and 0.12 seconds.

Figures 4.52 and 4.53 show the SPAC coefficients for the un-muted and muted Green's functions presented in Figures 4.50 and 4.51, respectively. A cut-off frequency of 28 Hz was used in the muted SPAC coefficients of Figure 4.53 as a threshold for retaining all zero crossings above this frequency.

Figure 4.54 shows the phase velocity dispersion curves for the muted Green's functions and SPAC coefficients presented in Figures 4.51 and 4.53, respectively, where four sets of missed zero crossings have been added. These sets of zero crossings are labeled A through D and they are selected to ensure that the direction of the first zero crossing correctly follows the theoretical direction of the related cosine or sine function, as previously discussed in Section 4.7. The full-band dispersion curve from the 32 layer forward model in Section 4.8.3 is included the figure and labeled as curve E.

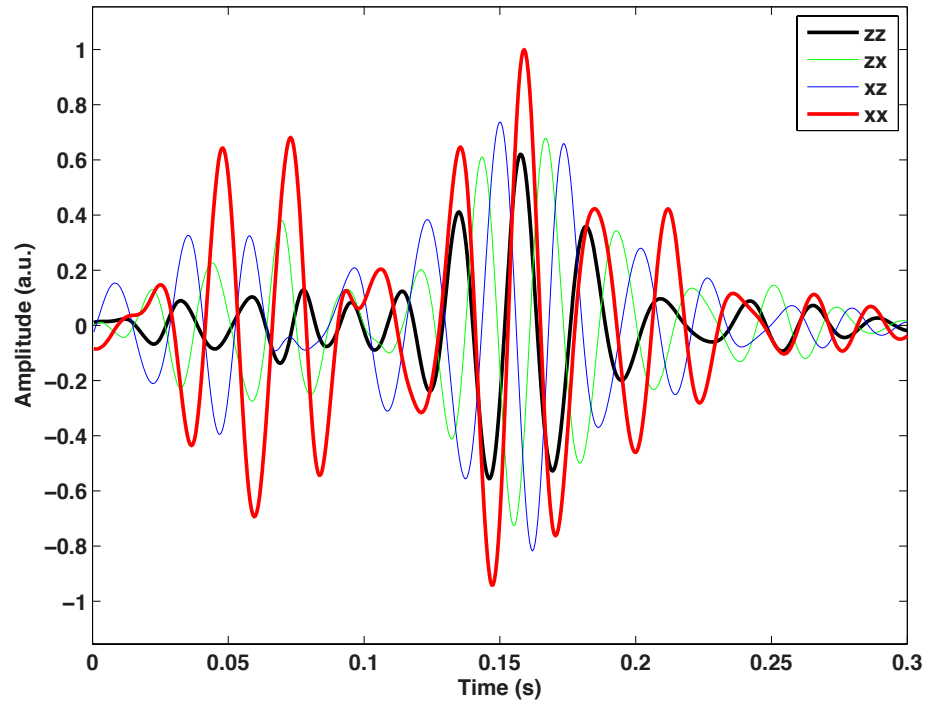


Figure 4.50: Un-muted Green's functions $G(s_{176}, s_{162}, t)$ for the field case where $r = 28$ m.

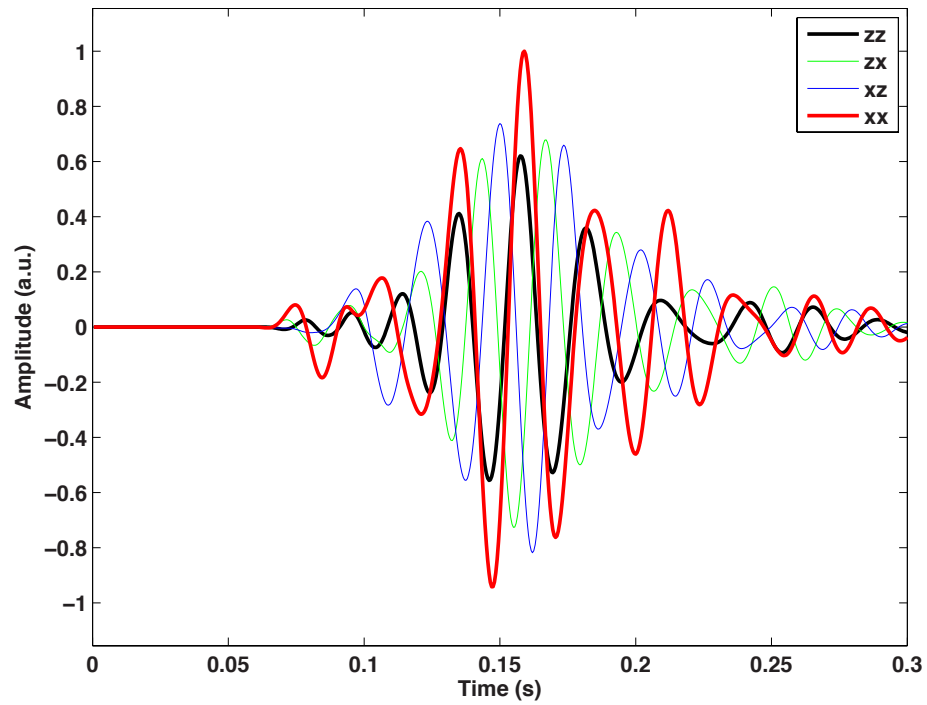


Figure 4.51: Top muted Green's functions $G(s_{176}, s_{162}, t)$ for the field case where $r = 28$ m.

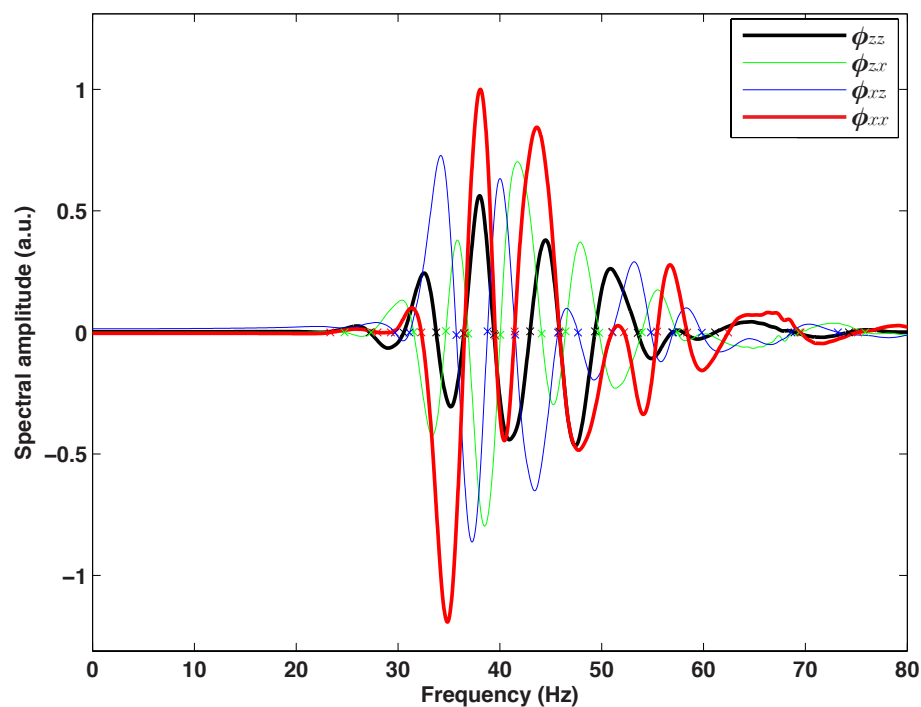


Figure 4.52: Un-muted SPAC coefficients $\phi(s_{176}, s_{162}, f)$ for the field case where $r = 28$ m.

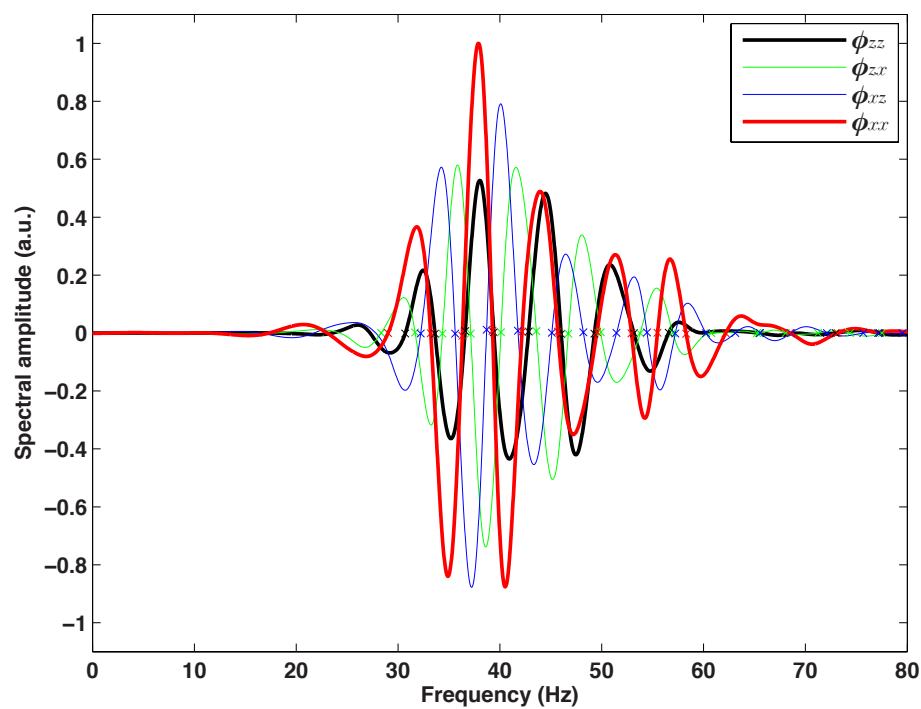


Figure 4.53: Top muted SPAC coefficients $\phi(s_{176}, s_{162}, f)$ for the field case where $r = 28$ m.

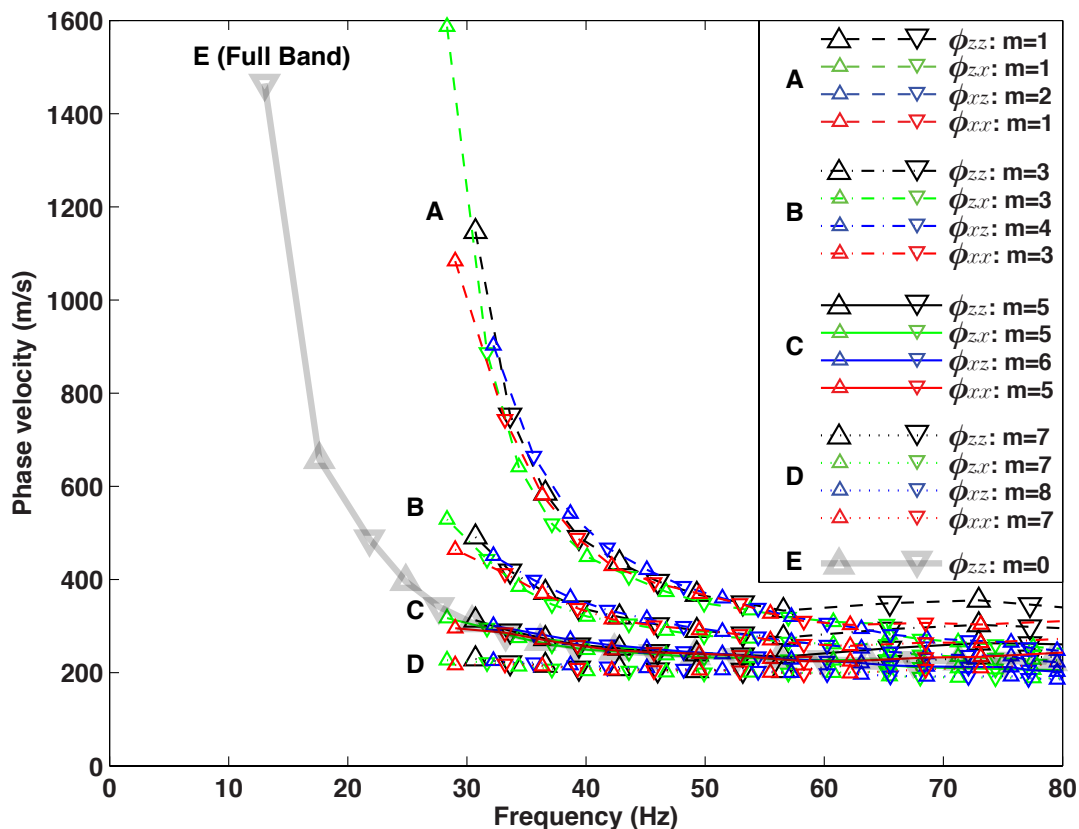


Figure 4.54: Top muted velocity dispersion curves $c(s_{176}, s_{162}, f)$ with a range of added zero crossings for the field case where $r = 28 m$. The semi-transparent and full color dispersion curves are for full-band and partial-band data respectively. The full-band curve E is based upon the 32 layer numerical model presented in the previous section. It shows that in our field case, that we have missed zero crossings as defined by $m_{zz, zx, xx} = 5$ and $m_{xz} = 6$ in the frequency range of 0-28 Hz where we did not sweep.

A Cross-Correlation Coefficient Gather

Here we present cross-correlation SPAC coefficient gather results for both SPAC (single component) and MuSPAC (four components). The SPAC and MuSPAC gather traces are shown in the left and right hand panels of Figure 4.55, respectively. Each SPAC coefficient trace is located at the common midpoint (CMP) between the receivers used in the SPAC and MuSPAC analyses. The dispersion curves phase velocity derived from the 7th zero crossing is shown in the corresponding panels above the gathers. This velocity is only useful for subjectively examining lateral variability as it does not represent velocity at a specific depth.

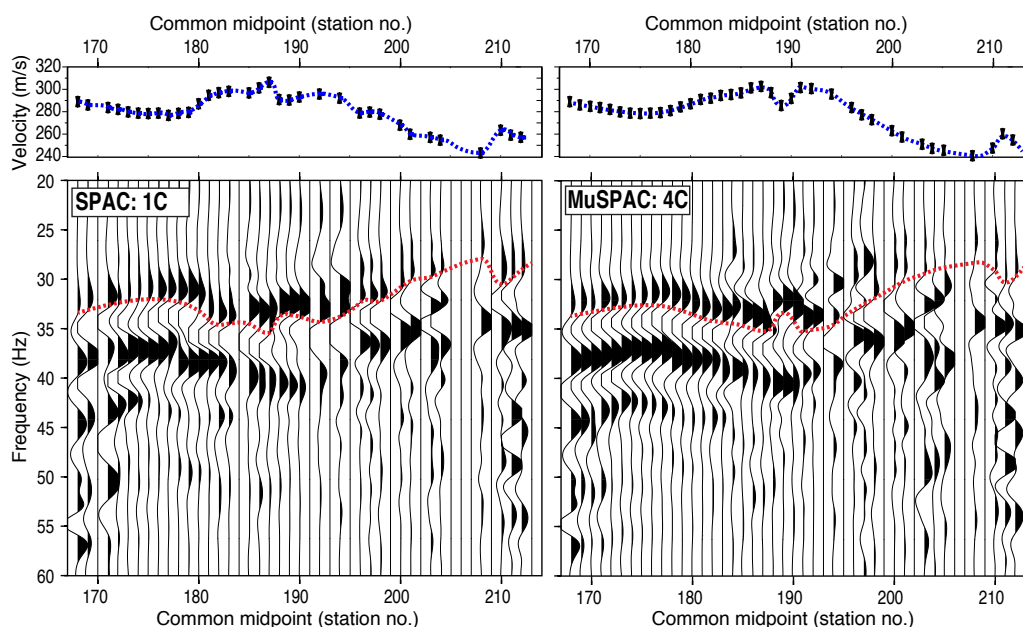


Figure 4.55: Left panel: The lower panel shows a gather of cross-correlation coefficient traces for $\phi_{xx}(s_{n+R}, s_n, f)$ for the field case where $n = 168$ to 213 and $R = 14$ refers to a separation of 14 stations or $r = 28$ m. The dashed red line shows the 7th zero crossings which is in-turn a proxy for changing velocity. The phase velocity corresponding to the 7th zero crossings is shown in the top panel. Right panel: The bottom panel shows a gather of all four cross-correlation coefficient components summed together for each trace. It is for the same field case as the left panel.

A MuSPAC Field Example Using $r = 56$ m

Here we present the results of doubling the receiver separation from the previous sections from $r = 28$ m to $r = 56$ m. The corresponding results for the Green's functions, SPAC coefficients, and dispersion curves were previously presented in Figures 4.56, 4.57, and 4.58 below. All data have been top muted to zero from times $t=0$ seconds to $t=0.22$ seconds and then a cosine taper was applied from $t=0.22$ seconds to 0.34 seconds.

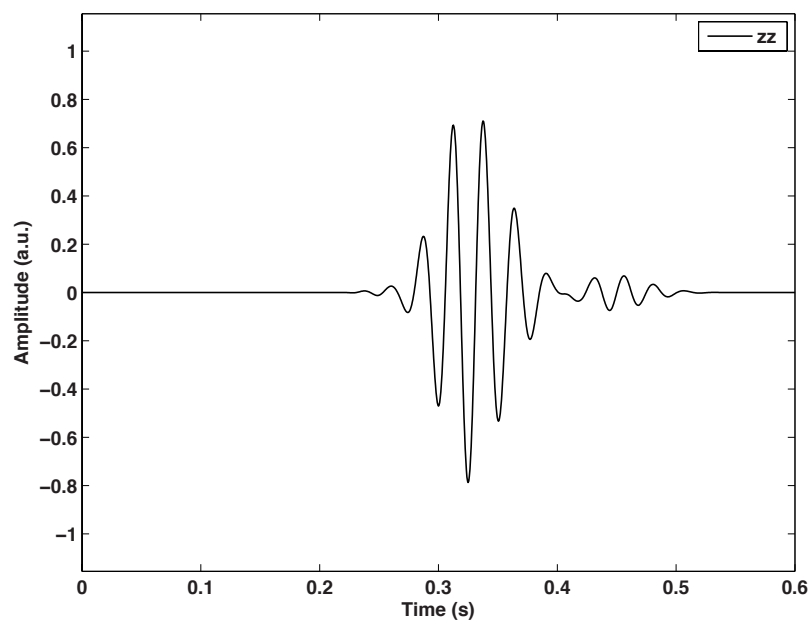


Figure 4.56: Top muted Green's functions $G(s_{190}, s_{162}, t)$ for the field case where $r = 56 m$.

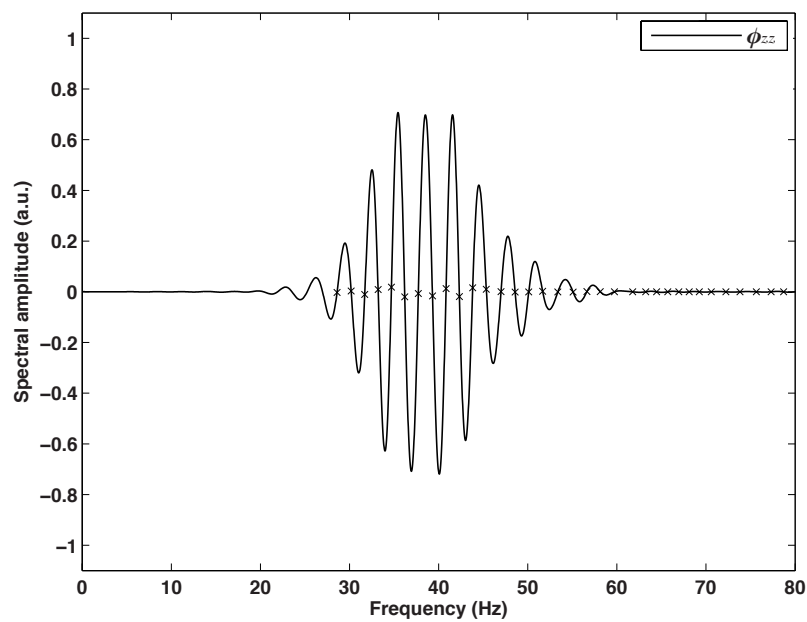


Figure 4.57: Top muted SPAC coefficients $\phi(s_{190}, s_{162}, f)$ for the field case where $r = 56 m$.

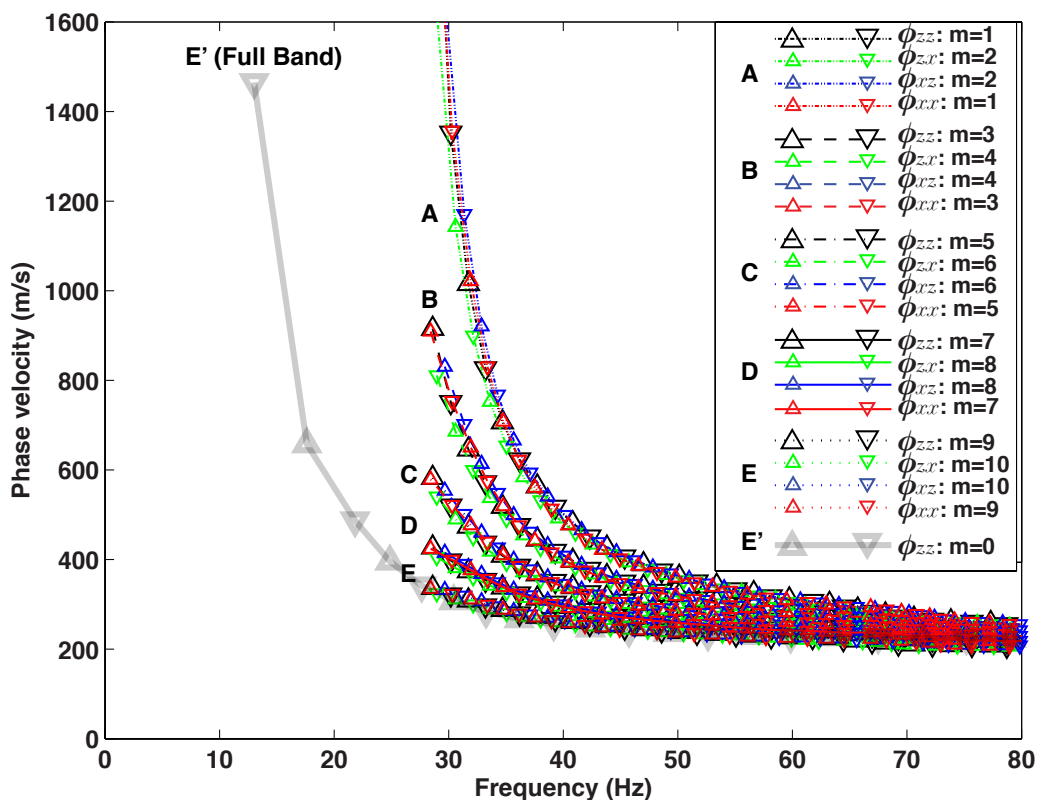


Figure 4.58: Top muted velocity dispersion curves $c(s_{190}, s_{162}, f)$ with a range of added zero crossings for the field case where $r = 56 m$. The semi-transparent and full color dispersion curves are for full-band and partial-band data respectively. The full-band curve E is based upon the 32 layer numerical model presented in the previous section. It shows that in our field case, that we have missed zero crossings as defined by $m_{zz, zx, xx} = 5$ and $m_{xz} = 6$ in the frequency range of 0-28 Hz where we did not sweep.

4.9.6 Discussion: MuSPAC Field Analysis

Virtual Shot Gathers

Figure 4.45 of the $G_{xx}(190, 162, t)$ Green's function shows the same events A through E as the real U_{xx} shot record in Figure 4.40, except it has improved signal coherency. This is due in part to the summation process improving the signal to noise ratio and the cross-correlation process removing non-linear events such as reflections. The interpreted shear wave reflections E have not been removed as they are approximately linear from offsets of 20 m upwards.

Like $G_{xx}(r, s_{162}, t)$, the virtual show record of $G_{zz}(r, s_{162}, t)$ in Figure 4.46 closely resembles the real U_{zz} shot record in Figure 4.41, except it has a higher level signal coherency. In particular, the refracting event B can be interpreted to a longer offset of 86 m where the DHL fracture zone commences. The amplitudes of the multiples from events A through B, in the offset range of 34 m to 60 m, have also been reduced in the virtual shot record $G_{zz}(r, s_{162}, t)$. This has the overall benefit of enhancing the relative dominance of the surface wave train and will improve the lower frequency surface wave energy that likely exists in this portion of the shot record. This is opposite to the reduction in amplitude of the corresponding faster events in the slab and 32-layer models in Sections 4.5 and 4.8, respectively. This suggests that the events in the field case have a linear moveout and are therefore either higher mode surface waves or refractions and their multiples. The faster events in the slab and 32-layer model were subdued by cross-correlating because they did not have a linear moveout and are therefore most likely reflections and their multiples.

Uncorrelated Versus Correlated Vibroseis Sweep Data

One of the advantages of the MuSPAC method is that we can use uncorrelated vibroseis data. Correlating these data with their pilot sweep trace prior to the MuSPAC analysis would be detrimental to the analysis as this only adds error through the introduction of added processing with a sweep trace that is not a perfect representation of the input impulse. In this section, we provide an example of the benefits of using uncorrelated sweep data by comparing the MuSPAC analysis results between uncorrelated and correlated shot data.

Figure 4.47 compares the $G_{zz}(s_{180}, s_{165}, t)$ (black lines) and $G_{xz}(s_{180}, s_{165}, t)$ (blue lines) Green's functions for correlated (solid lines) and uncorrelated (dashed lines) receiver pairs. The data are for a virtual shot at station number 165 and a receiver position of 180 giving a total offset of $r = 30$ m. The largest observable phase change between the uncorrelated and correlated based Green's functions occurs in the time span from 0.28 seconds to 0.5 seconds, where correlated and uncorrelated $G_{zz}(s_{180}, s_{165}, t)$ based Green's functions are up to 90° out of phase. The frequency of the correlated $G_{zz}(s_{180}, s_{165}, t)$ based Green's function in this range is approximately 30 Hz and the removal of this phase change is observed in the related $\phi_{zz}(s_{180}, s_{165}, f)$ and $\phi_{xz}(s_{180}, s_{165}, f)$ SPAC coefficients shown in Figure 4.48. This figure shows the resultant cross-term, $\phi_{xz}(s_{180}, s_{165}, f)$ having the largest change with its fifth zero crossing ($m = 5$) increasing in frequency by approximately 1 Hz. There are continued frequency shifts in the zero crossings at higher frequencies that diminish to almost 0 Hz by the 10th zero crossing at 45 Hz. These differences demonstrate the error introduced by correlating the measured receiver response with the sweep trace that is not an exact representation of the imparted source signal.

Figure 4.49 shows a comparison of the dispersion curves for the correlated and uncorrelated based data. The frequency shifts observed in the $\phi_{xz}(s_{180}, s_{165}, f)$ cross-correlation coefficient in Figure 4.48 can be seen to cause a corresponding reduction in $c_{xc}(s_{180}, s_{165}, f)$ of ~ 55 m/s at the fifth zero crossing. This estimation of the velocity change is approximate because it assumes a linear velocity profile between crossings.

This one example demonstrates how using correlated versus uncorrelated sweeps can cause up to a 10% variation in our phase velocity dispersion curve estimates for zero crossings near 30 Hz. We therefore base all our subsequent analyses in this section on the uncorrelated sweep data to minimize error introduced through correlating the vibroseis data with its pilot sweep trace.

A MuSPAC Field Example Using $r = 28$ m

Here we calculate a phase velocity dispersion curve for our field data between receiver stations 162 and 176. In our numerical analyses in Sections 4.7 and 4.8.3, we showed how body wave events that contaminate the surface wave signal can cause changes in our phase velocity estimates. Event B identified in Figures 4.40 through 4.42, and Figures 4.45 and 4.46 and its later multiples, we interpret as a non-surface wave related event or a non-random higher mode surface wave. This is because its reduction in amplitude in the $G_{zz}(s_{180}, s_{165}, t)$ Green's function (Figure 4.46) suggests it may not be a surface wave. Were event B and its multiples related to surface waves, then the cross-correlation process would preserve and enhance these events, rather than degrade them. We therefore try to isolate the surface wave train identified as D in these figures through early time muting of event B, referred to hereafter as top muting.

Top muting will have the detrimental effect of removing faster and lower frequency surface wave arrivals. These faster surface wave arrivals would have sampled the lower depths of our field site due to their longer wavelengths.

The $G(s_{176}, s_{162}, t)$ Green's functions shown in Figure 4.50 shows event B in the time range of 0.03 seconds through to 0.1 seconds. This event B was previously interpreted as not being a surface wave due to its amplitude being reduced in the Green's function. When the zero crossings between components in the un-muted and muted SPAC coefficients of Figures 4.52 and 4.53 are compared respectively, the muted zero crossing data show much tighter coherency amongst the cross-terms $\phi_{zx}(s_{176}, s_{162}, f)$ and $\phi_{xz}(s_{176}, s_{162}, f)$, and the diagonal terms $\phi_{zz}(s_{176}, s_{162}, f)$ and $\phi_{xx}(s_{176}, s_{162}, f)$. This improvement in coherency of zero crossings, through the removal of event B, suggests it is a body wave. It may also be a higher-order mode of the surface wave, although one would expect the Green's function to enhance its amplitude, if this were the case.

The phase velocity dispersion curves for the muted field case are shown in Figure 4.54. The $c_{zz}(176, 162, f)$ dispersion curve from the full-band numerical 32 layer model is shown to help determine the correct number of zero crossings missed in our partial-band field data. This modeled dispersion curve E was estimated through an iterative process between the 32 layer numerical model and this field data. The similarities between the main wavefield events in the field and numerical shot records (see Sections 4.8.3 and 4.9.2) along with the close match between E and C in Figure 4.54, suggest that the 32 layer velocity model presented in Figure 4.24 is an accurate representation of the subsurface between the 162 and 176 receiver pairs.

A Cross-Correlation Coefficient Gather

The lower left panel of Figure 4.55 shows a collection of $\phi_{xx}(s_n + R, s_n, f)$ cross-correlation SPAC coefficient curves where $n = 168$ to 213 and $R = 14$ stations ($r = 28$ m). These SPAC coefficient curves are based upon the radial component. The red dashed line represents the 7th zero crossing for each curve, and its trend shows the lateral change in phase velocity changes across the receiver line for common midpoints. An upward trend in this line to lower frequencies near common midpoint 187 represents a slowdown in velocity. Equation 4.6 can help to intuitively understand this trend, where the frequency (f) and phase velocity (c_n) are linearly proportional to each other. The blue dashed line in the upper panel, shows the corresponding velocities for the 7th zero crossings using Equation 4.6. This velocity profile has a general downward trend in the phase velocity from midpoint 187 to 212 of approximately 60 m/s. The 10 m/s increase in velocity between common midpoint 208 and 210 may be an error caused by a skipped zero crossing. Instead the 7th zero crossings for these last three traces may be at a frequency less than 28 Hz and instead the blue and red dashed lines are marking the 8th zero crossings for these last three common midpoints. This is quite feasible as the frequency band of our field data only extends down to about 28 Hz. Should this be the case, then the dash blue velocity profile would continue its downward velocity trend for these last three traces, which having a upward step between common midpoints 208 and 210.

The lower right panel of Figure 4.55 shows a collection of $\phi_{xx}(s_n + R, s_n, f)$ cross-correlation MuSPAC coefficient curves where $n = 168$ to 213 and $R = 14$ stations ($r = 28$ m). These MuSPAC coefficient curves are based upon the summation of all four components. Comparison of the SPAC and MuSPAC gathers shown in the left

and right hand panels of Figure 4.55 demonstrate the improvement in signal coherency through summation of all four components. In particular, the CMP stations from 168 to 194 show less variability in the MuSPAC example. Furthermore, the summation process also fills in some of the missing channels in the SPAC gather such as CMPs 170, 184, 191, and 205. There is also an improvement in the signal of the higher frequency zero crossings in the frequency range of 41 to 47 Hz and CMPs 168 to 184.

This gather of ϕ curves is a useful means of quickly assessing spatial changes in lateral velocity. Different receiver separations r can be used to control the number of ϕ gather zero crossings across a specific frequency range. For example, increasing r will cause more phase changes between two receiver pairs and therefore a corresponding increase in the zero crossings. This has a detrimental effect caused by the averaging of the lateral velocity structure over the larger r , even though it adds a higher density of zero crossings for a given frequency range. This increase in r therefore makes it more difficult to determine the correct number of zeros to be added as the sensitivity of the dispersion curves to changes in m will have been reduced.

The increased zero crossing density in ϕ caused by doubling the value of r from 28 m to 56 m is shown in Figure 4.57 where $\phi(s_{190}, s_{162}, f)$ is plotted. When compared to $\phi(s_{176}, s_{162}, f)$ for $r = 28$ m in Figure 4.53, the approximate doubling of the frequency between zero crossings, caused by the doubling of r , is readily apparent. Figure 4.58 shows the corresponding dispersion curves for $\phi(s_{190}, s_{162}, f)$ in Figure 4.57. The dispersion curves shown much less variability with m as compared to the dispersion curves in Figure 4.54, which use a receiver station separation of $r = 28$ m. While Figure 4.54 shows only two dispersion curves (B and C) that may be realistic fits, the decreased variability between curves in Figure 4.58 makes choos-

ing the correct number of missed zero crossings much more difficult. There could be up to 4 possible values of m that could be used, of which three are shown in this figure using the labels C, D, and E. The next curve below E would likely be a possible choice also as it will a curve that falls somewhere between C and D in Figure 4.54.

In summary, the ϕ gather plots provide a useful method of comparing our data and assessing the relative data quality between receiver pairs. They help identify the most appropriate receiver pairs for phase velocity dispersion analysis. They also help with determining appropriate values of m that can be selected according to the lateral variability in velocity observed across this gathers. For example, should the lateral change in velocity be relatively small for a specific receiver interval, then one could consider increasing r across this interval to achieve more depth resolution. The ϕ gather plots also help with interpretation of lateral variations in velocity, however caution must be used as they are not a direct indicator of velocity structure.

4.10 Conclusions

We have shown that we can successfully retrieve phase velocities for both numerical and field based data using the MuSPAC method. Through its use of interferometry with two wavefield components, the method's advantages over existing surface wave techniques include: 1) the addition of three dispersion curves to reduce error, 2) the enhancement of the signal to noise ratio through summation of sources and, 3) the ability to use any source term. In our field example, the ability to use the uncorrelated over the correlated vibroseis data proved to be a significant advantage for two reasons. The first, that is specific to our case, was our pilot sweep trace was partially clipped and using it to correlate would have introduced error. The second reason, that is more general and common to all vibroseis data, is the elimination of the need to measure the actual impulse that was imparted into the ground by the vibroseis trucks plate.

We have shown that for most cases, the challenge of partial-band data and missed zero crossings can be overcome by selecting an appropriate receiver separation distance and constraining the dispersion curves by using prior observed knowledge (e.g., Ekström *et al.*, 2009). We have demonstrated how the method's accuracy is improved by using interferometry to sum over shots, thereby reducing the effect of non-linear events (e.g., reflected waves) and improving the signal-to-noise ratio due to the removal of incoherent noise. For contamination of the surface wave not removed by interferometry, we have shown that time based muting can enhance the Rayleigh wavefield and improve our estimates of the phase velocity. Caution must be used when muting as it can also remove the lower frequency surface wave information that inherently travels at faster velocities due to its sampling of the deeper and faster layers.

All of our analyses for the Deadhorse lake field site fit a four layered system that, with increasing depth, is composed of unsaturated sediments, saturated sediments, altered quartz monzonite and granite. Our interpretations of these layers are shown in Figures 4.44 and 4.24. Our seismic and gravity based data show evidence for the N-S ramp fault (Miller, 1999) between Mount Antero and Mount Princeton at station 190 on our seismic line and stepping down to the east. This may well be a pathway for hot geothermal waters and would provide a good opportunity for further geophysical investigations along its strike through Chalk Creek valley.

FUTURE WORK

Seattle Fault Zone

Future work for enhancing our work at the western limits of the Seattle fault zone could include filling in some of the data gaps that exist across Hood Canal and to the south. Other than acquiring higher energy seismic data, lower cost options could include acquiring some joint 2-D magnetic and gravity data E-W transects that extend from Big Beef creek to the western shores of Hood Canal with parallel E-W transects extending down south to the Tacoma fault. These could then be tied together by using one or two N-S magnetic and gravity transects that extend from the Seattle to the Tacoma faults. The difficulty in this region is access to suitable pathways and it may be more practical to acquire the magnetic data using a low flying aircraft. The gravity data can then be acquired at points along the magnetic transects where access is available.

Geological Setting of Mount Princeton Hot Springs

The most significant contribution to the geological setting from our work in Chapters 2 and 3 is the imaging of the ramp fault traversing the eastern margin of DHL. The exact location of this fault and another segment interpreted by Miller (1999) to be about 1 km to the east was uncertain prior to our studies at DHL. A deep

seismic survey run down the entire length of Chalk Creek valley in 2008 (Blum *et al.*, 2009) tried to image the Sawatch fault but the seismic section was not very clear and therefore difficult to interpret. This was largely due to the sharp and shallow geological contrasts and to some extent the acquisition parameters. Our work serves to add more certainty to location of the ramp fault and the possibility that it may have a series of steps to the east, as demonstrated by our data locating it further to the west than previously interpreted.

Previous work by Richards *et al.* (2010) showed the effectiveness of combining self-potential with DC resistivity for identifying fault systems that are pathways for geothermal fluids. We have shown the additional benefit of using seismic and gravity to image the structure of these systems in this geological setting. For future work, we would recommend a combined field campaign using these four methods to image the ramp fault steps further to the east. Each of these steps may have the potential to be significant pathways for upwelling geothermal waters and thus providing the local area with an invaluable renewable resource.

The MuSPAC Method

Even in the complicated geological setting of Deadhorse lake with a data set of relatively low signal to noise, the MuSPAC method proved to be an effective means of characterizing the near surface. For future work, we would suggest extending the method to use sources that traverse through the line, and not just offset to one end. This will further improve the signal to noise ratio and the methods ability to provide more accurate velocities. We also recommend using the widest available frequency band, especially on the low end, to help with assessing the number of missed zero

crossings.

In our field case, we had to record each component separately and we believe that without careful attention to detail that this could introduce error associated with not revisiting the exact same locations or uncertainty about the sources location. This is especially detrimental to the MuSPAC method as it depends on having the correct phase shifts between components. It was for this reason that we had to use the weaker radial source data over the vertical source data as there was significantly more uncertainty about the geometric accuracy of our vertical source data set.

The use of multiple sources at the same time could also be explored as the MuSPAC method does not require any source synchronization or timing information.

REFERENCES

- K. Aki. 1957. Space and time spectra of stationary stochastic waves, with special reference to microtremors. *Bull. Earthq. Res. Inst.*, **35**, 415–456.
- B. F. Atwater, and E. Hemphill-Haley. 1997. *Recurrence intervals for great earthquakes of the past 3,500 years at northeastern Willapa bay, Washington*. U.S. Geological Survey Open-File Report 100-249-011.
- B. F. Atwater, and A. L. Moore. 1992. A Tsunami About 1000 Years Ago in Puget Sound, Washington. *Science*, **258**(5088), 1614–1617.
- R. S. Babcock, R. F. Burmester, D. C. Engebretson, A. Warnock, and K. P. Clark. 1992. A Rifted Margin Origin for the Crescent Basalts and Related Rocks in the Northern Coast Range Volcanic Province, Washington and British Columbia. *Journal of Geophysical Research*, **97**, 6799–6821.
- A. J. Berkhout. 2012. Blended acquisition with dispersed source arrays. *Geophysics*, **77**(4), A19–A23.
- R. J. Blakely, R. E. Wells, and C. S. Weaver. 1999. *Puget sound aeromagnetic maps and data*. U.S. Geological Survey Open-File Report 99-514.
- R. J. Blakely, R. E. Wells, C. S. Weaver, and S. Y. Johnson. 2002. Location, structure, and seismicity of the Seattle fault zone, Washington: Evidence from aeromagnetic anomalies, geologic mapping, and seismic-reflection data. *Geological Society Of America Bulletin*, **114**(2), 169–177.

- R. J. Blakely, D. A. John, S. E. Box, B. R. Berger, R. J. Fleck, R. P. Ashley, G. R. Newport, and G. R. Heinemeyer. 2007. Crustal controls on magmatic-hydrothermal systems: A geophysical comparison of White River, Washington, with Goldfield, Nevada. *Geosphere*, **3**(2), 91–107.
- R. J. Blakely, B. L. Sherrod, J. F. Hughes, M. L. Anderson, R. E. Wells, and C. S. Weaver. 2009. Saddle Mountain fault deformation zone, Olympic Peninsula, Washington: Western boundary of the Seattle uplift. *Geosphere*, **5**(2), 105–125.
- R. J. Blakely, B. L. Sherrod, C. S. Weaver, R. E. Wells, A. C. Rohay, E. A. Barnett, and N. E. Knepprath. 2011. Connecting the Yakima fold and thrust belt to active faults in the Puget Lowland, Washington. *Journal Of Geophysical Research*, **116**(B07105), 1–33.
- T. Blum, K. van Wijk, L. Liberty, M. Batzle, R. Krahenbuhl, A. Revil, and R. Reynolds. 2009. Characterization of a geothermal system in the Upper Arkansas Valley, CO. *SEG Technical Program Expanded Abstracts*, **28**(1), 1289–1293.
- M. T. Brandon, M. K. Roden-Tice, and J. I. Garver. 1998. Late Cenozoic exhumation of the Cascadia accretionary wedge in the Olympic Mountains, northwest Washington State. *Geological Society of America Bulletin*, **110**(8), 985–1009.
- T. M. Brocher, and A. L. Ruebel. 1998. *Compilation of 29 sonic and density logs from 23 oil test wells in western Washington State*. U.S. Geological Survey Open-File Report 98-249.
- T. M. Brocher, T. Parsons, J. Blakely, Richard, N. I. Christensen, M. A. Fisher, and R. E. Wells. 2001. Upper crustal structure in Puget Lowland, Washington:

- Results from the 1998 Seismic Hazards Investigation in Puget Sound. *Journal of Geophysical Research*, **106**(B7), 13541–13564.
- T. M. Brocher, R. J. Blakely, and R. E. Wells. 2004. Interpretation of the Seattle Uplift, Washington, as a Passive-Roof Duplex. *Bulletin of the Seismological Society of America*, **94**(4), 1379–1401.
- E. T. Brown. 1981. *Rock characterization, testing & monitoring: ISRM suggested methods*. Published for the Commission on Testing Methods, International Society for Rock Mechanics by Pergamon Press.
- R. C. Bucknam, E. Hemphill-Haley, and E. B. Leopold. 1992. Abrupt Uplift Within the Past 1700 Years at Southern Puget Sound, Washington. *Science*, **258**(5088), 1611–1614.
- C. R. Clement, T. L. Pratt, M. L. Holmes, and B. L. Sherrod. 2010. High-Resolution Seismic Reflection Imaging of Growth Folding and Shallow Faults beneath the Southern Puget Lowland, Washington State. *Bulletin of the Seismological Society of America*, **100**(4), 1710–1723.
- S. M. Colman, J. P. McCalpin, J. P. Ostenaar, and D. A. Kirkham. 1985. Map showing Upper Cenozoic rocks and deposits and Quaternary faults, Rio Grande Rift, south-central Colorado. *U.S. Geological Survey Miscellaneous Investigations Map I-1594*. U.S. Geological Survey, Denver, CO.
- S. V. Dadisman, S. Y. Johnson, and J. R. Childs. 1997. *Marine, High-Resolution, Multichannel, Seismic-Reflection Data Collected During Cruise G3-95-Ps, Northwestern Washington*. U.S. Geological Survey Open-File Report 97-735.

- Z. F. Dane, M. M. Bonno, E. Brau, W. D. Gilham, T. F. Hoffman, D. Johansen, M. H. Jones, B. Malfait, J. Masten, and G. O. Teague. 1965. Geophysical Investigation of the Southern Puget Sound Area, Washington. *Journal of Geophysical Research*, **70**(22), 5573–5580.
- G. Ekström, G. A. Abers, and S. C. Webb. 2009. Determination of surface-wave phase velocities across USArray from noise and Aki’s spectral formulation. *Geophysical Research Letters*, **36**(L18301), 1–5.
- E. Faccioli, F. Maggio, R. Paolucci, and A. Quarteroni. 1997. 2D and 3D elastic wave propagation by a pseudo-spectral domain decomposition method. *Journal of Seismology*, **1**, 237–251.
- J. P. Fairley, and J. J. Hinds. 2004. Rapid transport pathways for geothermal fluids in an active Great Basin fault zone. *Geology*, **32**(9), 825–828.
- C. Finn. 1990. Geophysical Constraints on Washington Convergent Margin Structure. *Journal of Geophysical Research*, **95**, 19533–19546.
- M. G. Glen, Johnathan, A. E. Egger, and D. A. Ponce. 2008. Structures controlling geothermal circulation identified through gravity and magnetic transects, Surprise Valley, California, Northwestern Great Basin. *Geothermal Resources Council Transactions*, **32**, 279–283.
- H. D. Gower, J. C. Yount, and R. S. Crosson. 1985. Seismotectonic Map of the Puget Sound Region, Washington. *U.S. Geological Survey Miscellaneous Investigations Series Map I-613*, scale 1:250,000.

- P. J. Haeussler, and K. P. Clark. 2000. Geologic Map of the Wildcat Lake 7.5' Quadrangle, Kitsap and Mason Counties, Washington. *U.S. Geological Survey Open-File Report 00-356*.
- M. M. Haney, T. D. Mikesell, K. van Wijk, and H. Nakahara. 2012. Extension of the spatial autocorrelation (SPAC) method to mixed-component correlations of surface waves. *Geophysical Journal International*, **191**(1), 189–206.
- R. A. Haugerud, D. J. Harding, S. Y. Johnson, J. L. Harless, C. S. Weaver, and B. L. Sherrod. 2003. High-Resolution Lidar Topography of the Puget Lowland, Washington A Bonanza for Earth Science. *GSA Today*, **13**(6), 4–10.
- D. M. Hirsch, and R. S. Babcock. 2009. Spatially heterogeneous burial and high-P/T metamorphism in the Crescent Formation, Olympic Peninsula, Washington. *American Mineralogist*, **94**(8-9), 1103–1110.
- J. F. Hughes. 2005. Meters of Synchronous Holocene Slip on two Strands of a Fault in the Western Puget Sound Lowland, Washington. *AGU Fall Meeting Abstracts*, **1**, 1020.
- B. H. Jacobsen. 1987. A case for upward continuation as a standard separation filter for potential-field maps. *Geophysics*, **52**(8), 1138–1148.
- G. C. Jacoby, P. L. Williams, and B. M. Buckley. 1992. Tree Ring Correlation Between Prehistoric Landslides and Abrupt Tectonic Events in Seattle, Washington. *Science*, **258**(5088), 1621–1623.
- S. Y. Johnson. 1985. Eocene strip-slip faulting and nonmarine basin formation in Washington. *Pages 283–302 of: K. T. Biddle, and N. Christie-Black (eds), Strike-*

- Slip Deformation, Basin Formation, and Sedimentation*, vol. 37. Special publication by the Society of Economic Paleontologists and Mineralogists.
- S. Y. Johnson, C. J. Potter, and J. M. Armentrout. 1994. Origin and evolution of the Seattle Fault and Seattle Basin, Washington. *Geology*, **22**(1), 71–74.
- S. Y. Johnson, C. J. Potter, J. M. Armentrout, J. J. Miller, C. A. Finn, and C. S. Weaver. 1996. The southern Whidbey Island Fault; an active structure in the Puget Lowland, Washington. *Geol Soc Am Bull*, **108**(3), 334–354.
- S. Y. Johnson, S. V. Dadisman, J. R. Childs, and W. D. Stanley. 1999. Active tectonics of the Seattle Fault and central Puget Sound, Washington; implications for earthquake hazards. *Geol Soc Am Bull*, **111**(7), 1042–1053.
- S. Y. Johnson, R. J. Blakely, W. J. Stephenson, S. V. Dadisman, and M. A. Fisher. 2004. Active shortening of the Cascadia forearc and implications for seismic hazards of the Puget Lowland. *Tectonics*, **23**(TC1011), 1–27.
- R. E. Karlin, and S. E. B. Abella. 1992. Paleoearthquakes in the Puget Sound Region Recorded in Sediments from Lake Washington, U.S.A. *Science*, **258**(5088), 1617–1620.
- H. M. Kelsey, B. L. Sherrod, A. R. Nelson, and T. M. Brocher. 2008. Earthquakes generated from bedding plane-parallel reverse faults above an active wedge thrust, Seattle fault zone. *Geological Society of America Bulletin*, **120**(11-12), 1581–1597.
- D. Komatitsch, and J. Tromp. 1999. Introduction to the spectral-element method for 3-D seismic wave propagation. *Geophysical J, International*, **139**, 806–822.

- D. Komatitsch, and J. Tromp. 2002. Spectral-element simulations of global seismic wave propagation-I. Validation. *Geophysical Journal International*, **150**, 390–412.
- D. Komatitsch, and J. P. Vilotte. 1998. The spectral-element method: an efficient tool to simulate the seismic response of 2D and 3D geological structures. *Bulletin of the Seismological Society of America*, **88**, 368–392.
- D. Komatitsch, J. Ritsema, and J. Tromp. 2002. The spectral-element method, Beowulf computing, and global seismology. *Science*, **298**, 1737–1742.
- A. P. Lamb, L. M. Liberty, R. J. Blakely, T. L. Pratt, B. L. Sherrod, and K. v. Wijk. 2012a. Western limits of the Seattle fault zone and its interaction with the Olympic Peninsula, Washington. *Geosphere*, **8**(4), 915–930.
- A. P. Lamb, L. M. Liberty, K. van Wijk, A. Revil, and C. Diggins. 2012b. Near-surface imaging of a hydrogeothermal system at Mount Princeton, Colorado using 3D seismic, self-potential, and dc resistivity data. *The Leading Edge*, **31**(1), 70–74.
- J. M. Lees, and R. S. Crosson. 1990. Tomographic Imaging of Local Earthquake Delay Times for Three-Dimensional Velocity Variation in Western Washington. *Journal of Geophysical Research*, **95**(B4), 4763–4776.
- L. M. Liberty, and T. L. Pratt. 2008. Structure of the Eastern Seattle Fault Zone, Washington State: New Insights from Seismic Reflection Data. *Bulletin of the Seismological Society of America*, **98**(4), 1681–1695.
- J. N. Louie. 2001. Faster, better: shear-wave velocity to 100 meters depth from refraction microtremor arrays. *Bulletin of the Seismological society of America*, **91**(2), 347–364.

- C. G. Mace, and K. M. Keranen. 2012. Oblique fault systems crossing the Seattle Basin: Geophysical evidence for additional shallow fault systems in the central Puget Lowland. *Journal of Geophysical Research*, **117**(B03105), 1–19.
- S. Mazzotti, H. Dragert, R. D. Hyndman, M. Miller, and J. A. Henton. 2002. GPS deformation in a region of high crustal seismicity: N. Cascadia forearc. *Earth and Planetary Science Letters*, **198**(1-2), 41–48.
- R. McCaffrey, A. I. Qamar, R. W. King, R. E. Wells, G. Khazaradze, C. A. Williams, C. W. Stevens, J. J. Vollick, and P. C. Zwick. 2007. Fault locking, block rotation and crustal deformation in the Pacific Northwest. *Geophysical Journal International*, **169**, 1315–1340.
- J. P. McCalpin, and J. R. Shannon. 2005. *Geologic map of the Buena Vista West Quadrangle, Chaffee County, Colorado*. Open-File Report 05-8. Colorado Geological Survey, Department of Natural Resources, Denver, CO.
- M. G. Miller. 1999. Active breaching of a geometric segment boundary in the Sawatch Range normal fault, Colorado, USA. *Journal Of Structural Geology*, **21**(7), 769–776.
- A. R. Nelson, S. Y. Johnson, H. M. Kelsey, R. E. Wells, B. L. Sherrod, S. K. Pezopane, L.-A. Bradley, R. D. Koehler, and R. C. Bucknam. 2003. Late Holocene earthquakes on the Toe Jam Hill fault, Seattle fault zone, Bainbridge Island, Washington. *Geological Society of America Bulletin*, **115**(11), 1388–1403.
- J. Olona, G. Pulgar, G. Fernández-Viejo, C. López-Fernández, and J. M. González-Cortina. 2010. Weathering variations in a granitic massif and related geotechnical

- properties through seismic and electrical resistivity methods. *Near Surface Geophysics*, **8**(6), 585 – 599.
- C. B. Park, R. D. Miller, and J. Xia. 1999. Multichannel analysis of surface waves. *Geophysics*, **64**(3), 800–808.
- T. Parsons, A. M. Trehu, J. H. Luetgert, K. Miller, F. Kilbride, R. E. Wells, M. A. Fisher, E. Flueh, U. S. ten Brink, and N. I. Christensen. 1998. A new view into the Cascadia subduction zone and volcanic arc: Implications for earthquake hazards along the Washington margin. *Geology*, **26**(3), 199–202.
- J. Phillips, R. Hansen, and R. Blakely. 2007. The use of curvature in potential-field interpretation. *Exploration Geophysics*, **38**(2), 111–119.
- T. L. Pratt, S. Johnson, C. Potter, W. Stephenson, and C. Finn. 1997. Seismic reflection images beneath Puget Sound, western Washington State: The Puget Lowland thrust sheet hypothesis. *Journal of Geophysical Research*, **102**, 27469–27490.
- E. Priolo, J. M. Carcione, and G. Seriani. 1994. Numerical simulations of interface waves by high-order spectral modeling techniques. *Journal of the Acoustical Society of America*, **95**, 681–693.
- K. Richards, A. Revil, A. Jardani, F. Henderson, M. Batzle, and A. Haas. 2010. Pattern of shallow ground water flow at Mount Princeton Hot Springs, Colorado, using geoelectrical methods. *Journal Of Volcanology And Geothermal Research*, **198**(1-2), 217–232.

- G. P. Roberts. 1996. Variation in fault-slip directions along active and segmented normal fault systems. *Journal Of Structural Geology*, **18**(6), 835–845.
- E. A. Robinson, and M. Saggaf. 2001. Klauder wavelet removal before vibroseis deconvolution. *Geophysical Prospecting*, **49**(3), 335–340.
- J. E. Sceva. 1957. Geological and ground-water resources, Kitsap County, Washington. *U.S. Geol. Surv. Water Supply Pap.*, **14413**.
- J. E. Schuster. 2005. Geologic map of Washington State. *Washington Division of Geology and Earth Resources Geologic Map GM-53, scale 1:250,000*.
- R. L. Schuster, R. L. Logan, and P. T. Pringle. 1992. Prehistoric Rock Avalanches in the Olympic Mountains, Washington. *Science*, **258**(5088), 1620–1621.
- G. R. Scott, R. E. Van Alstine, and W. N. Sharp. 1975. Geologic map of the Poncha Springs quadrangle, Chaffee County, Colorado. *U.S. Geological Survey Miscellaneous Field Studies Map MF-658*. U.S. Geological Survey, Denver, CO.
- B. L. Sherrod. 2001. Evidence for earthquake-induced subsidence about 1100 yr ago in coastal marshes of southern Puget Sound, Washington. *Geological Society of America Bulletin*, **113**(10), 1299–1311.
- B. L. Sherrod, R. C. Bucknam, and E. B. Leopold. 2000. Holocene Relative Sea Level Changes along the Seattle Fault at Restoration Point, Washington. *Quaternary Research*, **54**(3), 384–393.
- B. L. Sherrod, T. M. Brocher, C. S. Weaver, R. C. Bucknam, R. J. Blakely, H. M. Kelsey, A. R. Nelson, and R. Haugerud. 2004. Holocene fault scarps near Tacoma, Washington, USA. *Geology*, **32**(1), 9–12.

- B. L. Sherrod, R. J. Blakely, C. S. Weaver, H. M. Kelsey, E. Barnett, L. Liberty, K. L. Meagher, and K. Pape. 2008. Finding concealed active faults: Extending the southern Whidbey Island fault across the Puget Lowland, Washington. *Journal of Geophysical Research*, **113**(B05313), 1–25.
- R. P. Smith, V. J. S. Grauch, and D. D. Blackwell. 2002. Preliminary results of a high-resolution aeromagnetic survey to identify buried faults at Dixie Valley, Nevada. *Geothermal Resources Council Transactions*, **26**, 543–546.
- C. M. Snelson, T. M. Brocher, K. C. Miller, T. L. Pratt, and A. M. Trehu. 2007. Seismic Amplification within the Seattle Basin, Washington State: Insights from SHIPS Seismic Tomography Experiments. *Bulletin of the Seismological Society of America*, **97**(5), 1432–1448.
- W. J. Stephenson, A. D. Frankel, J. K. Odum, R. A. Williams, and T. L. Pratt. 2006. Toward resolving an earthquake ground motion mystery in west Seattle, Washington State: Shallow seismic focusing may cause anomalous chimney damage. *Geophysical Research Letters*, **33**, 4.
- W. Stephenson, S. Hartzell, A. Frankel, M. Asten, D. Carver, and W. Kim. 2009. Site characterization for urban seismic hazards in lower Manhattan, New York City, from microtremor array analysis. *Geophysical Research Letters*, **36**(L03301), 1–5.
- R. W. Tabor, and W. M. Cady. 1978a. Geologic map of the Olympic Peninsula, Washington. *U.S. Geological Survey Miscellaneous Investigations Series Map I-994*, scale 1:125,000.

- R. W. Tabor, and W. M. Cady. 1978b. *The structure of the Olympic Mountains, Washington: analysis of a subduction zone*. U.S. Geological Survey Professional Paper 1033.
- R. W. Tabor, R. A. Haugerud, P. J. Haeussler, and K. P. Clark. 2011. Lidar-revised Geologic Map of the Wildcat Lake 7.5' Quadrangle, Kitsap and Mason Counties, Washington. *U.S. Geological Survey Scientific Investigations Map 3187, scale 1:24,000*.
- U. S. ten Brink, P. C. Molzer, M. A. Fisher, R. J. Blakely, R. C. Bucknam, T. Parsons, R. S. Crosson, and K. C. Creager. 2002. Subsurface Geometry and Evolution of the Seattle Fault Zone and the Seattle Basin, Washington. *Bulletin of the Seismological Society of America*, **92**(5), 1737–1753.
- A. M. Trehu, I. Asudeh, T. M. Brocher, J. H. Luetgert, W. D. Mooney, J. L. Nabelek, and Y. Nakamura. 1994. Crustal Architecture of the Cascadia Forearc. *Science*, **266**(5183), 237–243.
- V. C. Tsai, and M. P. Moschetti. 2010. An explicit relationship between time-domain noise correlation and spatial autocorrelation (SPAC) results. *Geophysical Journal International*, **182**(1), 454–460.
- T. M. van Wagoner, R. S. Crosson, K. C. Creager, G. Medema, L. Preston, N. P. Symons, and T. M. Brocher. 2002. Crustal structure and relocated earthquakes in the Puget Lowland, Washington, from high-resolution seismic tomography. *Journal of Geophysical Research (Solid Earth)*, **107**, 2381.
- K. van Wijk, T. D. Mikesell, V. Schulte-Pelkum, and J. Stachnik. 2011. Estimating

- the Rayleigh-wave impulse response between seismic stations with the cross terms of the Green tensor. *Geophysical Research Letters*, **38**(L16301), 1–4.
- D. L. Wells, and K. J. Coppersmith. 1994. New empirical relationships among magnitude, rupture length, rupture width, rupture area, and surface displacement. *Bulletin of the Seismological Society of America*, **84**(4), 974–1002.
- R. E. Wells, D. C. Engebretson, P. D. S. Jr, and R. S. Coe. 1984. Cenozoic plate motions and the volcano-tectonic evolution of western Oregon and Washington. *Tectonics*, **3**(2), 275–294.
- R. E. Wells, C. S. Weaver, and R. J. Blakely. 1998. Fore-arc migration in Cascadia and its neotectonic significance. *Geology*, **26**(8), 759–762.
- J. White. 1983. *Underground sound: Application of seismic waves*. Methods in geochemistry and geophysics, no. 18. Elsevier.
- J. R. Wilson, M. J. Bartholomew, and R. J. Carson. 1979. Late Quaternary faults and their relationship to tectonism in the Olympic Peninsula, Washington. *Geology*, **7**(5), 235–239.
- J. Wilson. 1975. *Geology of the Price Lake area, Mason County, Washington*. M.S. thesis, North Carolina State University, Raleigh.
- R. C. Witter, R. W. Givler, and R. J. Carson. 2008. Two Post-Glacial Earthquakes on the Saddle Mountain West Fault, Southeastern Olympic Peninsula, Washington. *Bulletin of the Seismological Society of America*, **98**(6), 2894–2917.
- O. Yilmaz. 2001. *Seismic data analysis*. Society of Exploration Geophysicists.